DISTRIBUTED PARAMETER ACTIVE VIBRATION CONTROL OF SMART STRUCTURES

by

Scott E. Miller
S.B., Massachusetts Institute of Technology
(1986)

SUBMITTED TO THE DEPARTMENT OF MECHANICAL ENGINEERING
IN PARTIAL FULFILLMENT OF THE REQUIREMENTS
FOR THE DEGREE OF

MASTER OF SCIENCE
IN
MECHANICAL ENGINEERING

at the

MASSACHUSETTS INSTITUTE OF TECHNOLOGY
April 26, 1988

Signature of Author_____
Department of Mechanical Engineering
April 26, 1988

Certified by_____
Dr. James E. Hubbard, Jr.
Thesis Supervisor, C.S. Draper Technical Staff

Accepted by_____
Professor Ain A. Sonin
Chairman, Department Thesis Committee

DISTRIBUTED PARAMETER ACTIVE VIBRATION CONTROL
OF SMART STRUCTURES

by

Scott E. Miller

submitted to the Department of Mechanical Engineering
in partial fulfillment of the
requirements for the degree of Master of Science

ABSTRACT

A vibration control strategy for multi-component structures has been developed in which the structural components are actively damped beam members. Each component is *smart* in the sense that it is an active vibration control system which is autonomous of all other structural components. Distributed sensor and actuator transducers constructed from polyvinylidene fluoride (PVF_2) are embedded in each beam element. Lyapunov's direct method was used to develop a vibration control strategy for a generalized system consisting of an arbitrary number of smart beam members rigidly joined at a common boundary. The analysis leads to a smart component control law which guarantees stability to the global system. The distributed transducer electric fields may be varied to provide controllability to all modes or to specific modal subsets of a structure. Guidelines are presented for choosing film electrode spatial distributions to meet design goals. A *universal* spatial film distribution is proposed which has the potential of providing active damping to all modes of many structures with nearly arbitrary boundary conditions.

To develop the control methodology, theoretical models for spatially distributed transducers on flexible beam components were derived. An analytical model for spatially distributed sensors on flexible beam elements was developed without the necessity of modeling the beam in terms of its component vibrational modes. The model provides insight into the observability of beams with nearly arbitrary boundary conditions. The sensor electrode surface may be spatially distributed so as to function similar to point sensors or to produce a signal in which certain vibrational modes of the structure are weighted more than others. A previously derived model for PVF_2 actuators is presented in terms of its duality with the distributed sensor analysis. The sensor model was verified experimentally for spatially uniform and linearly-varying sensors applied to a clamped-free beam. The signals provided by the distributed sensors were compared to the outputs of corresponding point sensors. PVF_2 sensors and actuators situated on the same structural component developed radiative noise problems which were effectively compensated with noise reduction circuitry.

Experimental results were obtained which validate the *smart* structure control strategy. A *smart* beam component was constructed, the component was cantilevered, and controllability was demonstrated for the first two vibrational modes. A multi-component structure was then constructed from three rigidly joined autonomous smart components, and the *smart* structure control methodology was validated experimentally. Frequency and transient response data for the first four modes demonstrate that the smart structure control strategy is effective in providing active damping. A digital simulation using MSC-NASTRAN and CTRL-C yielded results which support the experimental analysis. The simulation demonstrates a methodology for modeling and analyzing *smart* structures.

Thesis Supervisor: Dr. James E. Hubbard, Jr.
Title: Lecturer of Mechanical Engineering, MIT
C.S. Draper Laboratory Technical Staff

ACKNOWLEDGEMENT

This thesis is dedicated to Carole Stacy Berkowitz. In her brief life Carole brought warmth into the lives of many people: I feel fortunate to have been one of those individuals. She always strived to repair the many injustices that we face in our world, and so she chose to dedicate her life to helping the deaf and the emotionally ill. Carole had a gift of human understanding that has touched many. Carole will always be missed, and will be forever with me.

You are never given a dream without also given the power to make it true. Completing my Masters degree at MIT is the fulfillment of a dream for me, and one that would not have been possible without the support of many truly caring people. My mother and father taught me as a child to pursue my dreams, and as an adult that sharing one's dreams with the people one loves is the essential element that makes life a joyful experience. My brother, Eric, is my friend as well, and I am thankful that we are close. Tamar Siegel, who has had to endure her share of neglect over the past few months as I have been laboring over my thesis, has always been a terrific provider of encouragement and support. Bob Litt and Fran Myman helped to pull me through some difficult times, and have proven themselves to be people I can always count on.

This thesis would not have materialized if not for the support of some extraordinary minds at Draper Laboratory. I would like to thank Jim Hubbard for being my thesis advisor, and for putting his confidence in me to help me to grow both technically and individually. Alex Gruzen is a LATEX wizard, and has really helped to make Draper a pleasant environment for me. Tom Bailey has been an invaluable help to me over these past two years, and to Tom I leave a thousand questions and all of my retired MORIA characters. Shawn Burke and John Connally have been excellent sources of good judgement at times when I wasn't: to both of them I leave all of my *stability* issues. There are a great many people both in and outside of Draper that must go unmentioned (or I may never finish this thesis), which I apologize for. You have all been invaluable.

TABLE OF CONTENTS

LIST OF FIGURES

LIST OF TABLES

Chapter 1

Introduction

The component elements used in systems such as large space structures are typically light, flexible, and have a large number of vibrational modes. These modes are generally lightly damped. Mission requirements, such as weight constraints, often preclude the incorporation of passive damping treatments. As a result, interest has been generated in the past several years regarding the application of active control techniques to the vibration control of distributed systems [1]. Traditionally, active dampers used in this context have been based on the implementation of a finite number of discrete sensors and actuators [2,3,4,5]. Since the flexible components are continuous and in theory possess an infinite number of degrees of freedom, these control schemes truncate the system model to a finite number of discrete modes [5]. It is often difficult to determine the number of modes required to accurately model the structure, and to reconcile the location of the sensors and actuators.

A research effort was initiated at MIT to apply a distributed actuator to the vibration control of a flexible beam [6,7]. The active damper consisted of a layer of the piezoelectric polymer, polyvinylidene fluoride (PVF_2). PVF_2 is a polymer which can be made piezoelectrically active through appropriate processing during manufacture. A voltage field applied across the faces of the film layer results in a longitudinal strain over its area. Analysis has shown that controllability for nearly arbitrary beam boundary configurations can be achieved by permitting the distributed actuator's control to vary in space as well as in time [1]. The results further indicate that for a broad class of boundary conditions, controllability can be achieved by producing an electric field across the distributed film actuator that is proportional to a unique feedback parameter [8].

The research study described herein was begun in part to design and construct distributed sensors using PVF_2 film. The study emphasizes the versatility of film sensors in particular applications relating to lightly damped beams, with the intention of showing how distributed sensors may be used in alternate applications. The use of PVF_2 film as a sensor has been studied in applications that have included detecting tactile information for robotic endeffectors [9], utilizing PVF_2 as a tactile stimulator and mechanical transformer element in a reading aid for the blind [10], implementing piezoelectric film in high frequency audio speaker systems [11,12,13], and others [14]. In the area of elastic continua, some research has been completed in which general observability and controllability conditions for a flexible body have been developed. it has been shown that in many cases, controllability and observability of all flexural modes can be achieved in theory with only one sensor and actuator pair co-located at a free boundary [15].

A model for the design and analysis of spatially distributed sensors is presented which shows that observability for nearly arbitrary beam configurations is possible by utilizing distributed sensors whose strain field is caused to vary spatially. In this study PVF_2 constitutes the active element: however, the analysis is applicable to all candidate materials which behave in a distributed manner to produce an electric field from applied strain. The model was derived without the necessity of modelling the beam in terms of its component vibrational modes. The model shows that the sensor electrode layers can be spatially varied so as to produce signals similar to point sensors or signals in which certain vibrational modes are weighted more than others. Experimental results are presented which support the model for two separate spatially varying electrode distributions on a cantilever beam. The film sensors were compared to corresponding point sensors. Radiative cross-coupling effects between PVF_2 sensors and actuators were investigated, and a simple compensation technique was devised which effectively eliminates adverse noise corruption.

The main intent of this research effort was to develop a vibration control strategy for multi-component flexible structures. The control methodology that has subsequently been developed and presented herein utilizes distributed transducers in order to preserve the ability to simultaneously control all modes or a specified subset of modes. The distributed sensor and actuator models are combined with Lyapunov's

second method, leading to a control law for flexible beam components. These actively controlled beam components are *smart* in the sense that all of the essential elements of the active damper are self-contained (the component is a beam/PVF_2 composite in which the control algorithm may be embedded on a microchip). A strategy is developed for the vibration control of a generalized structure consisting of an **arbitrary** number of *smart* structural members rigidly joined at a common boundary. The global system can be controlled by enforcing the component control law applied locally to each *smart* structural element. Lyapunov's second method is used to derive the multi-component structure control strategy. Enforcing the control law guarantees the stability of the global system for any spatial distribution of the transducer strain fields. Guidelines are presented for choosing spatial distributions to meet design goals. A "universal" *smart* component transducer electrode distribution is presented which has the character of providing active damping to all modes of a structure for many structural configurations.

Experimental results were obtained which validate the *smart* structure control strategy. A *smart* beam component was constructed, the component was cantilevered, and controllability was demonstrated for the first two vibrational modes. A multi-component structure was then constructed from three rigidly joined autonomous smart components, and the *smart* structure control methodology was validated experimentally. Frequency and transient response data for the first four modes demonstrate that the smart structure control strategy is effective in providing active damping. The greatest increase in modal damping was observed at the second mode of the structure, for which the damping ratio was increased by a factor of 28.8. A digital simulation using MSC-NASTRAN and CTRL-C yielded results which support the experimental analysis. The simulation demonstrates a methodology for the computational modeling of *smart* structures.

Chapter 2

Theoretical Analysis of *Smart* Structural Components

2.1 Distributed Sensing Using PVF_2 Film

For uniaxially polarized PVF_2 film, a longitudinal strain induces an electric field across its faces [16]. The induced field may be varied spatially by shaping the electrode plating over the faces of the film or by varying the film's thickness [1]. Although in this study the active element is PVF_2, the analysis assumes only that the distributed sensor produces an electric field from longitudinal strain. The analysis is therefore applicable to other candidate materials.

The geometric configuration of a beam/sensor composite is shown in Fig. 2-1. A PVF_2 sensor layer is adhered to the top surface of a beam component. The film polarity vector is oriented such that the positively charged surface of the film is the outermost surface. The strain induced on the outer face of the sensor film, $\epsilon_f(y,\bar{t})$, is a function of the curvature:

$$\epsilon_f(y,\bar{t}) = -D\frac{\partial^2\eta}{\partial y^2} \qquad (2-1)$$

where D is the distance from the neutral axis to the sensor film surface, $\bar{t}$ is time, $\eta(y,\bar{t})$ is the elastic deflection of the neutral axis of the beam component parallel to the x-axis, and $\frac{\partial^2\eta}{\partial y^2}$ is the curvature. The distance, D, is given by

$$D = \frac{E_b h_b^2 + E_f h_f^2 + 2E_f h_b h_f}{2(E_b h_b + E_f h_f)} + \frac{h_f}{2} \qquad (2-2)$$

where E_b and E_f are the moduli of elasticity for the beam and film, and h_b and h_f are the thicknesses of the beam and film layers, respectively. Note that if the film

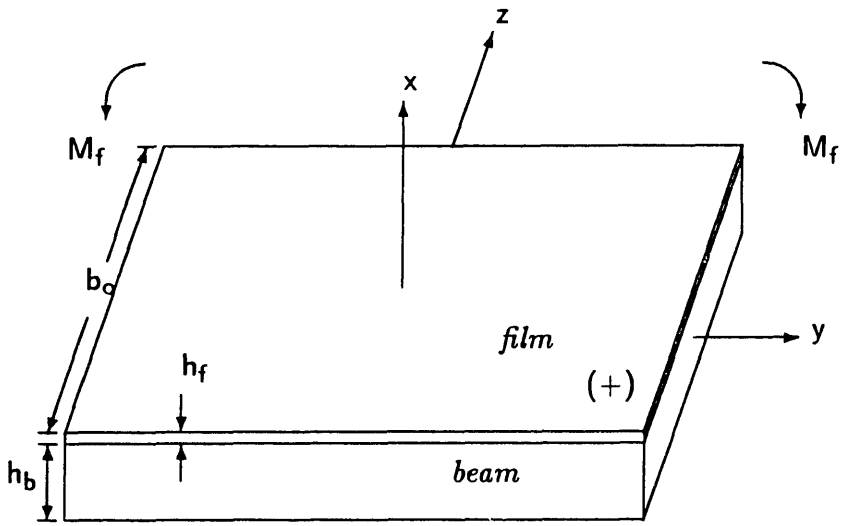

Figure 2-1. Geometry of a beam with a film transducer adhered to a single surface.

thickness is much smaller than the beam thickness then

$$D \cong \frac{h_b + h_f}{2} \qquad (2-3)$$

The charge developed at a point on the surface of the sensor film is directly proportional to the longitudinal strain acting on the film at that point,

$$q(y,\bar{t}) = \left(\frac{k_{31}^2}{g_{31}}\right) \hat{z}(y)\epsilon_f(y,\bar{t}) \qquad (2-4)$$

where $\hat{z}(y)$ is the distribution of the electric field parallel to the z- axis, k_{31} is the electromechanical coupling factor, and g_{31} is a piezoelectric film constant ($\frac{m^2}{Coul}$). The choice of the spatial weighting function, $\hat{z}(y)$, may be enforced in a number of ways, such as varying the geometric shape of the electrode plating or altering the film thickness. The electromechanical coupling factor indicates the ability of the piezoelectric material to exchange mechanical energy for electrical energy, and is a function of both frequency and the quality of adhesion between the film and beam. It is assumed that the thickness of the electrode layer on the surface of the PVF_2 film is negligible, so that spatially distributing the electrode plating does not significantly change the stiffness of the PVF_2 layer (electrode thickness is typically on the order of 400A° for Ni-Al plating on 28μm film [16]).

The total charge accumulated on the film surface, $Q(\bar{t})$, is the spatial summation of all point charges, $q(y,\bar{t})$, along the entire length of the electroplated film surface, L:

$$Q(\bar{t}) = \int_0^L q(y,\bar{t})dy \quad . \tag{2-5}$$

Combining Eq.'s (2-1), (2-4), and (2-5) gives

$$Q(\bar{t}) = -\left(\frac{k_{31}^2 D}{g_{31}}\right)\int_0^L \frac{\partial^2\eta}{\partial y^2}(y,\bar{t})\,\hat{z}(y)dy \quad . \tag{2-6}$$

It is preferable to nondimensionalize $\hat{z}(y)$ with respect to the width of the beam, b_o, so that

$$\Lambda(y) = \frac{\hat{z}(y)}{b_o} \tag{2-7}$$

where $\Lambda(y)$ represents a nondimensional spatial distribution function. By considering the capacitive effects of the film as a dielectric material and combining Eq.'s (2-6) and (2-7), a relation for the film sensor output voltage, V_f, is obtained:

$$V_f(\bar{t}) = -\frac{Q_o}{C_f}\int_0^L \frac{\partial^2\eta}{\partial y^2}\Lambda(y)dy \quad . \tag{2-8}$$

Eq. (2-8) is the governing distributed parameter sensor relation. C_f is the film capacitance. The constitutive charge coefficient, Q_o, has units of Coulombs and is defined in terms of the pertinent piezoelectric and geometric constants:

$$Q_o = \frac{b_o k_{31}^2 D}{g_{31}} \quad . \tag{2-9}$$

The central concepts which generated the model were the strain-curvature relationship for a beam in bending and the applicable piezoelectric relationship between longitudinal strain and charge developed on the film surface.

2.2 Distributed Actuation Using PVF_2 Film

The flexural vibrations of an elastic beam compone... having a PVF_2 actuation layer bonded to one face (see Fig. 2-1) have been described by Bailey [6]:

$$\frac{\partial^2}{\partial y^2}\left[EI\frac{\partial^2\eta}{\partial y^2} - m\bar{V}(y,\bar{t})\right] + \rho A\frac{\partial^2\eta}{\partial\bar{t}^2} = 0; \qquad 0 < y < L \tag{2-10}$$

where

$$\rho A = \rho_b A_b + \rho_f A_f \tag{2-11}$$

$$EI = E_b I_b + E_f I_f \tag{2-12}$$

$$m = -d_{31}(h_b + h_f)\frac{E_b E_f h_b b_o}{2(E_b h_b + E_f h_f)} \quad . \tag{2-13}$$

In the above expressions $\eta(y,\bar{t})$ is transverse displacement, d_{31} is a piezoelectric constant, h_b is the beam thickness, h_f is the thickness of the film layer, and b_o is the beam width. Bailey implicitly assumed throughout his analysis that the polarity vector of the film layer was oriented such that the positively biased surface of the film actuator was the outermost surface. The linear inhomogeneous equation (Eq. (2-10)) is the Bernoulli-Euler beam model with a bending moment term, $m \cdot \bar{V}(y,\bar{t})$, that results from the distributed action of the PVF_2 actuation layer. The control moment is as characterized a constant, m, which depends on the constitutive geometric, material, and piezoelectric properties of the composite structure and expresses the applied bending moment per volt. The actuation layer may be spatially varied in order to weight the function of the distributed moment, as is described in [8]. Eq. (2-10) may be non-dimensionalized for convenience, giving

$$\frac{\partial^4 w}{\partial Y^4} + \frac{\partial^2 w}{\partial t^2} = \frac{\partial^2 V}{\partial Y^2}; \qquad 0 < Y < 1 \tag{2-14}$$

where the non-dimensionalized variables have the following definitions:

$$Y = \frac{y}{L} \tag{2-15}$$

$$w = \frac{\eta}{L} \tag{2-16}$$

$$V = \frac{mL}{EI} \cdot \bar{V} \tag{2-17}$$

$$t = \bar{t}\sqrt{\left(\frac{EI}{\rho A L^4}\right)} \tag{2-18}$$

Eq. (2-14) may be used to determine the complete response of a particular system when combined with the appropriate set of boundary conditions. However the present form of Eq. (2-14) is ideally suited for investigating the behavior of

distributed actuation. The application of spatially varying actuator (and sensor) distributions is discussed in section 2.4.

A distributed parameter control algorithm was derived by Bailey [21,6] and Burke [8] using the second, or direct method of Lyapunov [23]. A Lyapunov functional was chosen that represents the sum of the beam's strain potential and kinetic energies:

$$F = \frac{1}{2}\int_0^1 \left[\left(\frac{\partial^2 w}{\partial Y^2}\right)^2 + \left(\frac{\partial w}{\partial t}\right)^2\right] dY \quad . \qquad (2-19)$$

Deriving the control algorithm using the Lyapunov functional in Eq. (2-19) allows for vibration damping to be implemented based on total system energy considerations and avoids the truncation of the system model. Burke showed that for a nearly arbitrary combination of boundary conditions for a given beam element, the time derivative of the Lyapunov functional (Eq. (2-19)) may be combined with the system governing equation (Eq. (2-14)) and written in the following form [8]:

$$\frac{dF}{dt} = \int_0^1 \frac{\partial^3 w}{\partial Y^2 \partial t} \cdot V(Y,t)dY + fcn\left(\frac{\partial w}{\partial t}(\xi,t), \frac{\partial^2 w}{\partial Y \partial t}(\xi,t), f(t), g(t)\right) \qquad (2-20)$$

where ξ represents the boundary point $Y = 0$ or $Y = 1$, and $f(t)$ and $g(t)$ are arbitrary forcing terms. The (normalized) control voltage to the actuation film, $V(Y,t)$, appears only in the spatial integral term. In order to insure that energy is always removed from the system, $V(Y,t)$ must be chosen to force the spatial integral term in Eq. (2-20) to always be negative. The control voltage may be written as the superposition of a control input time function, $\rho(t)$, and a spatial distribution function, $\Lambda(Y)$, such that

$$V(Y,t) = V_o \Lambda(Y)\rho(t) \qquad (2-21)$$

where V_o is the gain of the control signal. If the boundary terms are ignored in Eq. (2-20) and Eq. (2-20) is combined with Eq. (2-21), then

$$\frac{dF}{dt} = V_o \rho(t) \int_0^1 \frac{\partial^3 w}{\partial Y^2 \partial t} \Lambda(Y) dY \qquad (2-22)$$

This result will be combined in the next section with the distributed sensor relationship (Eq. (2-8)) in order to formulate a generalized control law for smart structural components.

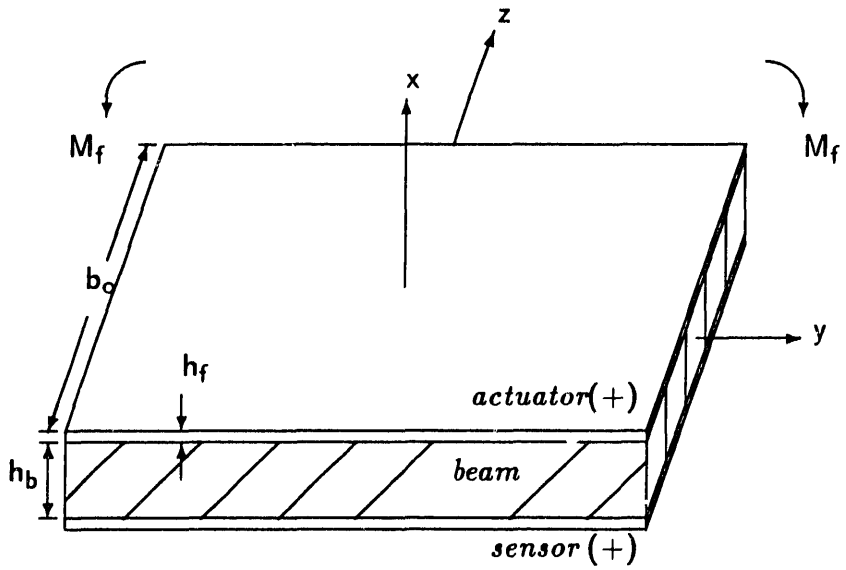

Figure 2-2. Geometry of a smart structural component.

2.3 Derivation of Smart Component Control Law

Specific constraints regarding the geometry of smart structural components must be rigidly obeyed in order to give validity to the control law presented in this section. In a smart component two distinctly separate layers of piezoelectric film are adhered to both faces of a flexible beam element as shown in Fig. 2-2. In this study PVF_2 is used as the candidate material, but the analysis lends itself to any material which can function in a distributed way to produce charge proportional to strain or induce strain due to an electric field applied across its faces. One film layer acts as a sensor and the other as an actuator. Both film layers must be oriented such that the polarity of each layer is positively biased on the outer surface and negatively biased on the inner surface. In this way the sign convention presented hereafter in the control law derivation is maintained. It is further assumed that both film distributions maintain identical spatial geometries. Regardless of what shape is chosen for a particular application, it is essential that both the sensor and actuator distributions are of the same shape. Finally, the sensor and actuator pair must be co-located on the structure so that the smart component is symmetrical along the y-z plane as shown in Fig. 2-2.

The distributed sensor model (Eq. (2-8)) may be non-dimensionalized in terms

of the new variable set described in Eq. (2-15), giving

$$\tilde{V}_f(t) = -\int_0^1 \frac{\partial^2 w}{\partial Y^2}(Y,t)\Lambda(Y)dY \qquad (2-23)$$

where $\tilde{V}_f = V_f \frac{C_f}{Q_o}$ is the nondimensionalized film sensor voltage. If the control signal time function, $\rho(t)$, in Eq. (2-22) is defined to be proportional to the time derivative of the sensor film output such that

$$\rho(t) = \frac{d\tilde{V}_f}{dt} \qquad (2-24)$$

then the time derivative of the Lyapunov functional, Eq. (2-22), becomes

$$\frac{dF}{dt} = -V_o \left[\int_0^1 \frac{\partial^3 w}{\partial Y^2 \partial t}\Lambda(Y)dY\right]^2 . \qquad (2-25)$$

Eq. (2-25) is a major result which validates the smart component control law given in Eq. (2-24). Eq. (2-25) is always non-positive, indicating that enforcing the control law (Eq. (2-24)) guarantees that energy will be removed from the system. The linear control law insures stability but does not optimize the amount of energy extracted from the system. The control law is applicable to any choice of spatially shaped film distributions, provided that the actuator and sensor distributions are identical and co-located. The control law insures that any film shape will provide controllability to the system; however, the character and effectiveness of the controller will ultimately be determined by the spatial distribution (see section 2.4). Similarly stability is insured, in the sense that if Eq. (2-24) is obeyed then energy can not be added to the system. A poor choice in a transducer shape may result in no active energy dissipation for certain vibrational modes, but will not provide excitation to those modes. The control law derivation has not required a modal analysis of the dynamic system; hence, the results are applicable to broad class of beams with nearly arbitrary boundary constraints.

2.4 Spatial Shaping of PVF_2 Transducers

In this section, theoretical results are presented which show that by spatially varying the electric field of the PVF_2 sensor and actuator layers, specific modal

subsets of an arbitrary beam system can be selectively controlled or all modes can be controlled simultaneously. A detailed treatment of spatially varying distributed sensors will be presented first, and analogies will then be made which link the behavior of spatially shaped sensors to the behavior of spatially shaped actuators.

2.4.1 Application of Spatially Distributed Sensors

The electric fields of distributed PVF_2 sensors and actuators may be varied so as to sense a distributed parameter or provide pure distributed actuation. PVF_2 transducer shapes may be carefully chosen in order to induce response functions similar to discrete transducers. Certain PVF_2 sensors can be described as measuring point angular and linear displacements, while similar PVF_2 actuators can be modeled as generating concentrated moments and forces. This representation is easily accomplished through the use of generalized functions, which are a notational restatement of singularity functions [17]. The generalized step function, $h(Y - a)$, is equal to zero for all $Y < a$ and equal to unity for all $Y \geq a$. Throughout the ensuing analysis it is assumed that distributed transducer electric fields are caused to vary by spatially shaping the electrode plating on the film surface. A spatially uniform electrode distribution which extends along the entire beam surface is denoted as

$$\Lambda(Y) = h(Y) - h(Y-1) \quad . \tag{2-26}$$

Similarly a "linearly-varying" electrode distribution extending along the entire length of the beam is written as

$$\Lambda(Y) = (1-Y)\,[h(Y) - h(Y-1)] \quad . \tag{2-27}$$

Both distributions are illustrated in Fig.'s 2-3 and 2-4.

2.4.1.1 Uniform Sensor Distribution

If the uniform distribution (Eq. (2-26)) is applied to the sensor model (Eq (2-23)) and the integral is solved, the result is

$$\tilde{V}_f(t) = \left[\frac{\partial w}{\partial Y}(0,t) - \frac{\partial w}{\partial Y}(1,t)\right] \tag{2-28}$$

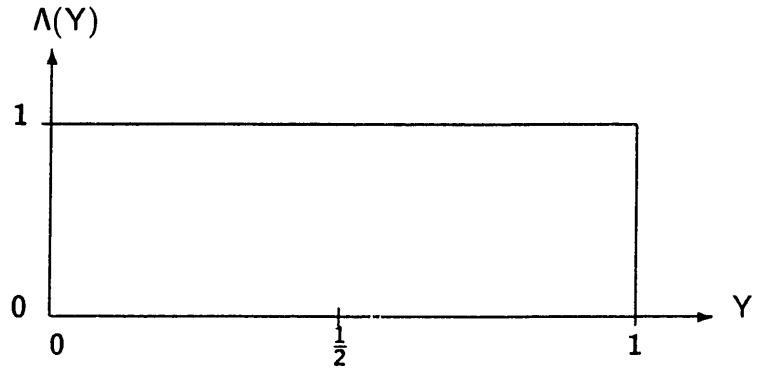

Figure 2-3. Spatially uniform film distribution.

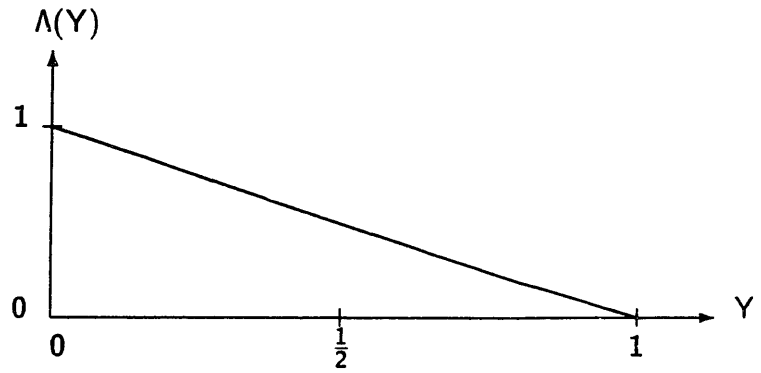

Figure 2-4. Linearly varying film distribution.

This result has been arrived at based on the underlying assumption that the strain-curvature relation (Eq. (2-1)) is valid and the governing relation (Eq. (2-23)) is integrable along the entire domain. If boundary constraints are such that both $\frac{\partial w}{\partial Y}(0,t)$ and $\frac{\partial w}{\partial Y}(1,t)$ are equivalent (e.g. clamp-clamped boundaries), then the uniform sensor distribution will fail to induce charge on the film surface. If the beam is clamped at $Y = 0$ and free at $Y = 1$, then the sensor will observe angular displacement at the free end, $\frac{\partial w}{\partial Y}(1,t)$.

Spatially uniform sensors can observe all modes of any beam configuration in which one boundary is either clamped or sliding and the opposing boundary is either pinned or free. For a cantilever beam every mode is characterized by a nonzero angular displacement at the free boundary, and therefore every mode gives a positive contribution to the sensor output. In this sense all modes are observable. The output of a spatially uniform sensor will always be a measurement of angular displacement. In a clamp-clamped configuration, however, both $\frac{\partial w}{\partial Y}(0,t)$ and $\frac{\partial w}{\partial Y}(1,t)$ are always equivalent and equal to zero, so that all modes are unobservable. Similarly a clamp-sliding configuration produces no sensor output.

An analysis of a uniform sensor on a pin-pinned beam lends insight into how distributed sensors function. The mode shapes of a pin-pinned (simply supported) beam are sinusoidal. Odd order modes exhibit even symmetry about the midspan, while for even modes the opposite is true. With all odd order modes, $\frac{\partial w}{\partial Y}(0,t) = -\frac{\partial w}{\partial Y}(1,t)$, the integral in Eq. (2-23) is nonvanishing and thus all odd order modes are observable. For even modes $\frac{\partial w}{\partial Y}(0,t) = \frac{\partial w}{\partial Y}(1,t)$, the integral in Eq. (2-23) vanishes and the uniform sensor is ineffective. The uniform sensor distribution may be represented as essentially half of a square wave in space and may be described in terms of a Fourier sine series containing only odd harmonics:

$$\Lambda(Y) = \frac{4}{\pi}\sum_{n=0}^{\infty}\frac{\sin((2n+1)\pi Y)}{2n+1}. \qquad (2-29)$$

The modes of a simply supported beam are sine functions,

$$w(Y,t) = \sum_{m=0}^{\infty}\sin(m\pi Y)\phi(t). \qquad (2-30)$$

If the two preceding equations are appropriately included in the sensor relation

(Eq. (2-23)), then the resulting constitutive relation nearly becomes a restatement of modal orthogonality for odd order modes of the pin-pinned beam. All even values for the mode number, m, cause the integral in Eq. (2-23) to be zero, since these even modes are orthogonal to every spatial harmonic in the Fourier decomposition of the uniformly distributed sensor.

2.4.1.2 Linearly-varying Sensor Distribution

If the linearly-varying distribution (Eq. (2-27)) is applied to the governing equation (Eq. (2-23)) and the integral is solved, then for all admissible curvatures the result is

$$\tilde{V}_f(t) = \left(\frac{\partial w}{\partial Y}(0,t) + w(0,t) - w(1,t)\right) \quad . \qquad (2-31)$$

The preceding equation reveals in part the significance of applying spatially varying sensors to certain beam configurations. Whereas the spatially uniform sensor cannot sense motion in a clamped-sliding beam, the linearly-varying sensor can: all modes become observable in the sense that each mode contributes a nonzero linear tip displacement at the sliding boundary.

In the case of the pin-pinned beam, the linearly-varying film distribution described in Eq. (2-27) may be used to effectively observe all structural modes. When the boundary constraints are applied to Eq. (2-39), the linear displacement terms vanish and only the angular displacement term at the $Y = 0$ boundary remains. A Fourier decomposition of this distribution would include all of the $\sin(m\pi Y)$ mode shapes. By replacing $\Lambda(Y)$ in the sensor governing equation (Eq. (2-23)) with the Fourier series of the ramp functional, the result would essentially be a restatement of orthogonality for both odd and even modes of the pin-pinned beam. With the uniform distribution the angular displacements at both boundaries are equivalent for even modes and cancel each other in Eq. (2-28). The linearly-varying distribution eliminates this effect and allows for all modes to be observable in the sense that the charge induced on the film will be the sum of nonzero contributions from all modes.

The linearly-varying sensor analysis reveals some unique features of spatially varying the sensor within the framework of generalized functions. Discontinuous *step changes* result in the sensing of *angular displacements* and discontinuous *slope*

changes result in the sensing of *linear displacements*. The uniform film distribution (Eq. (2-26)) on a cantilever beam senses angular displacement at the free end, whereas the linearly-varying distribution (Eq. (2-27)) applied to a cantilever beam clamped at Y=0 senses linear displacement at Y=1. Distributed sensors act as discrete sensors when in these configurations, provided that the beam curvature is admissible in the sense that the linear strain-curvature relationship (Eq. (2-1)) is applicable.

2.4.1.3 Other Spatially Varying Sensor Distributions

In this section, spatially varying sensor distributions that are neither uniform nor linearly-varying will be considered. The preceding discussion lends insight into how a distributed sensor may function comparatively with a point displacement sensor. Uniform and linearly-varying distributions may be applied to a broad class of boundary configurations to produce an output parameter which is the sum of contributions from even, odd, or both even and odd modes of the beam. Furthermore it is possible to synthesize spatial sensor distributions that will weight the angular displacement measurement more than the linear displacement measurement, or vice versa. The result may be a sensor signal that is more sensitive to odd modes than to even modes, etc., depending on the particular beam/sensor configuration.

The clamp-clamped beam provides an interesting example. A clamp-clamped beam will have modes with either a vanishing displacement or a vanishing slope at the midspan, but never both. Using insights gained from the previous analysis, an appropriate film distribution which senses contributions from all vibrational modes can be found. A spatial distribution with a discontinuous amplitude (step) change and slope change at the midspan will provide observability, and the magnitude of either the step or slope change may be varied to weight certain modes more than others. The spatial distributions in Fig.'s 2-5 and 2-6 have both step and slope changes at $Y = \frac{1}{2}$. However, the magnitude of the slope change in the former figure is twice that of the latter: thus in Fig. 2-5 odd modes are weighted twice as heavily as even modes relative to Fig. 2-6.

In certain applications it may be advantageous to resort to distributions which

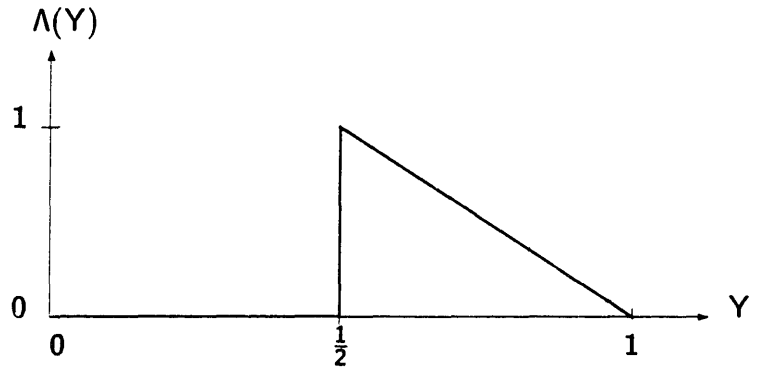

Figure 2-5. Spatial sensor distribution for a clamp-clamped beam.

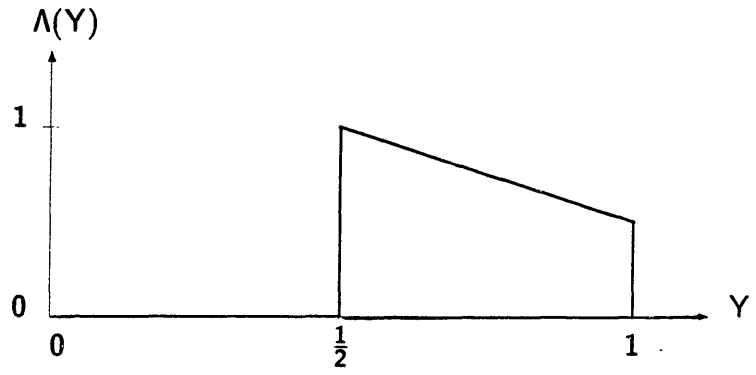

Figure 2-6. Spatial sensor distribution for a clamp-clamped beam.

have continuous slope changes that are non-uniform. An interesting example is that of sensing a single vibrational mode. Consider a beam configuration where the curvature relation corresponding to a particular mode has been determined analytically or approximated through computational methods. For most beam systems it is often impractical to determine the curvature relation corresponding to a specific mode; however, the purpose of this section is merely to demonstrate a unique example in which a nonlinear film distribution may be applied.

For a beam which obeys the Bernoulli-Euler equation there are two principle statements of modal orthogonality. They are described mathematically as [18]

$$\int_D \psi_j(Y)\psi_k(Y)dx = \delta_{jk} \qquad (2-32)$$

$$\int_D \psi_j(Y)\psi_k''''(Y)dx = \delta_{jk} \qquad (2-33)$$

where $\psi_j(Y)$ and $\psi_k(Y)$ are eigenfunctions which correspond to the j and k modes (the notation $()'$ indicates spatial differentiation), respectively, and

$$\delta_{jk} = \begin{cases} 0 & j \neq k \\ 1 & j = k \end{cases} \qquad (2-34)$$

If Eq. (2-33) is integrated twice by parts, the result is

$$\int_D \psi_j''(Y)\psi_k''(Y)dx - \left[\psi_j'(Y)\psi_k''(Y) - \psi_j(Y)\psi_k'''(Y)\right]_D = \delta_{jk} \qquad (2-35)$$

Realizing that an admissible solution to the Bernoulli-Euler equation is a displacement field, w(Y,t), of the form

$$w(Y,t) = A_0 \sum_{m=1}^{\infty} \psi_m(Y)e^{i\omega t} \qquad (2-36)$$

and comparing Eq. (2-35) with Eq. (2-23), one observes that if $\Lambda(Y)$ is chosen to vary spatially as the curvature, $\psi_k''(Y)$, of the k'th mode, then the sensor output will be proportional to the k'th mode only, subject to the constraint

$$\psi_k'(Y)\Lambda(Y) - \psi_k(Y)\Lambda'(Y) = 0. \qquad (2-37)$$

A pin-pinned beam is an example of a configuration which conforms to this constraint.

2.4.2 Application of Spatially Distributed Actuators

If the uniform film distribution, Eq. (2-26), is applied as a distributed actuator then the control input expression (Eq. (2-21)) becomes

$$V(Y,t) = V_o\,[h(Y) - h(Y-1)]\,\rho(t) \qquad (2-38)$$

The control input appears in the governing actuator equation (Eq. (2-10)) in terms of its Laplacian due to the beam moment curvature constitutive equations. The effective loading that the uniformly distributed actuator presents to the beam is found by examining the Laplacian of Eq. (2-38), which is given by

$$\frac{\partial^2 V}{\partial Y^2} = V_o\,[\delta'(Y) - \delta'(Y-1)]\,\rho(t) \qquad (2-39)$$

where the δ' terms are "doublet" or "concentrated point moment" functions. If the linearly varying distribution is applied as an actuator then the control input expression becomes

$$V(Y,t) = V_o(1-Y)\,[h(Y) - h(Y-1)]\,\rho(t) \qquad (2-40)$$

for which the Laplacian is given by

$$\frac{\partial^2 V}{\partial Y^2} = V_o\,[\delta'(Y) + \delta(Y) - \delta(Y-1)]\,\rho(t) \qquad (2-41)$$

where the δ terms represent "Dirac delta" or "concentrated point force" functions. A detailed treatment of PVF_2 as a distributed actuator is presented by Burke [8], who rigorously shows that discontinuities in *amplitude* give rise to *point moments*, while discontinuities in *slope* give rise to *point forces*. Prior studies have shown experimentally that the location of the discontinuities can be varied so as to implement an actuator which will provide control to all modes or to a desired subset of modes [1]. Distributed actuator behavior is therefore analogous to that of distributed sensors in the sense that PVF_2 sensors observe angular displacements at

locations of amplitude discontinuities and linear displacements at locations of slope discontinuities. All of the theoretical observations made in the previous sections regarding spatially shaped sensor distributions are applicable to distributed actuators as well.

Chapter 3

Theoretical Analysis of *Smart* Structures

3.1 Equations of Motion for a Generalized Structure

In this chapter the control law stated in Eq. (2-24) is applied in a general sense to a system constructed from an arbitrary arrangement of several smart structural elements. A generalized system is depicted in Fig. 3-1 in which an arbitrary number of smart components are rigidly joined to the free end of a cantilever beam. This system was chosen to facilitate an extension of the analysis which follows to a broad class of arbitrary structure geometries. The results of this chapter indicate that the energetic reactions between the component members will not degrade the stability of the actively controlled structure. The equations of motion are derived using Hamilton's Principle. Lyapunov's direct method is then applied to the system in conjunction with the distributed sensor and actuator models presented in the previous chapter to arrive at a control law for the generalized system.

Fig. 3-1 shows the geometry of the system. For convenience it is assumed that all beam components have a characteristic length, L. An inertial reference frame, designated as the $X_oY_oZ_o$ frame is attached to the base of the cantilever beam. Rotating reference frames are assigned to each of the elements that are rigidly connected to the free end of the cantilever. The frame associated with the j'th member is the designated as the $x_jy_jz_j$ frame. The $\hat{u}_{y_j}$ unit vector is defined as tangent to the j'th element at the common junction, as shown in the figure. When the structure is at rest, the $x_jy_jz_j$ frame is rotated with respect to the inertial frame through the angle ϕ_j in the $\hat{u}_{Z_o}$ direction. The elastic deformation of the j'th element, $\eta_j(y_j, \bar{t})$, is defined as the distance along a line perpendicular to the $\hat{u}_{y_j}$-axis from any ar-

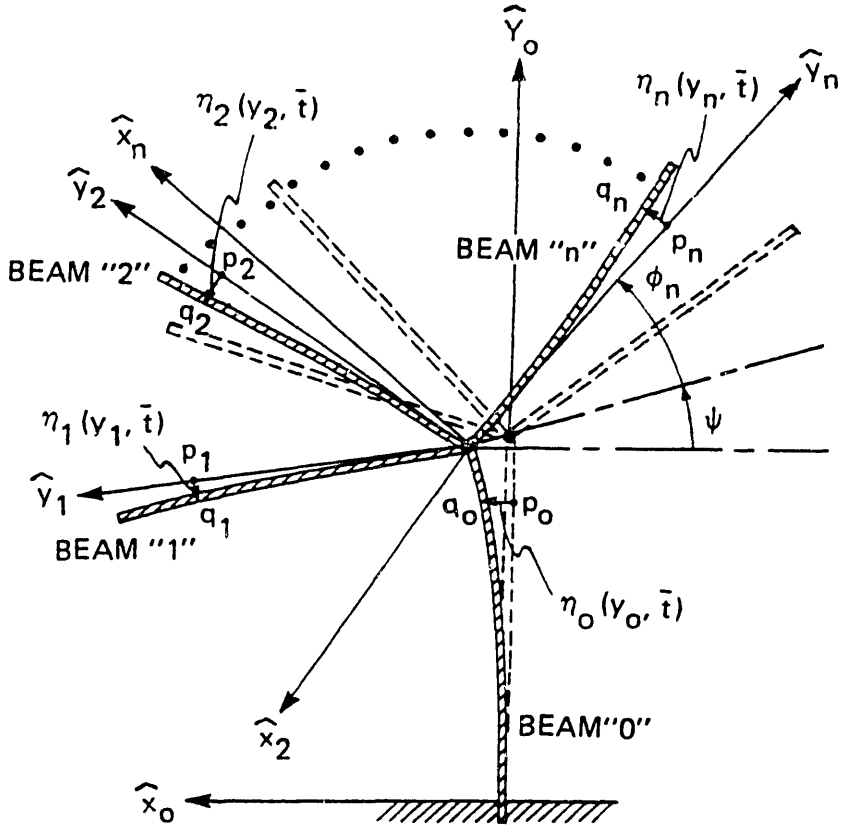

Figure 3-1. Geometry of a superstructure formed from an arbitrary number of smart structural elements.

bitrary point p_j on the $\hat{u}_{y_j}$-axis to a point q_j on the j'th smart component. For a system consisting of n components, a set of generalized coordinates which completely specifies the system configuration at any instant of time can be expressed as $\sum_{j=0}^{n} \eta_j(y_j, \bar{t})$. This set of coordinates is completely independent since each coordinate can be arbitrarily varied while keeping all other coordinates fixed. Not shown in the figure are arbitrary forces, $f_j(\bar{t})$, and arbitrary moments, $g_j(\bar{t})$, which may act at every boundary point $y_j = 1$.

To find the equations of motion it is first necessary to locate the point q_j with

respect to the inertial frame. From Fig. 3-1,

$$\vec{R}_{q_o} = y_o \hat{u}_{Y_o} + \eta_o \hat{u}_{X_o} \qquad (3-1)$$

and

$$\vec{R}_{q_j} = L\hat{u}_{Y_o} + \eta_o^L \hat{u}_{X_o} + y_j \hat{u}_{y_j} + \eta_j \hat{u}_{x_j} \qquad j = 1, ..., n \qquad (3-2)$$

where η_o^L is defined as the translation of the 0'th component (i.e. the base beam) in the $\hat{u}_{X_o}$ direction at $y_o = L$. The velocities of the points q_j with respect to the inertial frame are found by differentiating the displacement vectors:

$$\vec{V}_{q_o} = \frac{d\vec{R}_{q_o}}{dt} = \dot{\eta}_o \hat{u}_{X_o} \qquad (3-3)$$

and

$$\vec{V}_{q_j} = \frac{d\vec{R}_{q_j}}{dt} = \dot{\eta}_o^L \hat{u}_{X_c} + y_j \frac{d\hat{u}_{y_j}}{dt} + \dot{\eta}_j \hat{u}_{x_j} + \eta_j \frac{d\hat{u}_{x_j}}{dt} \qquad (3-4)$$

where $j = 1, ..., n$.

The time derivative of a unit vector in a rotating frame is defined as the cross-product between the angular velocity of the frame with respect to the inertial reference frame and the unit vector. Defining $\psi(t)$ as the slope of the base beam (beam "0") at $y_o = L$, i.e. $\psi(t) = \frac{\partial \eta_o}{\partial y_o}(L, t)$, then the angular velocity of frame $x_j y_j z_j$ in inertial space is given by $\dot{\psi}\hat{u}_{Z_o}$. Since the unit vectors $\hat{u}_{Z_o}$ and $\hat{u}_{z_j}$ in the inertial frame and in the $x_j y_j z_j$ frame, respectively, are equal,

$$\frac{d\hat{u}_{x_j}}{dt} = \dot{\psi}\hat{u}_{z_j} \times \hat{u}_{x_j} = \dot{\psi}\hat{u}_{y_j} \qquad (3-5)$$

and

$$\frac{d\hat{u}_{y_j}}{dt} = \dot{\psi}\hat{u}_{z_j} \times \hat{u}_{y_j} = -\dot{\psi}\hat{u}_{x_j} \qquad (3-6)$$

The $\hat{u}_{X_o}$ vector can be expressed as the sum of components in $\hat{u}_{x_j}$ and $\hat{u}_{y_j}$:

$$\hat{u}_{X_o} = \sin(\phi_j + \psi)\hat{u}_{x_j} - \cos(\phi_j + \psi)\hat{u}_{y_j} \qquad (3-7)$$

Combining Eq.'s (3-5), (3-6), and (3-7) with Eq. (3-4) yields

$$\vec{V}_{q_j} = \left[\dot{\eta}_o^L \sin(\phi_j + \psi) - y_j\dot{\psi} + \dot{\eta}_j\right]\hat{u}_{x_j} + \left[\eta_j\dot{\psi} - \dot{\eta}_o^L \cos(\phi_j + \psi)\right]\hat{u}_{y_j} \qquad (3-8)$$

The kinetic coenergy, T^*, of the system is the sum of kinetic coenergy terms arising from each component beam member,

$$T^* = \sum_{j=0}^{n} \frac{1}{2} m_j \int_0^L \vec{V}_j \bullet \vec{V}_j dy_j \qquad (3-9)$$

where $m_j = \rho_j A_j$ is the mass per unit length of the j'th beam, and torsional effects of the beam have been ignored. Assuming small motions Eq.'s (3-3) and (3-8) may be inserted into Eq. (3-9) giving

$$T^* = \frac{m_o}{2} \int_0^L \dot{\eta}_o^2 dy_o + \sum_{j=1}^{n} \left\{ \frac{m_j}{2} \int_0^L \left[\dot{\eta}_j^2 - 2\dot{\eta}_j \dot{\psi} y_j + 2\dot{\eta}_o^L \dot{\eta}_j \sin(\phi_j + \psi) \right] dy_j \right.$$
$$\left. + \frac{m_j}{2} \left[\frac{1}{3} L^3 \dot{\psi} + L \left(\dot{\eta}_o^L \right)^2 - L^2 \dot{\eta}_o^L \dot{\psi} \sin(\phi_j + \psi) \right] \right\} \qquad (3\text{-}10)$$

where higher order terms (greater than 2nd order) have been neglected and terms not containing $\dot{\eta}_j(y_j, t)$ were evaluated through the bounds of the integral.

The total potential strain energy of the system, $\mathcal{V}$, is determined based on the assumption that no shear strains are present, i.e. all structural members are modeled as Bernoulli-Euler beams. The total potential is given as

$$\mathcal{V} = \sum_{j=0}^{n} \left[\frac{1}{2} \int_0^L \int_{A_{bj}} E_{bj} \epsilon_{bj} \, dA_{bj} dy_j + \frac{1}{2} \int_0^L \int_{A_{fj}} E_{bj} \epsilon_{fj} \, dA_{fj} dy_j \right] \qquad (3-11)$$

where ϵ_{bj} and ϵ_{fj} are the axial strains of the beam and film layers, respectively, of the j'th component due to bending. A_{bj} and A_{fj} represent the cross-sectional areas of the beam and film layers of the j'th element; E_{bj} and E_{fj} are the Young's Moduli pertaining to each element. Assuming small transverse displacements, the normal strains for the beam and film sublayers of the j'th component become

$$\epsilon_{bj} = -x_j \frac{\partial^2 \eta_j}{\partial y_j^2} \qquad (3-12)$$

and

$$\epsilon_{fj} = -x_j \frac{\partial^2 \eta_j}{\partial y_j^2} + \epsilon_o \qquad (3-13)$$

where x_j is the distance in the $\hat{u}_{x_j}$ direction from the neutral axis to an arbitrary point within the beam/film composite. An initial prescribed prestrain, ϵ_o, has been

added to the elastic strain of the film to account for strain induced through the piezoelectric effect. Combining Eq.'s (3-12) and (3-13) with Eq. (3-11) gives

$$\mathcal{V} = \sum_{j=0}^{n} \left[\frac{1}{2} \int_0^L \int_{A_{bj}} E_{bj} x_j^2 \left(\frac{\partial^2 \eta_j}{\partial y_j^2} \right)^2 dA_{bj} dy_j + \frac{1}{2} \int_0^L \int_{A_{fj}} E_{bj} \left(-x_j \frac{\partial^2 \eta_j}{\partial y_j^2} + \epsilon_o \right)^2 dA_{fj} dy_j \right] . \tag{3-14}$$

The area moment of inertia of the j'th beam about its neutral axis is given by

$$I_{bj} = \int_{A_{bj}} x_j^2 dA_{bj} \tag{3-15}$$

and similarly the area moment of inertia for the film layer is

$$I_{fj} = \int_{A_{fj}} x_j^2 dA_{fj} \tag{3-16}$$

The total moment induced on the j'th structural element due to the film, M_{fj}, is

$$M_{fj} = \int_{A_{fj}} E_{fj} \epsilon_o x dA_{fj} \tag{3-17}$$

Eq. (3-14) may be combined with Eq.'s (3-15), (3-16), and (3-17) and reduced, giving the following expression for the strain energy of the system:

$$\mathcal{V} = \sum_{j=0}^{n} \left\{ \frac{1}{2} \int_0^L \left[(EI)_j \left(\frac{\partial^2 \eta_j}{\partial y_j^2} \right)^2 - 2 M_{fj} \frac{\partial^2 \eta_j}{\partial y_j^2} \right] dy_j + \int_0^L \int_{A_{fj}} \frac{1}{2} E_{fj} \epsilon_o^2 dA_{fj} dy_j \right\} \tag{3-18}$$

where $(EI)_j = (EI)_{bj} + (EI)_{fj}$.

The expressions for T^* (Eq. (3-10)) and $\mathcal{V}$ (Eq. (3-18)) are used in conjunction with Hamilton's Principle to arrive at the equations of motion for the system. Hamilton's Principle (Lagrange's Equation) is stated as

$$\int_{\bar{t}_1}^{\bar{t}_2} (\delta T^* - \delta \mathcal{V} + \Xi_j \delta \zeta_j) d\bar{t} = 0 \tag{3-19}$$

where Ξ_j are nonconservative forces not represented in the expression for $\mathcal{V}$. In this system it is assumed that arbitrary forces, $f_j(\bar{t})$, and arbitrary moments, $g_j(\bar{t})$, act on each element in the structure at the boundary point $y_j = L$. When applying the

calculus of variations to the potential strain energy term it is essential to realize that both $\delta\bar{t}_1$ and $\delta\bar{t}_2$ are equal to zero. The prescribed strain, ϵ_o, is constant and can not be varied. The equations of motion are found by varying $T^* - \mathcal{V}$ and integrating the result by parts in both space and time until the independent variational variables are no longer in differential form. When integrating by parts the geometric boundary constraints at $y_j = 0$ must be obeyed; namely, $\eta_j(0,t) = \dot{\eta}_j(0,t) = 0$ for all $j = 1, ..., n$. The following system of governing equations are derived ($j = 1, ..., n$):

$$\text{Beam 0}: \quad m_o\ddot{\eta}_o + (EI)_o\frac{\partial^4\eta_o}{\partial y_o^4} = \frac{\partial^2 M_{fo}}{\partial y_o^2} \tag{3-20}$$

$$\text{Beam j}: \quad m_j\ddot{\eta}_j + (EI)_j\frac{\partial^4\eta_j}{\partial y_j^4} - m_j y_j\ddot{\psi} + m_j\ddot{\eta}_o^L\sin(\phi_j + \psi) = \frac{\partial^2 M_{fj}}{\partial y_j^2} \tag{3-21}$$

The system is subject to the following natural boundary conditions at $y_o = L$:

$$\sum_{j=1}^{n}\left\{\frac{m_j L^2}{2}\ddot{\psi}\sin(\phi_j+\psi) - m_j L\ddot{\eta}_o - \int_0^L m_j\ddot{\eta}_j\sin(\phi_j+\psi)dy_j\right\} + (EI)_o\frac{\partial^3\eta_o}{\partial y_o^3} = \frac{\partial M_{fo}}{\partial y_o} + f_o(\bar{t}) \tag{3-22}$$

and

$$\sum_{j=1}^{n}\left\{\frac{m_j L^3}{3}\ddot{\psi} - \frac{m_j L^2}{2}\ddot{\eta}_o\sin(\phi_j+\psi) - \int_0^L m_j y_j\ddot{\eta}_j dy_j\right\} + (EI)_o\frac{\partial^2\eta_o}{\partial y_j^2} = M_{fo} + g_o(\bar{t}) \ . \tag{3-23}$$

The equations of motion also include two natural boundary constraints at $y_j = L$ ($j = 1, ..., n$):

$$(EI)_j\frac{\partial^2\eta_j}{\partial y_j^2} = M_{fj} + g_j(\bar{t}) \tag{3-24}$$

and

$$(EI)_j\frac{\partial^3\eta_j}{\partial y_j^3} = \frac{\partial M_{fj}}{\partial y_j} + f_j(\bar{t}) \ . \tag{3-25}$$

The equations of motion have been derived based on the assumptions of small motions and the absence of shear strains. Eq.'s (3-21) through (3-25) may be nondimensionalized according to the following new set of variables for j=1,...,n:

$$w_j = \frac{\eta_j}{L}$$

$$Y_j = \frac{y_j}{L}$$

$$t_j = K_j\bar{t} = \bar{t}\sqrt{\frac{(EI)_j}{m_jL^4}}$$

$$\tilde{M}_j = \frac{M_{fj}L}{(EI)_j}$$

The system equations in nondimensional form are written as

Equations of Motion:

$$\text{beam 0}: \quad \frac{\partial^2 w_o}{\partial t_o^2} + \frac{\partial^4 w_o}{\partial Y_o^4} = \frac{\partial^2 \tilde{M}_o}{\partial Y_o^2} \tag{3-26}$$

$$\text{beam j}: \quad \frac{\partial^2 w_j}{\partial t_j^2} + \frac{\partial^4 w_j}{\partial Y_j^4} - Y_j\frac{\partial^2 \psi}{\partial t_j^2} + \sin(\phi_j + \psi)\frac{\partial^2 w_o}{\partial t_j^2}(1, t_j) = \frac{\partial^2 \tilde{M}_j}{\partial Y_j^2} \tag{3-27}$$

Natural Boundary Conditions at $Y_o = 1$:

$$\sum_{j=1}^{n}\left\{ \tfrac{1}{2}\sin(\phi_j+\psi)\tfrac{\partial^2\psi}{\partial t_j^2} - \tfrac{\partial^2 w_o}{\partial t_j^2} - \int_0^1 \sin(\phi_j+\psi)\tfrac{\partial^2 w_j}{\partial t_j^2}dY_j \right\} + \tfrac{\partial^3 w_o}{\partial Y_o^3} = \tfrac{\partial \tilde{M}_o}{\partial Y_o} + f_o(t_o) \tag{3-28}$$

and

$$\sum_{j=1}^{n}\left\{ \tfrac{1}{3}\tfrac{\partial^2\psi}{\partial t_j^2} - \int_0^1 \tfrac{\partial^2 w_j}{\partial t_j^2}Y_j dY_j - \tfrac{1}{2}\sin(\phi_j+\psi)\tfrac{\partial^2 w_o}{\partial t_j^2} \right\} + \tfrac{\partial^2 w_o}{\partial Y_o^2} = \tilde{M}_o + g_o(t_o) \tag{3-29}$$

Natural Boundary Conditions at $Y_j = 1$ $(j = 1, ..., n)$:

$$\frac{\partial^3 w_j}{\partial Y_j^3} = \frac{\partial \tilde{M}_j}{\partial Y_j} + f_j(t_j) \tag{3-30}$$

and

$$\frac{\partial^2 w_j}{\partial Y_j^2} = \tilde{M}_j + g_j(t_j) \tag{3-31}$$

3.2 *Smart* Structures Control Strategy

In this section the *smart* structures control strategy is derived based on Lyapunov's second method [23]. Distributed actuator and sensor governing equations are combined with the Lyapunov functional time derivative to arrive at a *smart*

component control law which guarantees the controllability of the global system. It is assumed that the (undamped) generalized structure does not contain any unstable modes. The (nondimensionalized) Lyapunov energy functional pertaining to the generalized structure is given as

$$F = \frac{1}{2}\int_0^1 \left[\left(\frac{\partial^2 w_o}{\partial Y_o^2}\right)^2 + \left(\frac{\partial w_o}{\partial t_o}\right)^2 \right] dY_o + \sum_{j=1}^{n} \frac{1}{2}\int_0^1 \left[\left(\frac{\partial^2 w_j}{\partial Y_j^2}\right)^2 + \left(\frac{\partial w_j}{\partial t_j} - Y_j \frac{\partial \psi}{\partial t_j} + \sin(\phi_j + \psi)\frac{\partial w_o}{\partial t_j}(1, t_j)\right)^2 \right] dY_j \,. \quad (3\text{-}32)$$

This functional is valid for small motions only: terms greater than second order have been neglected in order to be consistent with the assumptions made in deriving the equations of motion. The first and second terms in the first integral represent the potential strain and kinetic energies of the base beam, respectively. The first and second terms in the second integral represent the potential strain and kinetic energies of the j'th element. Differentiating the functional with respect to time gives an expression for the power in the system:

$$\dot{F} = \int_0^1 \left[\frac{\partial^2 w_o}{\partial Y_o^2}\frac{\partial^3 w_o}{\partial Y_o^2 \partial t_o} + \frac{\partial w_o}{\partial t_o}\frac{\partial^2 w_o}{\partial t_o^2} \right] dY_o + \sum_{j=1}^{n} \int_0^1 \left\{ \left[\frac{\partial w_j}{\partial t_j} - Y_j \frac{\partial \psi}{\partial t_j} + \sin(\phi_j + \psi)\frac{\partial w_o}{\partial t_j}(1, t_j) \right] \left[\frac{\partial^2 w_j}{\partial t_j^2} - Y_j \frac{\partial^2 \psi}{\partial t_j^2} + \sin(\phi_j + \psi)\frac{\partial^2 w_o}{\partial t_j^2}(1, t_j) \right] + \frac{\partial^2 w_j}{\partial Y_j^2}\frac{\partial^3 w_j}{\partial Y_j^2 \partial t_j} \right\} dY_j \,. \quad (3\text{-}33)$$

The equations of motion (Eq.'s (3-26) and (3-27)) can be substituted into the above expression to replace the kinetic energy time derivative terms:

$$\dot{F} = \int_0^1 \left[\frac{\partial^2 w_o}{\partial Y_o^2}\frac{\partial^3 w_o}{\partial Y_o^2 \partial t_o} + \frac{\partial w_o}{\partial t_o}\left(\frac{\partial^2 \tilde{M}_o}{\partial Y_o^2} - \frac{\partial^4 w_o}{\partial Y_o^4} \right) \right] dY_o + \sum_{j=1}^{n} \int_0^1 \left\{ \left[\frac{\partial w_j}{\partial t_j} - Y_j \frac{\partial \psi}{\partial t_j} + \sin(\phi_j + \psi)\frac{\partial w_o}{\partial t_j}(1, t_j) \right] \left[\frac{\partial^2 \tilde{M}_j}{\partial Y_j^2} - \frac{\partial^4 w_j}{\partial Y_j^4} \right] + \frac{\partial^2 w_j}{\partial Y_j^2}\frac{\partial^3 w_j}{\partial Y_j^2 \partial t_j} \right\} dY_j \,. \quad (3\text{-}34)$$

Differentiating both integrals by parts twice gives

$$\dot{F} = \int_0^1 \frac{\partial^3 w_o}{\partial Y_o^2 \partial t_o} \tilde{M}_o dY_o + \sum_{j=1}^{n} \int_0^1 \frac{\partial^3 w_j}{\partial Y_j^2 \partial t_j} \tilde{M}_j dY_j$$
$$+ \frac{\partial w_o}{\partial t_o} \left(\frac{\partial \tilde{M}_o}{\partial Y_o} - \frac{\partial^3 w_o}{\partial Y_o^3} \right) \Bigg|_{Y_o=0}^{Y_o=1} - \frac{\partial^2 w_o}{\partial Y_o \partial t_o} \left(\tilde{M}_o - \frac{\partial^2 w_o}{\partial Y_o^2} \right) \Bigg|_{Y_o=0}^{Y_o=1}$$
$$+ \sum_{j=1}^{n} \left\{ \left[\frac{\partial w_j}{\partial t_j} - Y_j \frac{\partial \psi}{\partial t_j} + \sin(\phi_j + \psi) \frac{\partial w_o}{\partial t_j}(1, t_j) \right] \left[\frac{\partial \tilde{M}_j}{\partial Y_j} - \frac{\partial^3 w_j}{\partial Y_j^3} \right] \Bigg|_{Y_j=0}^{Y_j=1} \right.$$
$$\left. - \left[\frac{\partial^2 w_j}{\partial Y_j \partial t_j} - \frac{\partial \psi}{\partial t_j} \right] \left[\tilde{M}_j - \frac{\partial^2 w_j}{\partial Y_j^2} \right] \Bigg|_{Y_j=0}^{Y_j=1} \right\} . \qquad (3\text{-}35)$$

Finally Eq. (3-35) may be combined with the natural boundary constraints of the system (Eq.'s (3-28)-(3-31)) to give the result

$$\dot{F} = \sum_{j=0}^{n} \int_0^1 \frac{\partial^3 w_j}{\partial Y_j^2 \partial t_j} \tilde{M}_j dY_j + fcn \sum_{j=0}^{n} \left[\frac{\partial w_j}{\partial t_j}(1, t_j), \frac{\partial^2 w_j}{\partial Y_j \partial t_j}(1, t_j), \frac{\partial^2 w_j}{\partial t_j^2}(1, t_j), \frac{\partial^3 w_j}{\partial Y_j \partial t_j^2}(1, t_j), f_j(t_j), g_j(t_j) \right] . \qquad (3-36)$$

Eq. (3-36) shows that regardless of the energetic interactions between components in the large structure the moment induced by the film only appears in the spatial integral term. Recall that the (nondimensionalized) piezoelectrically induced moment is proportional to the (nondimensionalized) film voltage and varies in both space and time:

$$\tilde{M}_j = V_{oj} \Lambda(Y_j) \rho(t_j) \qquad (3-37)$$

where V_{oj} is the gain of the control signal for the j'th component. Combining Eq. (3-37) with Eq. (3-36) and ignoring the boundary terms since they are independent of $\tilde{M}_j$ gives

$$\dot{F} = \sum_{j=0}^{n} \left[V_{oj} \rho_j(t_j) \int_0^1 \frac{\partial^3 w_j}{\partial Y_j^2 \partial t_j} \Lambda(Y_j) dY_j \right] . \qquad (3-38)$$

The film sensor governing equation for the j'th component follows directly from Eq. (2-23):

$$(\tilde{V}_f)_j = - \int_0^1 \frac{\partial^2 w_j}{\partial Y_j^2}(Y_j, t_j) \, \Lambda_j(Y_j) \, dY_j . \qquad (3-39)$$

In order to extract energy from the global system each structural component is *autonomously* controlled according to the following control law for the j'th component:

$$\rho_j(t_j) = \frac{d}{dt_j}\left(\tilde{V}_f\right)_j \quad . \tag{3-40}$$

Applying Eq. (3-40) by differentiating Eq. (3-39) and substituting the result into Eq. (3-38) gives

$$\dot{F} = -\sum_{j=0}^{n}\left[V_{oj}\left\{\int_0^1 \frac{\partial^3 w_j}{\partial Y_j^2 \partial t_j}\Lambda(Y_j)dY_j\right\}^2\right] \quad . \tag{3-41}$$

Eq. (3-41) shows that if each smart component is independently controlled according to the control law stated in Eq. (3-40) then the multi-component structure can not be destabilized since energy is always removed from the global system. Because the negative definiteness of Eq. (3-41) the system is certain to be stabilizable, although the character and effectiveness of the global control strategy will ultimately be determined by the choice of spatial distributions and actuator orientations. It is important to note that at worst a poor choice in transducer shapes will render certain modes uncontrollable but will not provide excitation to these modes. It has been assumed that all eigenvalues of the undamped structure are nonpositive. The result also implies that for systems of even greater complexity the same control law will still provide global stability. For instance, a system where an arbitrary number of additional beams were rigidly joined to the free end of the n'th component ($n \neq 0$) of the current structure will lead to a new set of boundary terms at $Y_n = 1$ to replace the $f_n(t_n)$ and $g_n(t_n)$ forcing functions. These terms will be similar to the natural boundary constraints that exist at $Y_o = 1$ of the current system. New coupling terms will appear in the equations of motion that will also appear as kinetic energy terms in the Lyapunov functional: these terms will vanish in the final result through the substitution of the equations of motion into the Lyapunov functional time derivative.

3.3 Smart Component Spatial Distributions

By choosing different PVF_2 electrode spatial distributions for the component members, it becomes possible to implement a controller that can control all modes

of a structure simultaneously or provide vibrational attenuation to a selected modal subset. In order to develop a methodology for choosing an effective combination of spatial distributions and actuator orientations, it is first necessary to approach a specific example system. Consider the simple structure shown in Fig 3-2, in which two smart components are rigidly joined at a common boundary and clamped at opposing ends. It is assumed that both components are characterized by the identical geometric and material constants. The specific constraints described in section 2.3 regarding the geometry and polarity of each component necessarily apply to this example system. The Lyapunov functional for the structure can be written as the superposition of functionals corresponding to each functional member:

$$F = \frac{1}{2}\int_{-1}^{0}\left(\frac{\partial^2 w_1}{\partial Y^2}\right)^2 + \left(\frac{\partial w_1}{\partial t}\right)^2 dY + \frac{1}{2}\int_{0}^{1}\left(\frac{\partial^2 w_2}{\partial Y^2}\right)^2 + \left(\frac{\partial w_2}{\partial t}\right)^2 dY \,. \quad (3-42)$$

Taking the time derivative of the above expression yields

$$\begin{aligned}\frac{dF}{dt} = &\int_{-1}^{0}\left\{\left(\frac{\partial^2 w_1}{\partial Y^2}\right)\left(\frac{\partial^3 w_1}{\partial^2 Y \partial t}\right) + \left(\frac{\partial w_1}{\partial t}\right)\left(\frac{\partial^2 w_1}{\partial t^2}\right)\right\} dY \\ &+ \int_{0}^{1}\left\{\left(\frac{\partial^2 w_2}{\partial Y^2}\right)\left(\frac{\partial^3 w_2}{\partial^2 Y \partial t}\right) + \left(\frac{\partial w_2}{\partial t}\right)\left(\frac{\partial^2 w_2}{\partial t^2}\right)\right\} dY \,. \end{aligned} \quad (3\text{-}43)$$

Eq. (3-43) is reduced by applying the equation of motion (Eq. (2-14)) to eliminate the transverse linear acceleration terms, integrating by parts, and applying the boundary constraints. The resulting expression for $\frac{dF}{dt}$ becomes

$$\frac{dF}{dt} = \int_{-1}^{0}\left(\frac{\partial^3 w_1}{\partial^2 Y \partial t}\right) V_1 dY + \int_{0}^{1}\left(\frac{\partial^3 w_2}{\partial^2 Y \partial t}\right) V_2 dY \quad (3-44)$$

which is a restatement of the generalized expression (Eq. (3-36)) for this particular system. If the control input is restated according to Eq. (2-21) then

$$\frac{dF}{dt} = V_{o1}\rho_1(t)\int_{-1}^{0}\left(\frac{\partial^3 w_1}{\partial^2 Y \partial t}\right)\Lambda_1 dY + V_{o2}\rho_2(t)\int_{0}^{1}\left(\frac{\partial^3 w_2}{\partial^2 Y \partial t}\right)\Lambda_2 dY \quad (3-45)$$

which is similar to Eq. (3-38).

Eq. (3-45) is suited for exploring various choices in smart component actuator shapes and global geometries. As a first case, consider the application of two smart

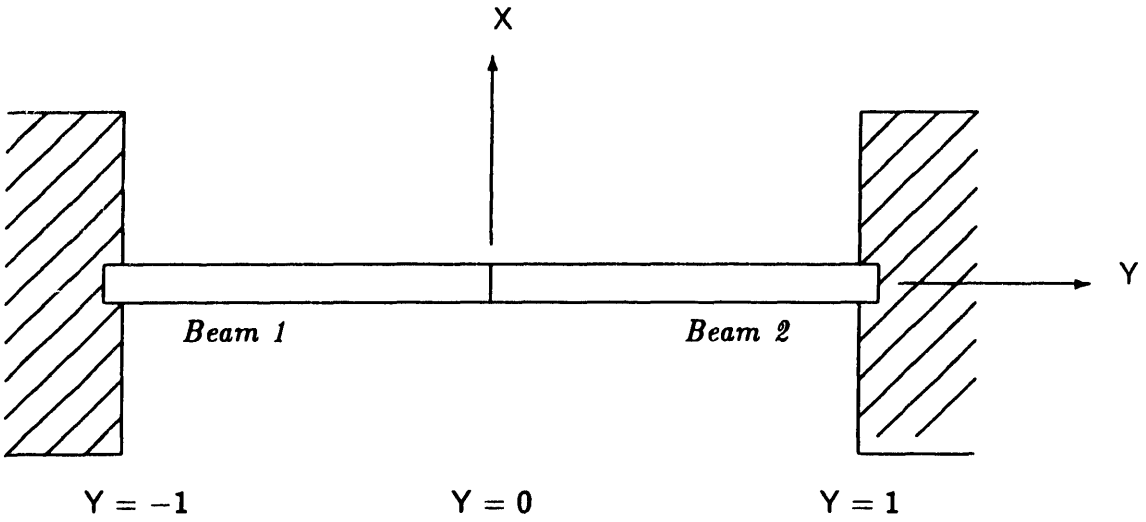

Figure 3-2. Simple structure in which two smart components are rigidly joined at a common boundary and clamped at opposing ends.

structural components in which the candidate actuator (and sensor) electrode shape is a uniform distribution described by Eq. (2-26) and shown in Fig. 2-3. There are two possible global geometries, schematically depicted in Fig.'s 3-3 and 3-4. In Fig. 3-3 both smart components would be arranged so that their PVF_2 actuator layers are directly adjacent to each other. In Fig 3-4 both PVF_2 layers would be on opposing sides of the neutral axis of the composite structure. If the geometry shown in Fig. 3-3 is implemented and the polarity constraints are obeyed, then enforcing clamped boundary constraints allows Eq. (3-45) to be reduced to

$$\frac{dF}{dt} = V_{o1}\rho_1(t)\frac{\partial^2 w_1}{\partial Y \partial t}(0,t) - V_{o2}\rho_2(t)\frac{\partial^2 w_2}{\partial Y \partial t}(0,t) \quad . \qquad (3-46)$$

Obeying the control law (Eq. (3-40)) yields

$$\rho_1(t) = -\frac{\partial^2 w_1}{\partial Y \partial t}(0,t) \qquad (3-47)$$

and

$$\rho_2(t) = +\frac{\partial^2 w_2}{\partial Y \partial t}(0,t) \quad . \qquad (3-48)$$

If the constitutive constants Q_o and C_f are the same for both smart components then $\rho_1(t) = -\rho_2(t)$ since $w_1(0,t) = w_2(0,t)$. Therefore if the control amplitudes

V_{o1} and V_{o2} are equal to unity then the functional time derivative reduces to

$$\frac{dF}{dt} = -2\left[\frac{\partial^2 w_1}{\partial Y \partial t}(0,t)\right]^2 \quad . \qquad (3-49)$$

Eq. (3-49) is negative for all even-order modes and zero for all odd-order modes since odd modes are characterized by vanishing angular velocity at $Y = 0$. The geometry in Fig. 3-3 therefore provides controllability to even modes only.

If the geometry in Fig. 3-4 is implemented then $\rho_2(t) = \rho_1(t)$ where $\rho_1(t)$ is given by Eq. (3-47). Eq. (3-45) becomes

$$\frac{dF}{dt} = V_{o1}\rho_1(t)\frac{\partial^2 w_1}{\partial Y \partial t}(0,t) + V_{o2}\rho_2(t)\frac{\partial^2 w_2}{\partial Y \partial t}(0,t) \qquad (3-50)$$

which for this geometry reduces to

$$\frac{dF}{dt} = -2\left[\frac{\partial^2 w_1}{\partial Y \partial t}(0,t)\right]^2 \quad . \qquad (3-51)$$

This distribution, like the distribution in Fig. 3-3, allows for point moment control at the midspan, which will provide controllability for all even-order modes since all even modes exhibit a non-zero slope at the center. Odd order modes of the structure are not controllable using either geometry since they are characterized by vanishing slope at the midspan. It is important to realize that it makes no difference on which side of the structure the actuators are situated relative to each other: as long as the polarity constraints (section 2.3) and the control law (Eq. (3-40)) are obeyed then energy will be actively dissipated for the even modes regardless of which of the two configurations are chosen.

It is possible to control all modes of the structure using smart structural components in which the film distribution is the linearly-varying film shape described by Eq. (2-27). The geometric configuration shown in Fig. 3-5 was chosen in which the component actuator (and sensor) distributions are linearly varying. Implementing the control law (Eq. (3-40)) for each smart component yields

$$\rho_1(t) = -\frac{\partial w_1}{\partial t}(0,t) \qquad (3-52)$$

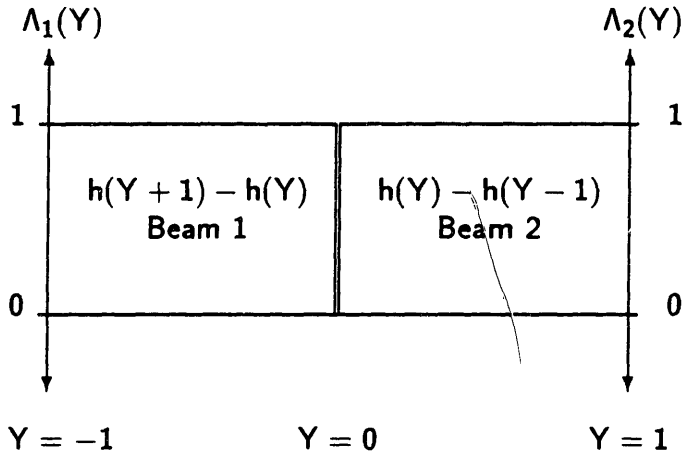

Figure 3-3. Choice for smart component film layer spatial geometries for control of the global system.

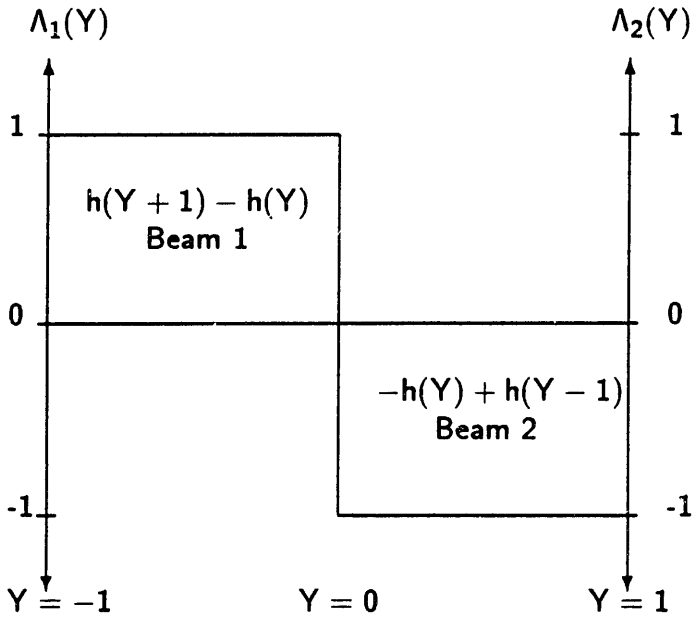

Figure 3-4. Choice of smart component film layer spatial geometries for control of the global system

and

$$\rho_2(t) = -\left[\frac{\partial^2 w_2}{\partial Y \partial t}(0,t) - \frac{\partial w_2}{\partial t}(0,t)\right] \quad . \qquad (3-53)$$

Odd-order modes are characterized by zero slope at the midpoint while even modes are characterized by vanishing linear displacement at the center. Thus for odd modes,

$$\rho_1(t) = -\rho_2(t) = -\frac{\partial w_1}{\partial t}(0,t) \qquad (3-54)$$

where the constitutive geometric and piezoelectric parameters for both components are assumed to be identical. For even modes $\rho_1(t) = 0$ and $\rho_2(t)$ is given by

$$\rho_2(t) = -\frac{\partial^2 w_2}{\partial Y \partial t}(0,t) \quad . \qquad (3-55)$$

The Lyapunov functional time derivative is found by applying the spatial actuator configuration to Eq. (3-45):

$$\frac{dF}{dt} = V_{o1}\rho_1(t)\frac{\partial w_1}{\partial t}(0,t) + V_{o2}\rho_2(t)\left[\frac{\partial^2 w_2}{\partial Y \partial t}(0,t) - \frac{\partial w_2}{\partial t}(0,t)\right] \qquad (3-56)$$

Assuming that the control gains V_{o1} and V_{o2} are unity then for odd modes Eq.'s (3-54) and (3-56) may be combined to give

$$\frac{dF}{dt} = -2\left[\frac{\partial w_1}{\partial t}(0,t)\right]^2 \qquad (3-57)$$

and for even modes Eq.'s (3-55) and (3-56) may be combined to give

$$\frac{dF}{dt} = -\left[\frac{\partial w_2}{\partial Y \partial t}(0,t)\right]^2 \quad . \qquad (3-58)$$

The two preceding equations demonstrate that the linearly-varying electrode distribution actively removes energy from all modes of the system ; however, twice as much energy is dissipated for odd-modes relative to even modes. This example shows that different spatial geometries can be chosen in which the control authority of certain modes or modal subsets is weighted more than others.

In this specific example it has been shown that in order to provide controllability to all modes of the system it is necessary to implement a distribution where both

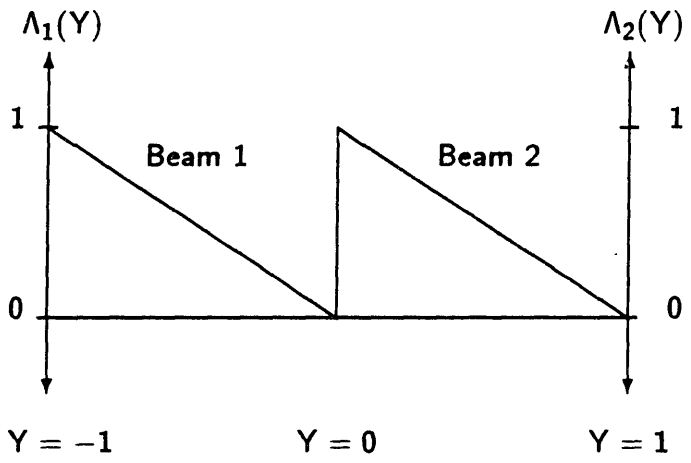

Beam 1: $\Lambda_1(Y) = -Y\,[h(Y+1) - h(Y)]$
Beam 2: $\Lambda_2(Y) = (1-Y)\,[h(Y) - h(Y-1)]$

Figure 3-5. Choice for smart component film layer spatial geometries for control of the global system.

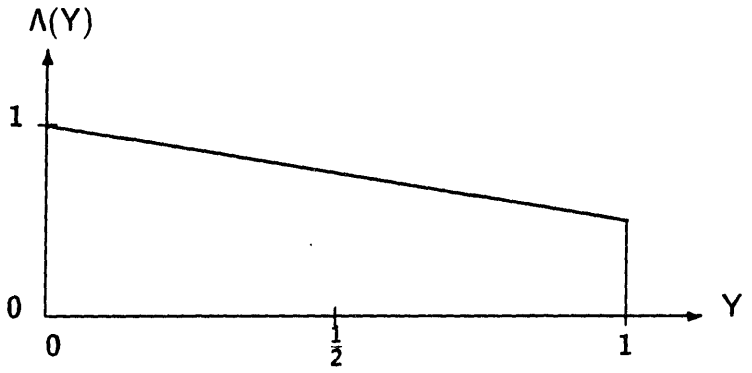

Figure 3-6. "Universal" distribution, which gives rise to both point forces and point moments at each boundary.

moments and forces are generated at the common junction between the component members. The boundary constraints of complex multi-component structures generally will not be known *a priori.* Therefore control of complex *smart* structures often necessitates choosing distributions where both control moments and forces are generated at all structural junctions. In many cases the uniform and/or linearly varying distributions will suffice and possibly provide the most effective control for a given system. For simplicity it is often preferable to choose a single PVF_2 film shape to be used for every component member. The "universal" distribution shown in Fig. 3-6 is applicable in most cases as a viable choice in film shape to provide damping to the large structure. The distribution is essentially a combination between the linearly-varying and uniform distributions presented earlier. The universal distribution has the attribute of providing both force and moment actuation at both boundaries. The universal distribution will therefore preserve the characteristic of providing active damping to all modes of most structural configurations.

In general if one has knowledge of the modeshapes of a superstructure then an arrangement of PVF_2 transducer shapes can be chosen to control all modes of that structure. Consider the "Y-structure" shown in Fig. 3-7 (this structure was

constructed in the laboratory and is discussed in section 5.2). This system consists of two smart components which are rigidly joined to the free end of a cantilevered third component. The system obeys the equations of motion given in Eq.'s (3-26) through (3-31) for the case of $n = 2$ (recall the base beam is assigned "beam 0"*). Dynamic analysis shows that all modes of this system are characterized by non-zero slope at every point $Y_j = 1$, for all $j = 0, 1, 2$. Therefore point force boundary control is not required and a simple strategy for providing active damping to *all* structural modes is to use three smart components with uniformly distributed PVF_2 transducers (Fig. 2-3). In this way control moments are provided at all $Y_j = 1$. In the experimental analysis section this strategy is demonstrated to be effective in providing active damping to the first four modes of the structure.

*In this chapter the base beam has been assigned "beam 0", while in the sections 5.2 and 6.1 the base beam of the Y-structure will be assigned "beam 1". I apologize for the confusion.

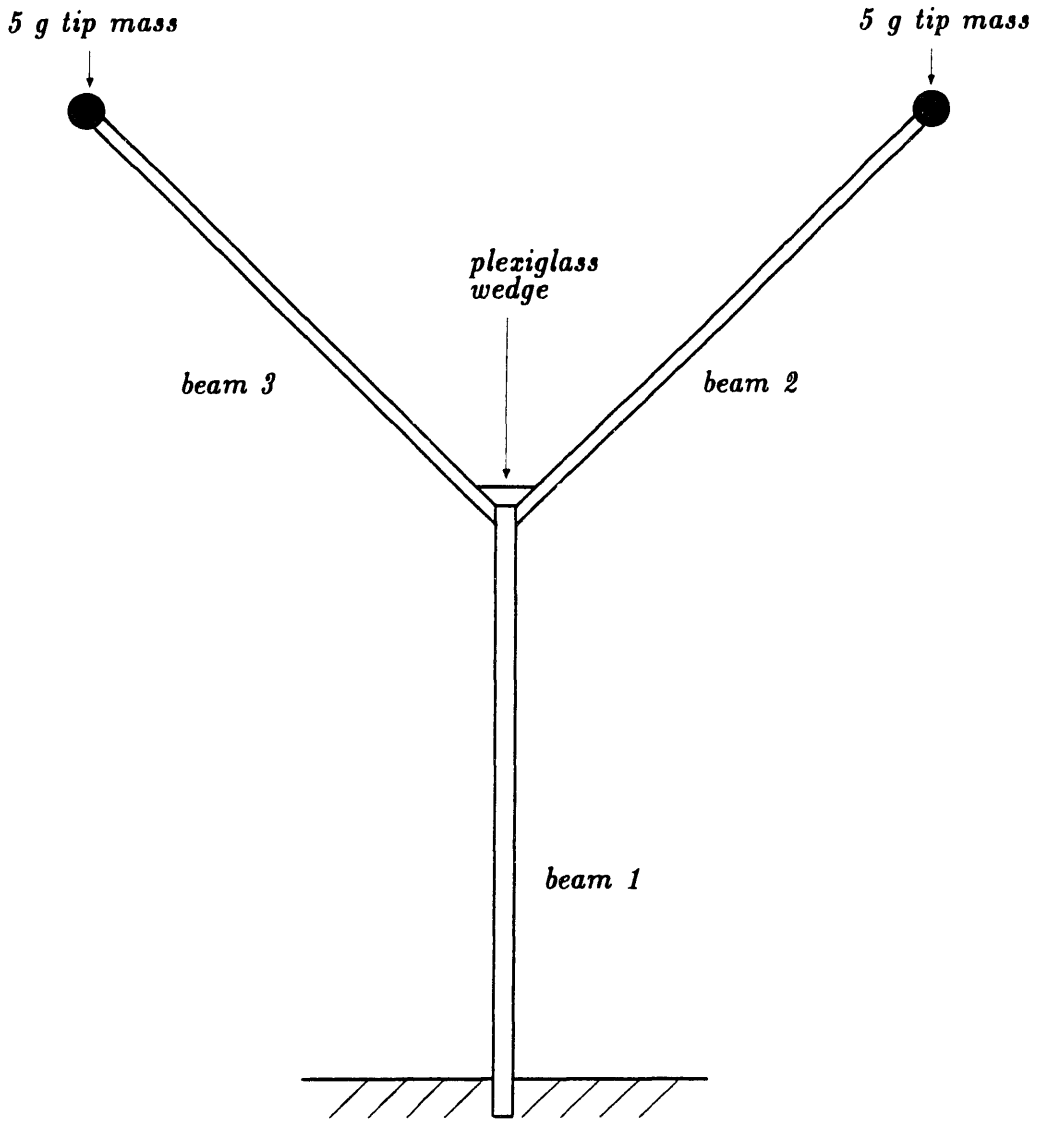

Figure 3-7. A three component system which demonstrates the utility of using uniformly distributed PVF_2 transducer layers for vibration control. All three smart components are fastened to a plexiglass wedge as shown.

3.4 Design Guidelines for the Application of Smart Components

The results of presented thus far are summarized in this section in the form of a set of design guidelines for applying smart structural components to large structures.

1) Each smart structural component must be designed so that (a) the polarity vector of both actuator and sensor layers point toward the neutral axis of the beam member, (b) both actuator and sensor electric field distributions are identical in shape and in orientation on the structure, and (c) the time derivative of the sensor output is used as the control signal for the actuator.

2) The electric fields of the PVF_2 transducers may be spatially varied to control all modes of a structure simultaneously or to control a desired subset of modes. Varying the electric field is accomplished through shaping the electrode deposition layer or by allowing the thickness of the film layer to vary spatially.

3) Uniform distributions are effective for many structural geometries. It may be preferable to use uniformly distributed film layers because they are simple to construct.

4) Discontinuites in the amplitude of the PVF_2 actuator electrode layer result in point moments and discontinuities in slope result in point forces. The magnitude of the amplitude and slope discontinuities dictates the weighting of the boundary control action produced by film actuators. In many instances the location of the discontinuities may be varied to implement a control function that will weight certain modes more heavily than others.

5) Discontinuites in the amplitude of the PVF_2 sensor electrode layer result in point angular displacement measurements and discontinuities in slope result in point linear displacement measurements.

6) If the dynamic behavior of a multi-component structure is completely unknown then the "universal" distribution can be applied, which has the characteristic of producing forces and moments at all boundary points. In most instances this distribution will succeed in providing active damping to all structural modes.

Chapter 4

Experimental Verification of Distributed Sensor Model

4.1 Spatially Uniform Sensor on a Cantilever Beam

In this chapter the governing distributed sensor relation is verified experimentally for both uniform and linearly varying film shapes. Radiative cross-coupling effects are addressed, which arise when both distributed sensors and actuators are located on the same strucutral component. Verification of the distributed actuator theory presented in section 2.2 is not included here but is provided in several references [1,6,8,21,22].

The sensor model (Eq. (2-23)) was verified for a spatially uniform distribution applied to a cantilever beam. The beam parameters are provided in Table 4-1. The experimental configuration is shown in Fig. 4-1. A 35 gram Endevco 7302B angular accelerometer was mounted on the tip. The shielded accelerometer leads were extended above the beam and clamped in order to minimize their effect on the beam vibrations. Uniaxially polarized PVF_2 film (28μm thickness) was bonded to the steel beam using Eccobond 45LV, a low viscosity epoxy. The average thickness of the adhesive layer was measured and found to be $\approx$ 12μm. The PVF_2 sensor electrode was constructed by soldering a lead wire to a thin copper tab, and was adhered to the electroplated film surface with conductive epoxy. An Electro 3030S20 magnetic coil was used as an actuator to excite the beam/film composite structure. The magnetic actuator has the advantage that it is small and non-invasive. However, the coil can not tolerate large voltages and therefore can not induce large forces.

The sensor model (Eq. (2-23)) predicts that a spatially uniform film distribution on a cantilever beam will sense angular tip displacement, $\frac{\partial w}{\partial Y}(1,t)$. To verify this

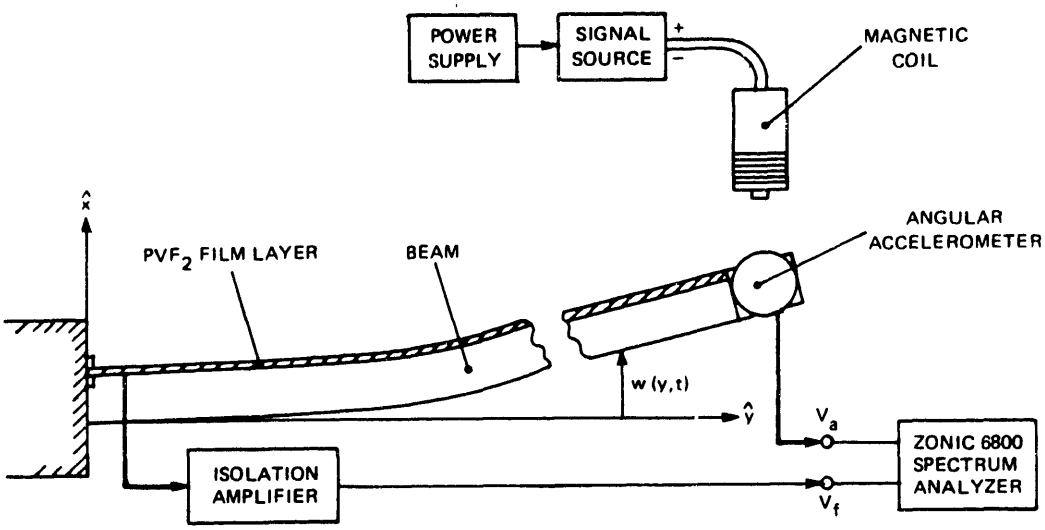

Figure 4-1. Experimental configuration for the uniform sensor analysis.

result, the beam composite was excited with the magnetic coil through a sinusoidal sweep from 15 to 60 Hz, and a Zonic 6800 structural analyzer was used to correlate the accelerometer and film sensor signals. Because the film behaves as an electrical capacitor with a large input impedance, the isolation amplifier shown in Fig. 4-2 was used to precondition the film output.

A spatially uniform sensor obeys Eq. (2-28). With the clamped boundary condition at $Y = 0$ and with the dynamics of the isolation amplifier circuit included in the model, Eq. (2-28) becomes

$$V_f(s) = -Q_0 \left(\frac{R_b s}{R_b C_f s + 1} \right) \frac{\partial w}{\partial Y}(1, s) \qquad (4-1)$$

where the tip angular displacement has been transformed into the frequency domain, s is the Laplace operator, R_b is the resistance associated with the isolation amplifier circuit (see Fig. 4-2), and C_f is the film capacitance. The angular accelerometer obeys the equation,

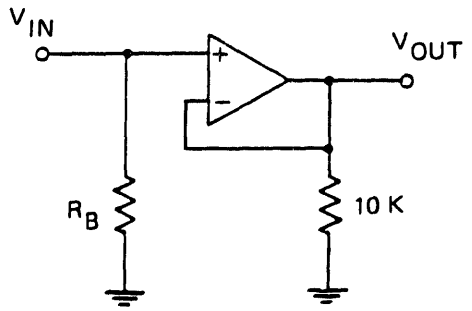

Figure 4-2. Operational amplifier buffer circuit.

$$V_a(s) = G_a s^2 \frac{\partial w}{\partial Y}(1, s) \qquad (4-2)$$

where V_a is the accelerometer output voltage and G_a is the accelerometer gain. Combining the two preceding equations gives

$$\frac{V_a}{V_f} = -\frac{G_a s}{Q_0}\left(\frac{R_b C_f s + 1}{R_b}\right) \qquad (4-3)$$

which is the analytical governing equation for this experimental analysis.

The necessary parameters are given in Table 4-1. The values for the piezoelectric constants, k_{31} and g_{31} are average values supplied by the film manufacturer [16]. The film capacitance and resistance were measured in the laboratory. The angular accelerometer was calibrated and adjusted so that its sensitivity was 1.67 mV/$\frac{\text{rad}}{\text{sec}^2}$. The distance from the neutral axis to the film surface, D, was calculated from Eq. (2-2), and its value is approximately $\frac{h_b}{2}$. The thickness of the epoxy layer was ignored since its thickness is much less than that of the beam. The charge constant was then calculated from the values of the appropriate constants supplied in the table, and was found to be 1.61×10^{-7} Coulombs.

The structure was excited through a continuous sinusoidal sweep from 15 to 60 Hz. The first two vibrational modes were found to occur at 2.2 Hz and 33.75 Hz. The analysis was limited to this frequency range because at low frequencies and at frequencies greater than 60 Hz the magnetic actuator was unable to induce sufficient angular acceleration, resulting in poor coherence and therefore unreliable

parameter	*Beam*	PVF_2	*Other*
Modulus, E, $N \cdot m^2$	$210x10^9$	$2.0x10^9$	
Length, L, m	0.140	0.140	
Thickness, h, mm	$h_b = .381$	$h_f = .028$	
Width, b_0, mm	12.7	12.7	
Density, ρ, kgm^{-3}	7800	1800	
Film Capacitance, C_f, nF		5.03	
Film Resistance, MΩ		> 7000	
g_{31}, $\frac{m^2}{Coul}$		$\cong 216x10^{-3}$	
Coupling Factor, k_{31}		$\cong 12\%$	
Buffer Resistance, R_b			80MΩ
Accelerometer Gain, G_a			$1.67mV/\frac{rad}{sec^2}$
Dist. from n. axis, D, μm			190.64
Q_0, Coulombs			$1.61x10^{-7}$

Table 4-1. Uniform Sensor Analysis Experimental Parameters

data. Fig. 4-3 shows the data from the continuous sweep experiment. The figure shows both magnitude and phase relationships between the accelerometer and the film sensor. The model predicts that both sensors should produce signals which are always in phase (except near 0 Hz, from Eq. (4-3)). In Fig. 4-3 the actual data is shown as a solid line. The dashed lines are analytical results for which the electromechanical coupling factor, k_{31}, is 12%, while the hash-marked lines are theoretical results for which $k_{31} \approx 7\%$. The 12% value for k_{31} given in Table 4-1 is an upper bound provided by the manufacturer which suggests perfect adhesion of the film to the bonded surface. This is an idealization which is unacceptable in actual practice. Technical data on PVF_2 film shows that the coupling factor typically will be less than 12% in the frequency bandwidth of this analysis [16].

The results shown in Fig. 4-3 validate Eq. (2-23) through this frequency range for this structural configuration. The analysis range was limited due to the inability of the magnetic actuator to provide sufficient excitation at frequencies outside of bandwidth of the experiment. Results which follow will support the model for other configurations and broader frequency ranges.

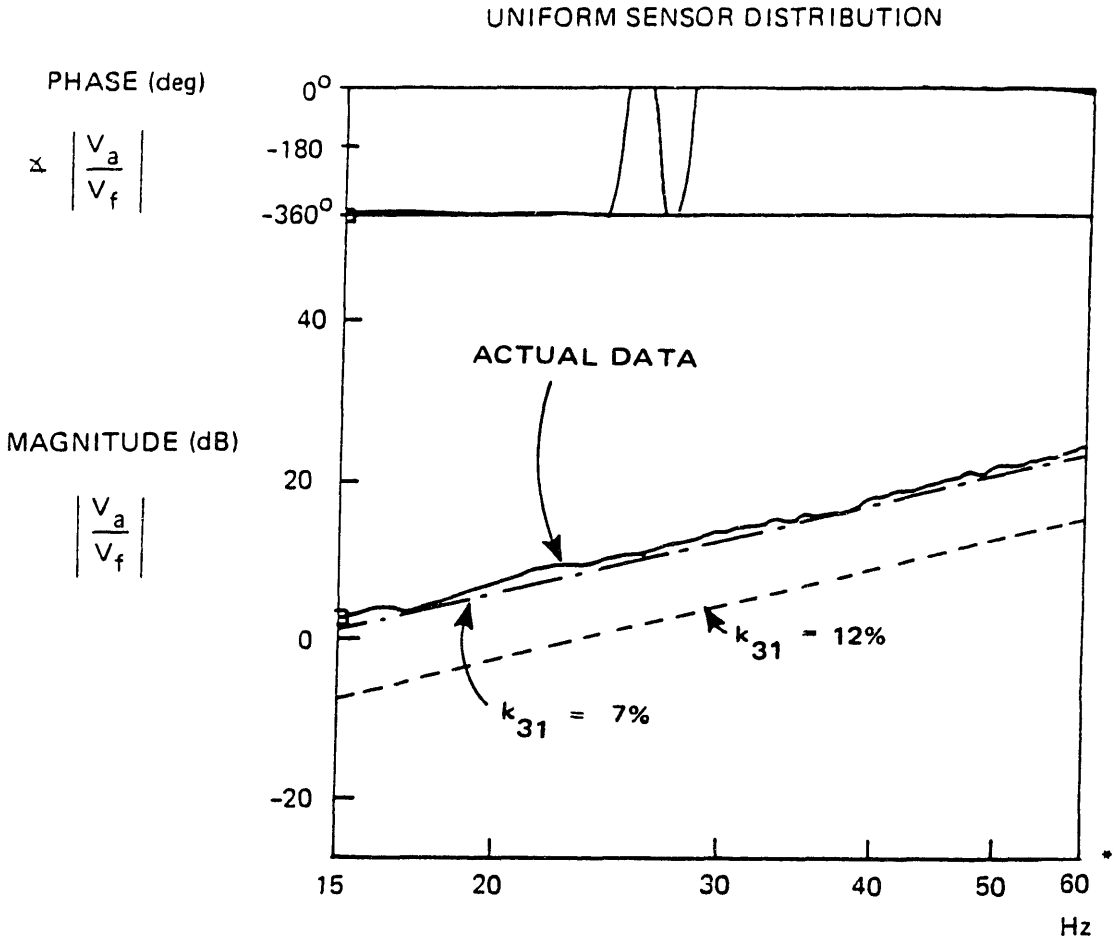

Figure 4-3. Uniform sensor distribution results, 15 to 60 Hz data.

4.2 Linearly-varying Sensor on a Cantilever Beam

The sensor model was tested for a linearly-varying distribution (Eq. (2-27)) applied to a cantilever beam. A $\frac{1}{2}$ gram Entran EGA-125 linear accelerometer was mounted on the tip. The accelerometer leads were extended above the structure and clamped to minimize their effect on the beam vibrations. The experimental configuration and procedure was identical to the configuration described in the preceding section.

A sideview of the linearly-varying sensor/beam composite is depicted in Figure 4-4. Instead of spatially varying the electrode on the film surface, it was deemed permissible to *cut* the uniformly plated film into the desired spatial configuration and adhere it to the beam. The stiffness and thickness of the PVF_2 layer are both much less than that of the steel beam, and therefore it was assumed that the strain relation given in Eq. (2-1) is still valid. The experimental results which follow support this argument. However, if the thickness and modulus of elasticity of the film layer are of the same order of magnitude as the corresponding component material parameters then the strain distribution on the non-uniform film layer will be significantly altered. In that case, cutting the film would no longer be permissible and the non-uniform distribution would have to be accomplished by spatially varying the electrode plating.

Because the tip mass was small ($\frac{1}{2}$ gram),the magnetic actuator proved to be more effective in inducing flexural vibrations than in the uniform sensor analysis. However, a cantilever beam produces small linear tip displacements (but large angular displacements) at even modes. A linearly-varying distribution on a cantilever beam senses transverse tip displacement only (from Eq. (2-31)),

$$V_f(s) = -\frac{Q_0}{C}\left(\frac{w(1,s)}{L}\right). \qquad (4-4)$$

The accelerometer output, V_a, is giver by

$$V_a(s) = G_a s^2 w(1,s) \qquad (4-5)$$

Representing Eq. (4-4) in the frequency domain with the buffer circuitry included,

and combining the result with Eq. (4-5) gives the governing equation for this experimental analysis:

$$\frac{V_a}{V_f} = -\frac{G_a L}{Q_0}\left(\frac{R_b C_f s + 1}{R_b}\right) s \qquad (4-6)$$

The relevant parameters are found in Table 4-2. The structure was excited through a continuous sinusoidal sweep from 6 to 120 Hz for fifty averages. The first three modes were found to occur at 17.81 Hz, 67.5 Hz, and 115.3 Hz, respectively. Figure 4-5 shows the experimental results. Theoretical curves are drawn for $k_{31} = 12\%$ (dashed lines) and $k_{31} = 6\%$ (hash-marked lines). As is evident from the figure, there is no coherence for a band of frequencies in the vicinity of the second mode. Even modes of a cantilever beam are characterized by large angular tip displacements but minimal transverse tip displacements and accelerations. Because there is little translational tip motion at these frequencies, neither the film sensor nor the accelerometer adequately senses its respective parameter.

The frequency bandwidth of both experimental analyses presented thus far has been limited due to the poor ability of the discrete sensors to observe motion at certain frequencies because of their location on the structure, and similarly the inability of the magnetic actuator to provide sufficient excitation throughout the entire analysis range. In the next section, linearly-varying PVF_2 sensors *and* actuators are incorporated in the same structure, producing results which verify the sensor governing equation (Eq. (2-23)) for the first three modes.

4.3 Radiative Cross-coupling Between PVF_2 Sensors and Actuators

In this section the radiative cross-coupling phenomenon, an effect which occurs when structual elements contain both sensor and actuator film distributions, is investigated. The sensor governing equation (Eq. (2-23)) was tested for a linearly-varying distribution (Eq. (2-27)) on a cantilever beam using the identical experimental configuration and procedure described in section 4.2. However, rather than a magnetic coil a linearly-varying film distribution was used as the actuation element. A signal source generated a continuous sinusoidal sweep from 7 to 120 Hz. The source output was then amplified and a 200 Volt RMS signal was applied across the actuator

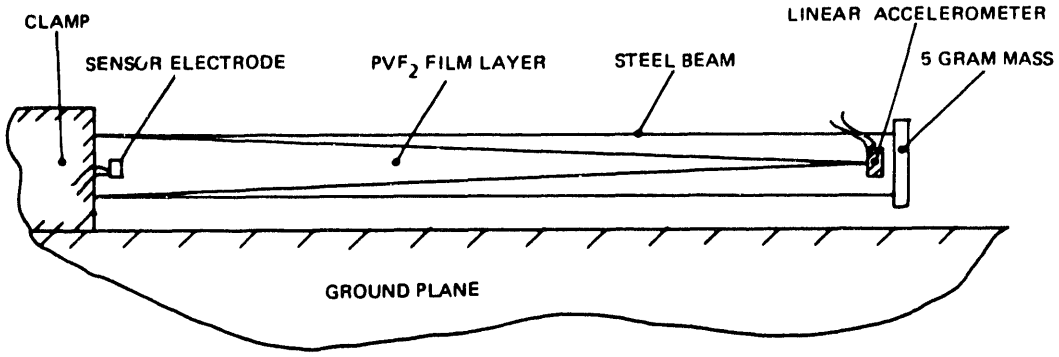

Figure 4-4. Linearly-varying sensor applied to a cantilever beam, side view.

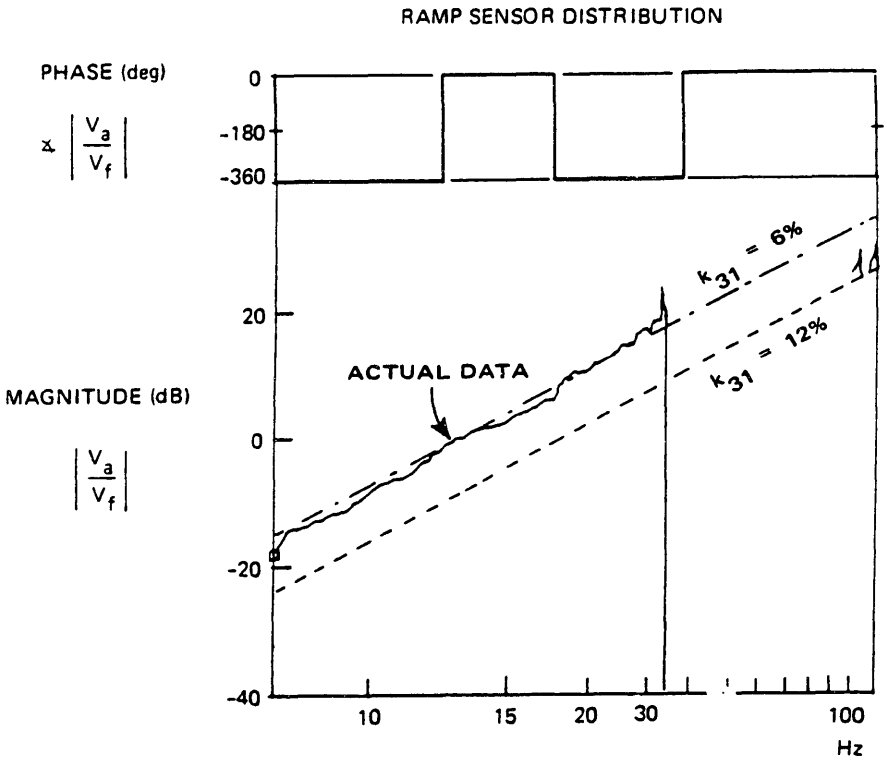

Figure 4-5. Linearly-varying sensor distribution results.

parameter	*Beam*	PVF_2	*Other*
Modulus, E, $N \cdot m^2$	$210x10^9$	$2.0x10^9$	
Length, L, m	0.140	0.140	
Thickness, h, mm	$h_b = .508$	$h_f = .028$	
Width, b_0, mm	12.7	12.7	
Density, ρ, kgm^{-3}	7800	1800	
Film Capacitance, C_f, nF		2.08	
Film Resistance, MΩ		> 7000	
g_{31}, $\frac{m^2}{Coul}$		$\cong 216x10^{-3}$	
Coupling Factor, k_{31}		$\cong 12\%$	
Buffer Resistance, R_b			80 MΩ
Accelerometer Gain, G_a			37.1 mV/$\frac{m}{sec^2}$
Dist. from n. axis, D, μm			254
Q_0, Coulombs			$2.15x10^{-7}$

Table 4-2. Linearly-varying Sensor Analysis Parameters

film, inducing a strain in the film and thereby exciting the structure. A $\frac{1}{2}$ gram linear accelerometer was mounted near the free boundary, the accelerometer and film sensor outputs were measured using the Zonic 6800 spectrum analyzer, and the data was compared to the theoretical result (Eq. (4-6)). All relevant parameters are included in Table 4-2.

The results of the experimental procedure are given in Figure 4-6. Theoretical curves for $k_{31} = 12\%$ and for $k_{31} = 6\%$ are indicated on the figure as dashed lines and hash marks, respectively. The figure shows that the implementation of both sensor and actuator spatial film distributions on the same composite structure results in a radiative "cross-coupling" effect, in which large excitation signals on the actuator film propagate onto the sensor film. If a 200 V RMS square wave is applied across the actuator film, a square wave signal is observed on the sensor film. At off-modal frequencies the sensor film produces small structurally-induced voltages which are dominated by cross-coupled noise. At frequencies which are characterized by large tip displacements (near the first and third structural modes), the structurally-induced component of the sensor film signal is significantly greater than the radiative noise component. In Fig 4-6 the data follows the theoretical curve

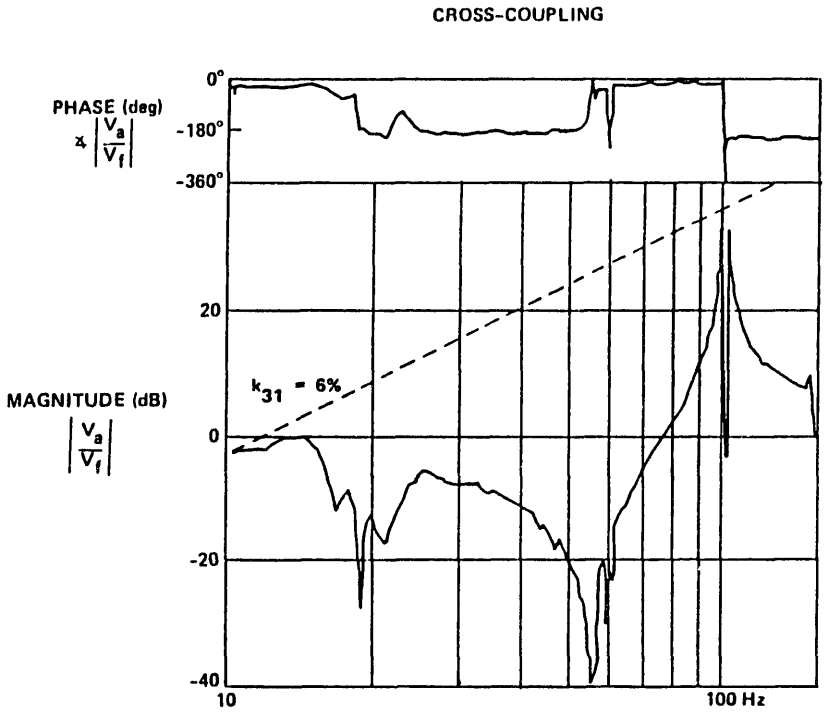

Figure 4-6. Experimental results for linearly-varying sensor experiment using PVF_2 as an actuator. Results indicate a radiative cross-coupling phenomenon between sensor and actuator film layers.

in the vicinity of the first and third modes (11.25 Hz and 94.22 Hz, respectively). At off-modal frequencies and at frequencies near the second mode ($\approx$ 55 Hz) the radiative noise is high, resulting in poor coherence and unreliable data. If the radiative noise dominates the sensor output, then a large phase shift is observed.

An effective way to reduce the cross-coupling phenomenon is through the implementation of a simple decoupling circuit. The decoupling circuit shown in Fig. 4-7 was incorporated into the experimental configuration as indicated in Fig. 4-8. The experimental results are shown in Fig.'s 4-9 and 4-10. Fig. 4-10 shows that at 51.6 Hz the tip displacement is minimal, the accelerometer signal is reduced dramatically, and the distributed (displacement) film sensor signal falls into the noise floor. The analog circuitry is unable to reject the radiative noise caused by the large actuator signal when the signal-to-noise ratio falls below -75 dB. At 66.5 Hz, significant tip

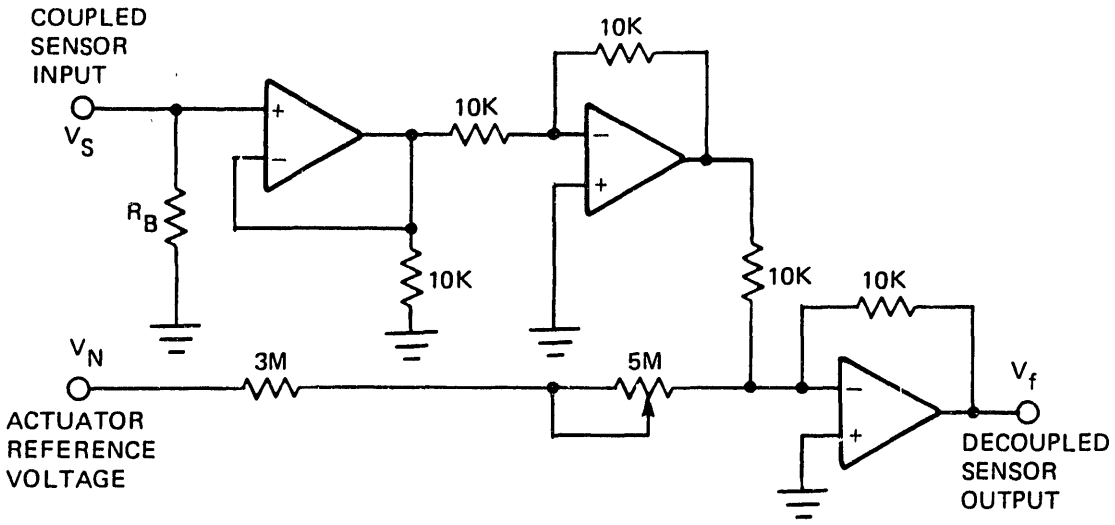

Figure 4-7. Differential circuit to reduce cross-coupling effect.

motion allows the film sensor to function effectively, but at higher frequencies small tip displacements again lead to coupling between the sensor signal and the actuator film input.

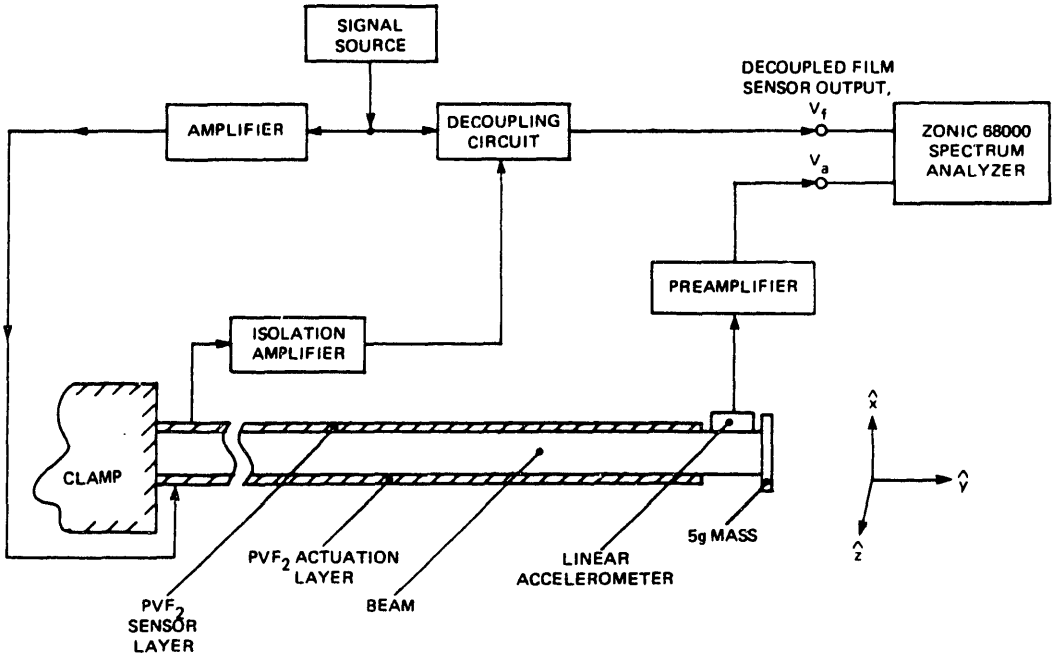

Figure 4-8. Experimental configuration with cross-coupling rejection circuit included.

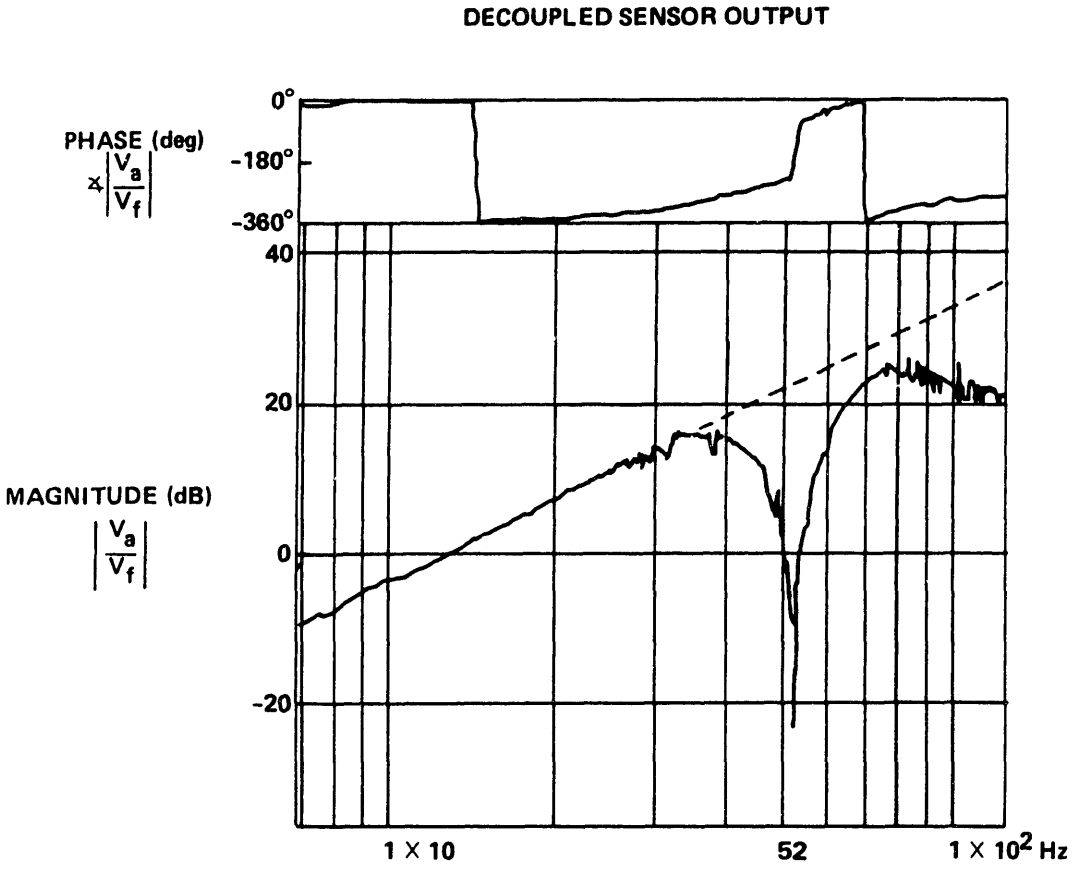

Figure 4-9. Experimental results with rejection circuitry included.

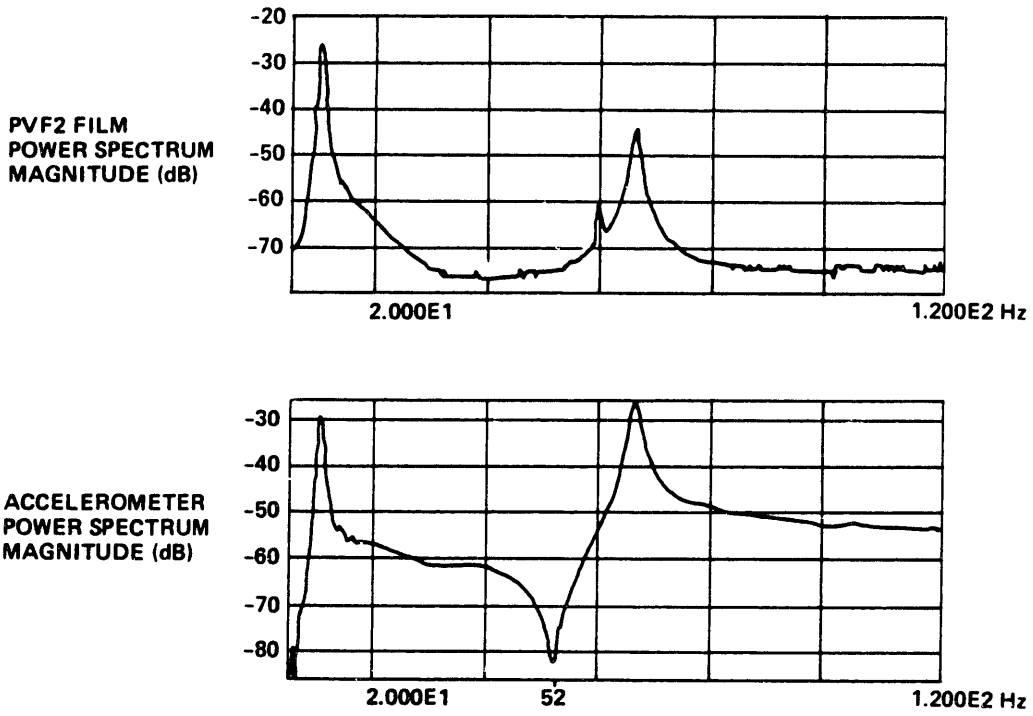

Figure 4-10. Frequency spectrum data for the PVF_2 linearly-varying displacement sensor (top) and accelerometer (bottom).

Chapter 5

Experimental Verification of Control Methodologies

5.1 Experimental Verification of *Smart* Component Control Law

In this section the smart component control law (Eq. (2-24)) is experimentally validated. Uniformly distributed sensor and actuator film layers are applied to a cantilever beam, resulting in a beam/film composite structure which contains all of the fundamental elements of an active vibration control system. The control law and set of geometric constraints presented in section 2.3 are enforced for the structure and controllability is demonstrated for the first two vibrational modes.

Fig. 5-1 shows the configuration of the experimental procedure. The stainless steel beam with uniform PVF_2 transducers epoxied to each surface was excited with an Electro 3030S20 magnetic coil. An Entran EGA-125 linear accelerometer was mounted at the tip of the structure for the first mode analysis, and near the midspan of the structure for second mode testing. A Zonic 6800 spectral analyzer was used to measure the transfer function between acceleration and beam excitation. A 5 gram tip mass was incorporated into the test structure. For the first mode analysis the accelerometer was mounted near the tip of the beam, and for second mode testing the accelerometer was fixed to a point along the midspan of the structure. All pertinent experimental parameters are contained in Table 4-2.

The first modal frequency of the test structure was approximately 5 Hz. The structure was excited by a swept sine from 3.75 to 6.0 Hz using a sweep rate of 0.05 $\frac{Hz}{sec}$. The sweep rate and narrow band analysis range was chosen so that several sweeps would occur within the discrete time averaging interval, to insure reliable and repeatable results. A voltage proportional to the time derivative of the sensor

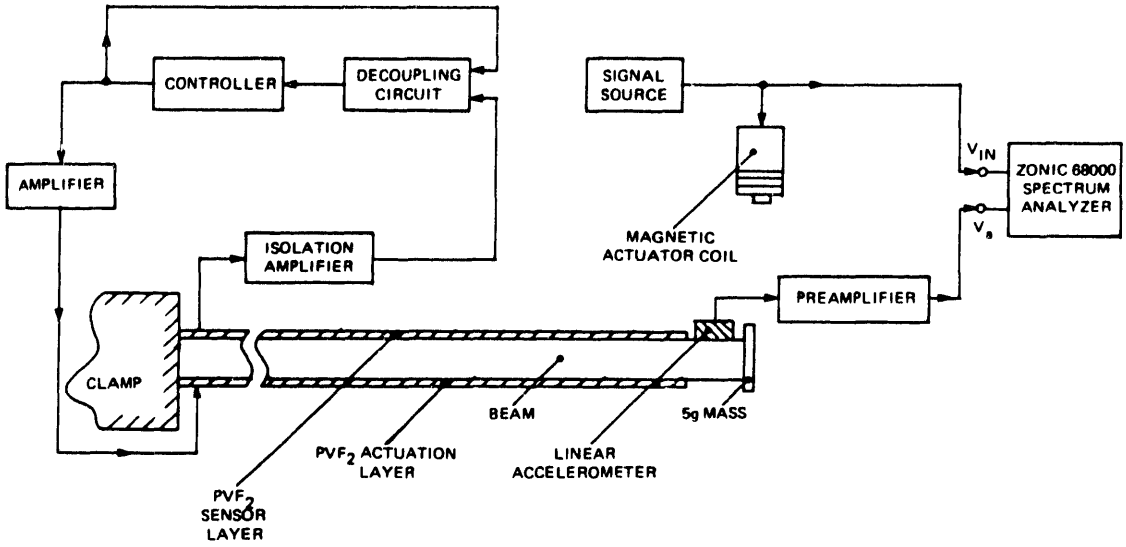

Figure 5-1. Experimental configuration for control analysis.

signal was applied across the actuator film to provide active damping. The actuator film in this configuration develops a uniform bending moment within the structure, as discussed by Bailey and Burke [6,8]. The experimental configuration allows the transfer function between acceleration and actuator excitation to be measured independent of the active damper elements. The damping coefficient, ζ, was calculated from Eq. (5-1) [19,20] where ω_a and ω_b are the peak frequencies in the real part of the transfer function:

$$\zeta = \frac{1}{2}\left[\frac{\left(\frac{\omega_b}{\omega_a}\right)^2 - 1}{\left(\frac{\omega_b}{\omega_a}\right)^2 + 1}\right] \qquad \omega_a < \omega_b \qquad (5-1)$$

Fig. 5-2 shows the magnitude of the transfer function between tip acceleration and input excitation from the magnetic actuator for the first mode. In the figure, the solid line represents the transfer function as a function of frequency for the uncontrolled case, and the dotted line represents the frequency response of the actively controlled beam. The maximum voltage applied across the actuator film was 350 V peak-to-peak for the first mode. Fig. 5-3 shows the results for the second vibrational mode, which occurs at $\approx$ 48 Hz. For second mode analysis, the test structure was excited through a continuous sinusoidal sweep from 46 to 52 Hz at

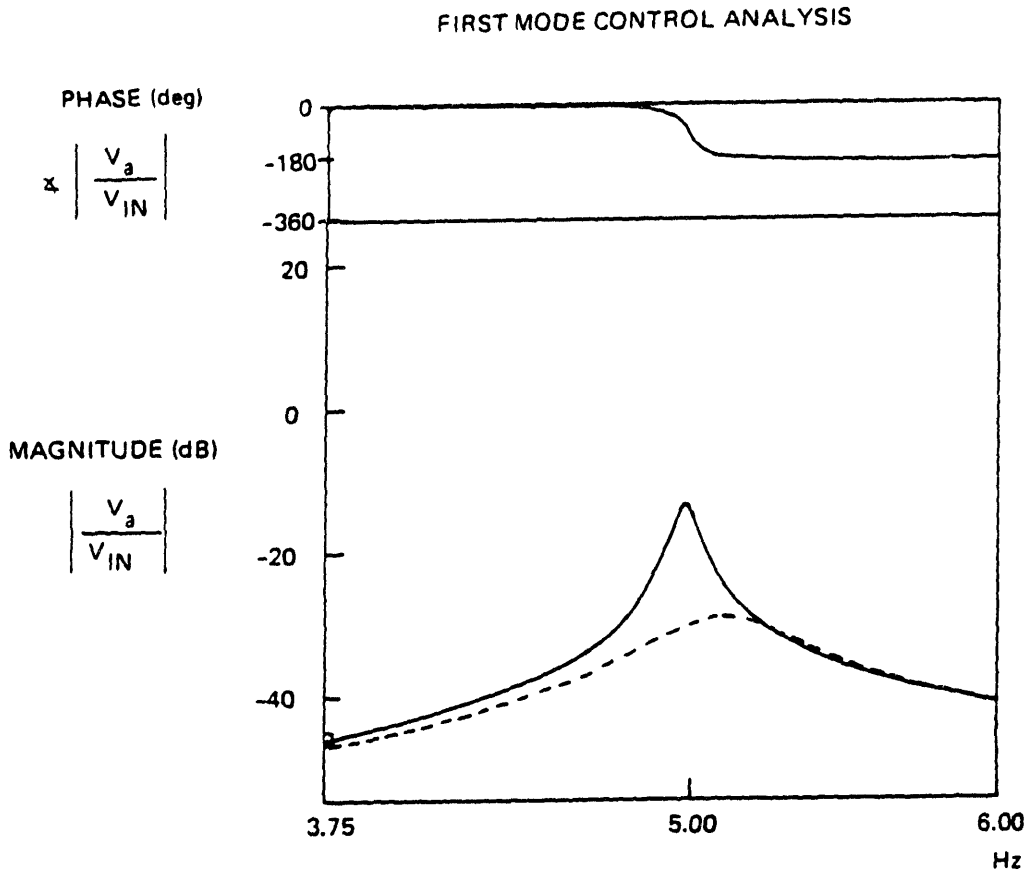

Figure 5-2. Transfer function between acceleration and actuator signal for the first mode. Solid line is the uncontrolled response, dashed line is the actively damped response.

a rate of .05 Hz/sec. Because differentiation is an inherently noisy process, it was not possible to apply a feedback voltage greater than 184 V peak-to-peak across the actuator film for second mode control, because noise in the feedback signal would drive the system unstable. In both figures it is seen that the damped natural frequency is higher than the undamped resonant frequency, which is most likely the result of a phase error in the bandpass filter. The control algorithm requires a $-90°$ phase shift between the film sensor output and the feedback signal to the actuator: in the actual experiment the phase shifts for the first and second modes were $-99.2°$ and $-100.8°$, respectively.

The numerical results for both the first and second modes are tabulated in Ta-

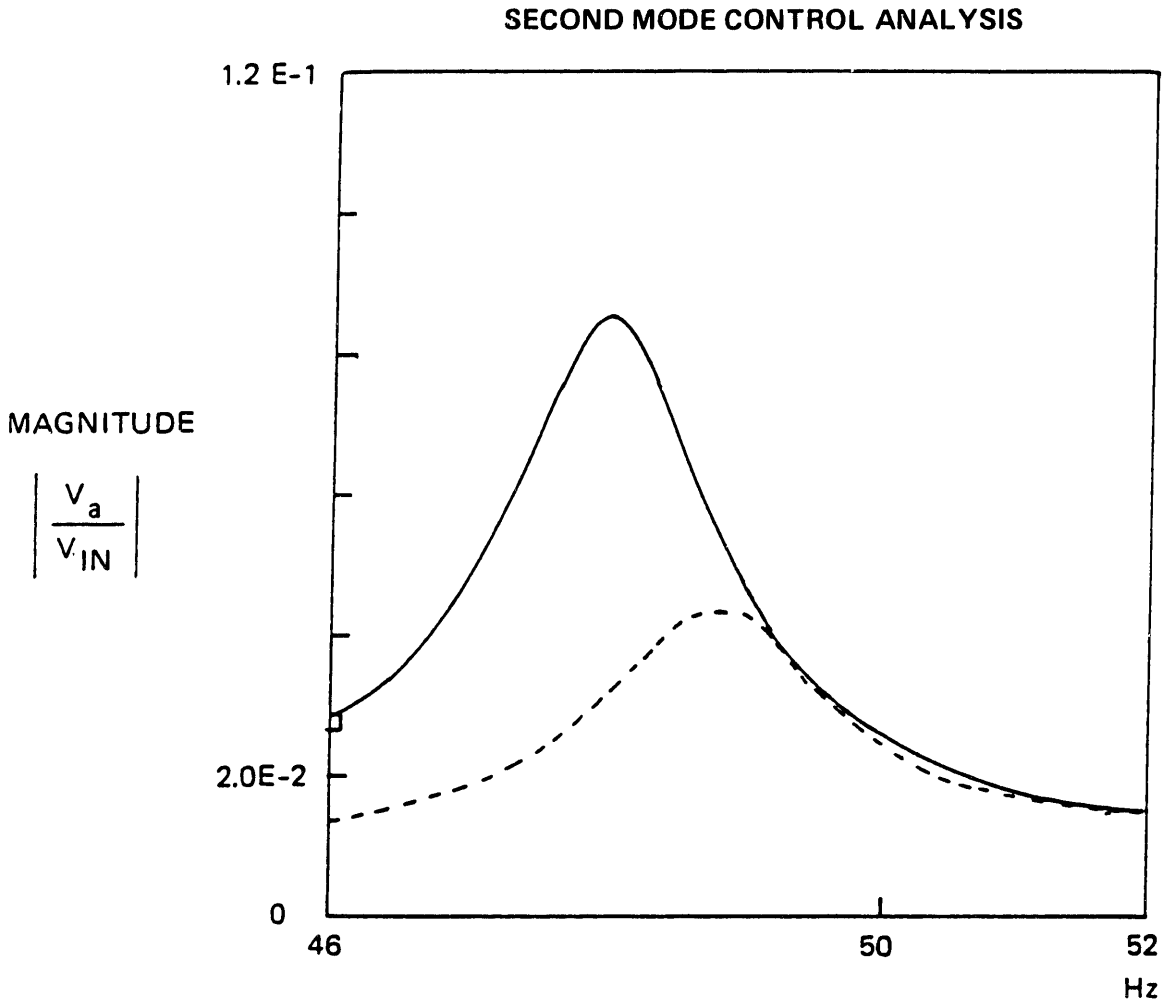

Figure 5-3. Transfer function between acceleration and actuator signal for the second mode. Solid line is the uncontrolled response, dashed line is the actively damped response. The y-axis is linearly scaled.

parameter	*First Mode*		*Second Mode*	
	uncontrolled	**controlled**	**uncontrolled**	**controlled**
ω_a	4.94 Hz	4.98 Hz	47.20 Hz	47.22 Hz
ω_b	5.01 Hz	5.395 Hz	48.53 Hz	49.824 Hz
ζ	0.0069	0.0399	0.0139	0.0268
feedback	350 V		184 V	
d. factor, R	5.728		1.928	

Table 5-1. Experimental Results for Component Control Analysis

ble 5-1. The damping factor, R, indicates the ratio between the controlled and uncontrolled damping coefficients. The results indicate that PVF_2 sensors and actuators may be integrated into a lightly damped beam component to provide active structural damping. However, the results show that the radiative cross-coupling phenomenon hampers the effectiveness of the PVF_2 sensor-actuator damper. The radiative cross-coupling effect produces noise on the sensor film, and differentiating the sensor signal to provide the control parameter augments the noise problem. In practical application, it may be advantageous to use multiplexing techniques between the sensor and actuator rather than to implement differential amplifier circuitry. The quality of the noise reduction techniques will generally dictate the effectiveness of the controller.

5.2 Experimental Verification of Smart Structures Concept

In this section the generalized smart structure control law (Eq. (3-40)) is validated through the experimental analysis of the "Y-structure" shown in Fig. 3-7. The structure is constructed from three beam members, each of which has uniform layers of uniaxially polarized PVF_2 film epoxied to both faces. Parameters for each beam member are nearly identical and are provided in Table 5-2. Tip masses (4 grams) are fixed to the free ends of the structure as shown in the figure. The base beam is rigidly clamped to a ground fixture. Each film layer is 28μm in thickness and is adhered to a component surface using Eccobond 45LV, a low viscosity epoxy. The average thickness of the epoxy layers was measured and found to be $\approx 9\mu$m. Every PVF_2 layer is oriented such that each positively biased film surface is an outer

surface. The beam layers are steel and 0.015 inches (0.381μm) in thickness. Based on the experimental results presented in section 4.3, the steel layers are used as a ground plane to reduce cross-coupling between the actuator and sensor film layers. Electrodes constructed by soldering lead wires to thin copper tabs are adhered to the electroplated, positively-biased outer film surfaces with conductive epoxy. Stranded 40 gage lead wires are used because they are extremely compliant and therefore preserve the lightly damped character of the passive system.

The three smart beam components are rigidly attached at a common boundary as shown in Fig. 5-4. The two outer beams are each bent at 45 degree angles and spot welded onto the base beam. An isosceles shaped plexiglass wedge, one inch thick along the hypotenuse, is inserted between the two outer beams as shown. The wedge is adhered to the two outboard members with Permabond 910, a cyanoacrylate adhesive. The plexiglass wedge serves to enforce a zero slope boundary condition for the outer beams and to provide additional rigidity to the joint without significantly increasing the mass of the structure.

A schematic of the experimental setup is shown in Fig. 5-5. An Electro 3030S20 magnetic coil was used to drive the system. As indicated in the figure, each smart beam component is independently controlled according to the control law given in Eq. (3-40). Based on the previous experimental results found in section 4.3, the film sensor output was passed through a buffer and a decoupling circuit in order to reduce cross-coupling noise between sensor and actuator transducers on the same beam member. A bandpass filter was used as the the controller in order to differentiate the sensor signal across a bandwidth spanning the first four modes. The first four modes all occur at frequencies less than 40 Hz. A bandpass filter with the following transfer function was chosen:

$$\frac{V_{out}}{V_{in}} = 100\frac{s}{(s+3000)^2} \qquad (5-2)$$

The buffer, differential decoupling, and bandpass filter electronics are shown in Fig. 5-6.

Frequency response data corresponding to the second, third, and fourth structural modes were obtained by exciting the structure through a sinusoidal sweep in a narrow bandwidth of frequencies in the vicinity of each mode, and then measuring

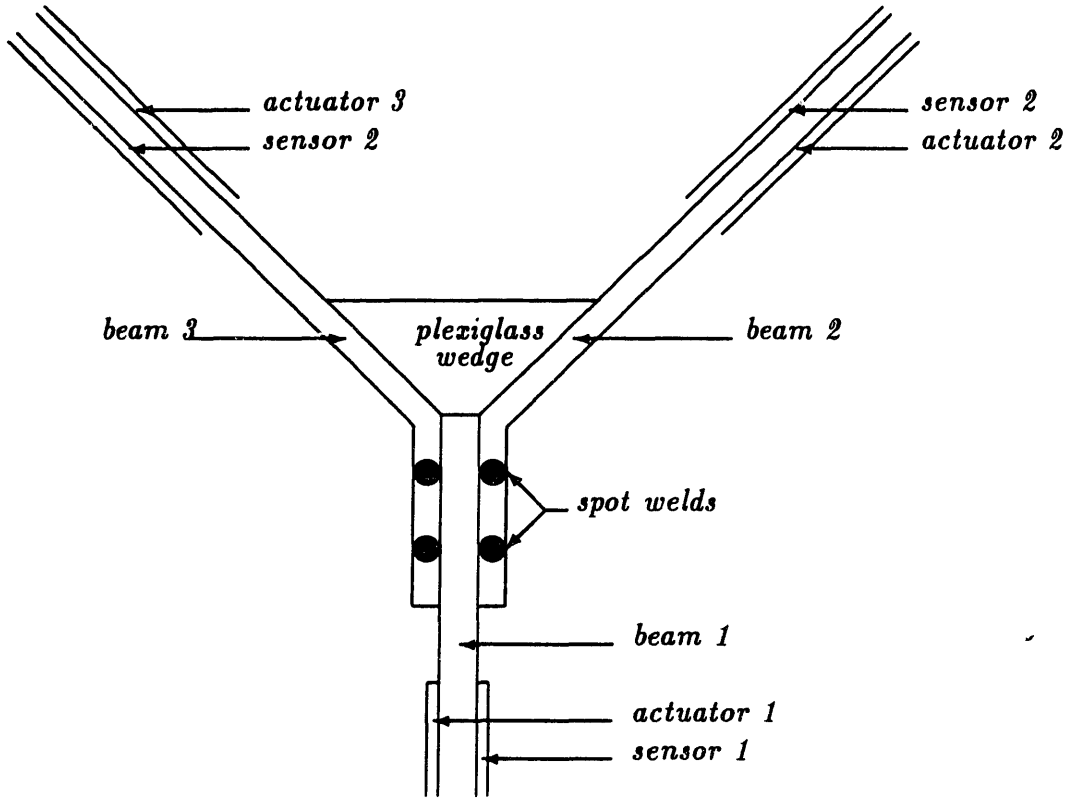

Figure 5-4. Geometry of the common boundary where the three smart components are joined. Beams 2 and 3 are spot-welded to beam 1. All three members are epoxied to the plexiglass wedge.

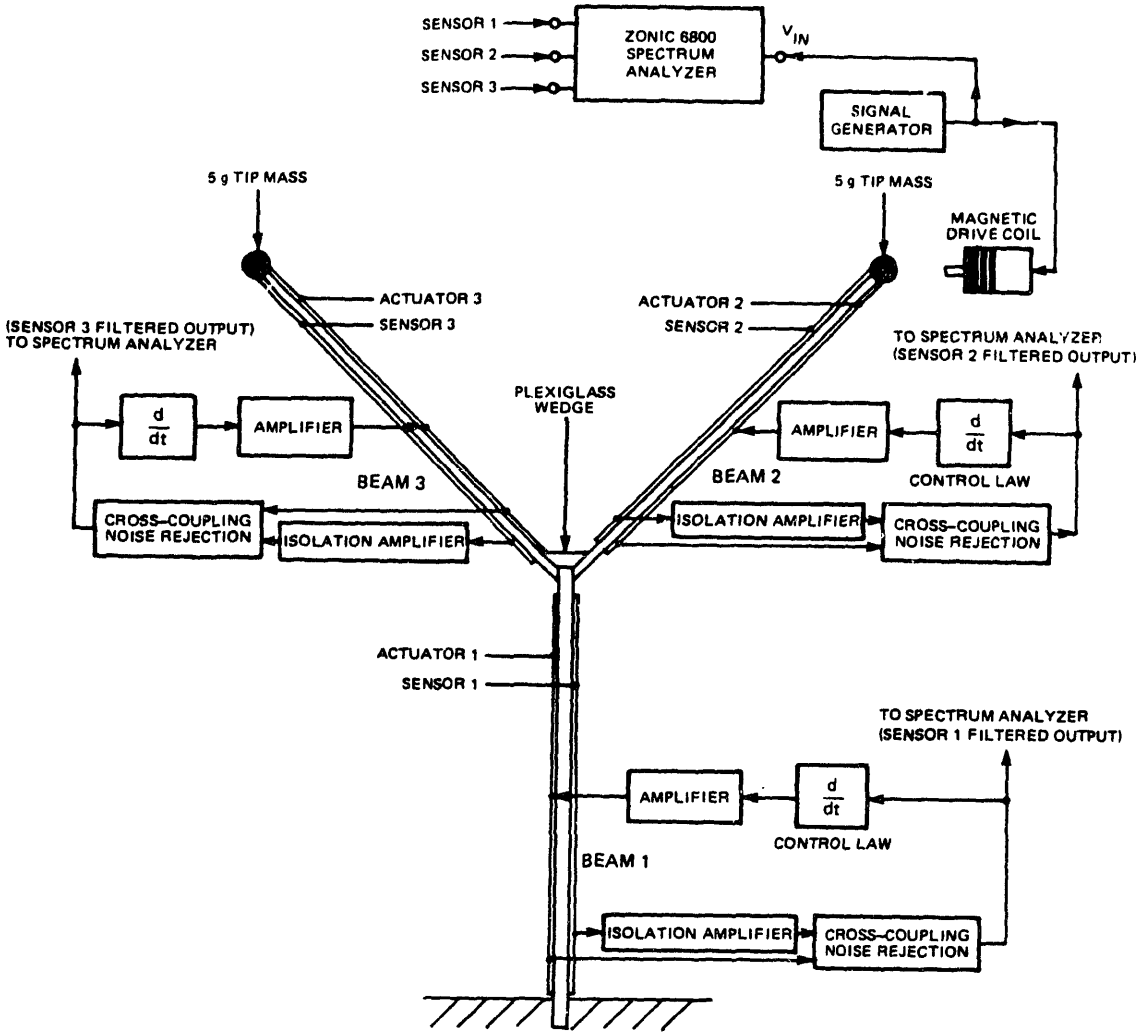

Figure 5-5. Experimental setup for the Y-structure control experiment.

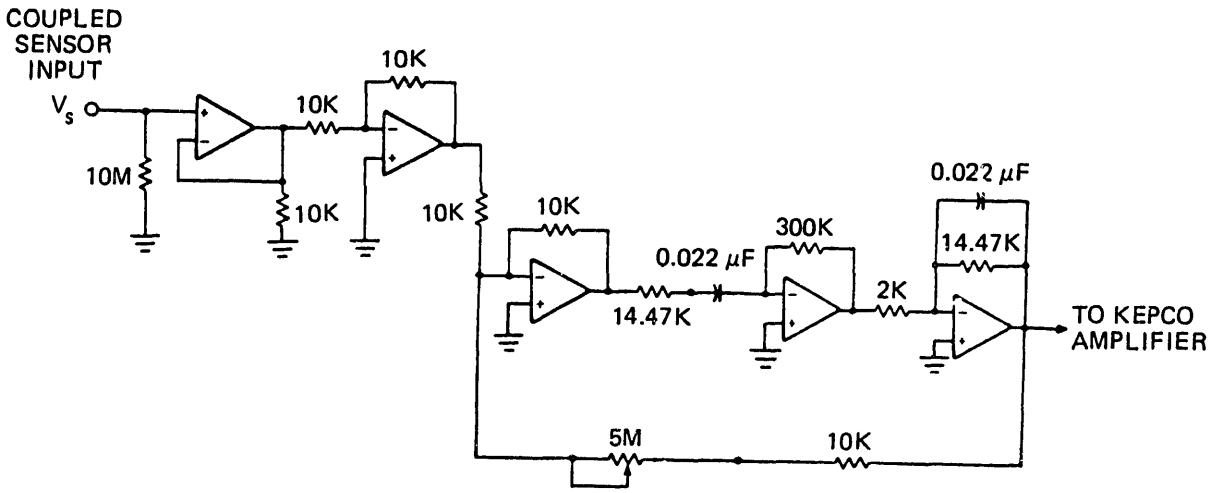

Figure 5-6. Analog compensation circuit used to implement the control law for each smart component.

the transfer function between a selected film sensor output and the noise input to the coil. The sweep rate for each test was carefully selected in order to insure that several sweeps would be generated for every sampling period while maintaining a sweep that would be slow enough to guarantee repeatable results. The magnetic actuator signal was limited to insure small motions. The frequency response data were measured for both the open and closed loop system using a Zonic 6800 modal analyzer. To obtain damping coefficients the Zonic modal capability was used: the Zonic analyzer determines the coefficients by characterizing each mode as a spring-mass subsystem with a linear viscous damper element.

It was not possible to obtain reliable frequency response data for the first mode for two reasons: the signal generator was not capable of initializing the sweep at a sufficiently low frequency (< 1Hz), and the generator could not perform a sweep at a rate slow enough to insure accurate results. The damping coefficients for this mode were therefore obtained through a transient response analysis. The modeshape of the first bending mode is shown in Fig. 5-7. The modeshape was determined using the NASTRAN finite element program (section 6.1). The resonant frequency of the first mode of the (undamped) system was found to be 1.380 Hz. The structure was excited at this frequency with the drive coil until a steady state was reached. The signal to the drive coil was then turned off and the uncontrolled structure was allowed to free-decay. The output of the film sensor situated on the base beam was measured using the Zonic 6800 analyzer. The procedure was then repeated but the control loops for each smart component were closed. The open and closed loop transient response data is given in Fig. 5-8.

The damping coefficient, ζ, for both controlled and uncontrolled system response to excitation at the first mode was determined using the logarithmic decrement method (Ref. [21], pp. 126-128) and is included in Table 5-3. Because the passive damping for the first mode is high, the PVF_2 active layers are not able to increase the damping for this mode by a large amount. In the actively controlled case the feedback amplifier gains were adjusted to provide the maximum voltage to each actuator (400 V peak-to-peak is an upper bound). Since the relative motions in beams 2 and 3 were small, the maximum control signal inputs to actuators 2 and 3 were less than 75 V peak-to-peak (the gains could not be increased further

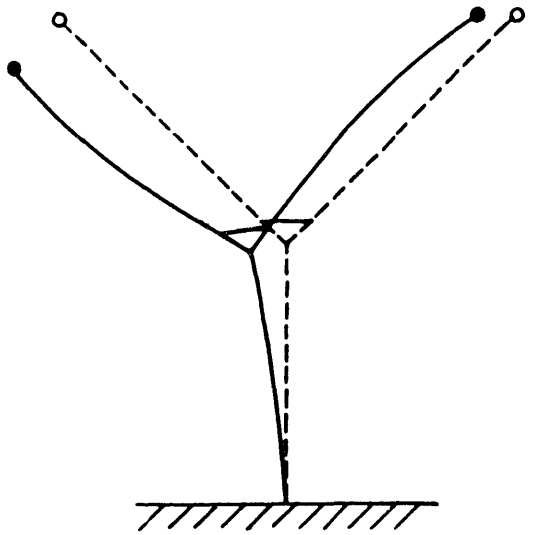

Figure 5-7. Modeshape for the first bending mode of the Y-structure.

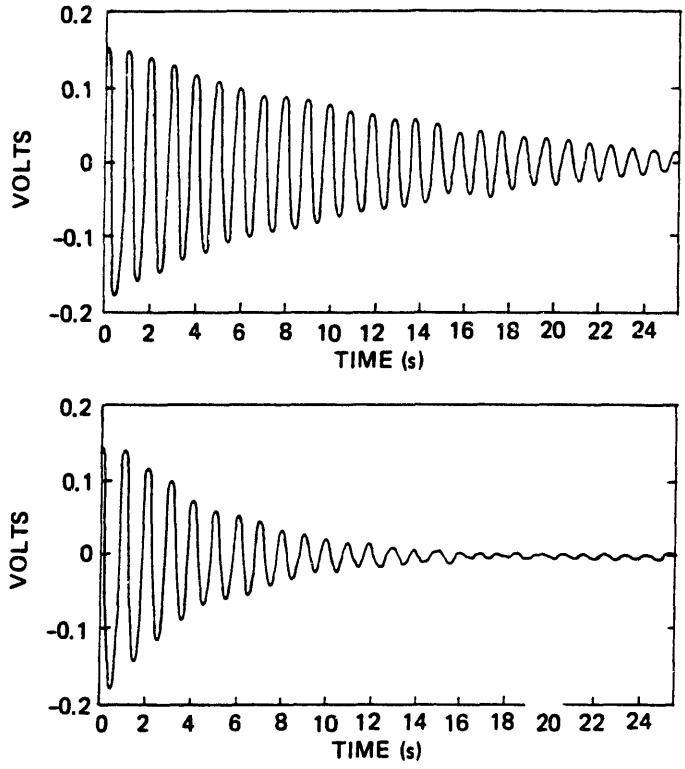

Figure 5-8. Transient response data for the first mode. Open loop response is at top, closed loop response is at bottom.

without saturating the op-amps). Performance was inhibited since most of the active damping was achieved through the active control of beam 1 alone.

The modeshape corresponding to the second bending mode is shown in Fig. 5-9, and was determined using a finite element model simulation (section 6.1). The resonant frequency of the second mode was found to be 7.60 Hz. The mode is characterized by large angular displacements at the free ends of beams 2 and 3. Beam 1 is not displaced. Frequency response data for this mode was obtained by exciting the structure with the magnetic coil through a sinusoidal sweep spanning a frequency range of 6.8 to 8.2 Hz. A sweep rate of .01 Hz/sec was chosen, allowing for nearly four sweeps to occur within one averaging period. The uncontrolled and controlled transfer functions between the beam 2 film sensor and the input signal to the magnetic driving coil are given in Fig. 5-10. The data was obtained over a sampling interval of 50 averages. The damping coefficients for the controlled and uncontrolled system are found in Table 5-3. The controller feedback gains were adjusted to provide 400 V peak-to-peak to the actuators on beams 2 and 3 at the resonant frequency. Since there is no relative motion in beam 1, adjusting the feedback gain in the control loop for beam 1 was ineffectual. The second mode is more lightly damped than the first mode, and thus the results shown in Fig. 5-10 clearly demonstrate the effectiveness of the smart structure control strategy. Damping is increased by a factor of 28.8 for this mode using the linearly-proportional rate feedback control law.

The modeshape corresponding to the third structural mode is shown in Fig. 5-11. The third mode was found to occur at 9.09 Hz. Because of the close proximity of the resonant frequency of the third mode to that of the second mode, frequency response data was accumulated for a frequency range spanning *both the second and third modes* to validate the assertion that the smart structure control strategy can simultaneously provide active damping to multiple modes of a structure. The magnetic coil was used to excite the structure through a sinusoidal sweep from 7 to 10 Hz. A linear sweep rate of 0.01 Hz/sec was again chosen. The controller gains were again set to provide a 400 V peak-to-peak signal to the actuators on beams 2 and 3 at the resonant frequency of second mode, and to provide a 400 V peak-to-peak signal to the actuator layer on beam 1 at the resonant frequency of the third

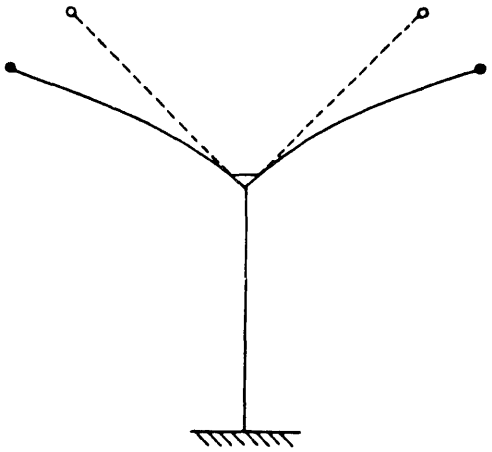

Figure 5-9. Modeshape for the second bending mode of the Y-structure.

mode. At the third mode resonant frequency the control signals into the beam 2 and beam 3 actuators were measured and found to be approximately 285 V peak-to-peak. It was not possible to increase the gains in the feedback loop for these two components without running the risk of damaging the film actuators due to excessive voltages. A transfer function between the sensor film on the second beam and the input signal to the magnetic actuator coil was obtained for the uncontrolled and controlled cases: the results are given Fig. 5-12. Data was accumulated over a sampling interval of 50 averages. The damping coefficients are given in Table 5-3. The results indicate that the smart component control strategy is effective in providing vibration control to both the second and third modes simultaneously.

The fourth structural mode was found to occur at 36.91 Hz. The modeshape for the fourth mode is given in Fig. 5-13. The drive coil was used to excite the structure from 35 to 40 Hz. A sweep rate of .05 Hz/sec was chosen. Transfer functions between the beam 2 film sensor and the excitation noise were obtained for the controlled and uncontrolled responses and are presented in Fig. 5-14. The results are included in Table 5-3.

In Fig.'s 5-10, 5-12, and 5-14 it is observed that the damped modal frequencies tend to exceed the undamped modal frequencies. The effect becomes more apparent

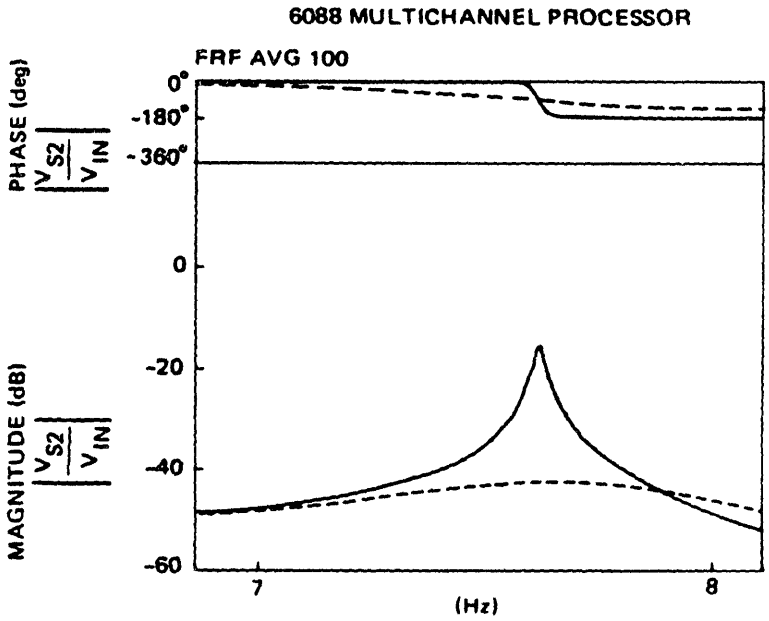

Figure 5-10. Transfer function between the film sensor on beam 2 and the signal input to the magnetic driving coil for the second mode. Solid line is the uncontrolled response, dashed line is the actively damped response.

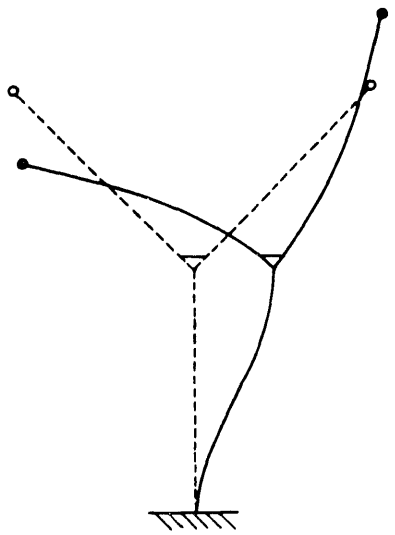

Figure 5-11. Modeshape for the third bending mode of the Y-structure.

as the modal frequencies increase. The phenomena occurs due to the fact that the phase of the bandpass filter (Eq. (5-2)), intially 90° at 0 Hz, tends to decrease with increasing frequency. The phase is nearly constant over the frequency range spanning the first three modes, although at the fourth mode the compensator phase has deviated by nearly 15°. The damped natural frequency of the fourth mode is therefore appreciably greater than the undamped natural frequency. The damped natural frequency of the fourth mode is seen to diminish as the center frequency of the bandpass filter is increased.

The experimental results indicate that the *smart* structures concept is most effective in controlling vibrations in structural modes characterized by low damping and high strain energy states. In this particular structure the strain energy state of the first mode is less than all other modes considered in the experimental analysis. In the first mode the base beam experiences some strain whereas the outboard beams (beams 2 and 3 in Fig. 3-7) remain nearly rigid. The outboard beams exhibit large strains at the second mode. The strain energy and structural damping of the second mode is significantly greater than all other modes, and implementation of the *smart* structure control law increased the damping coefficient for the second mode by a factor of 29. The damping coefficient of mode 3 was increased by a

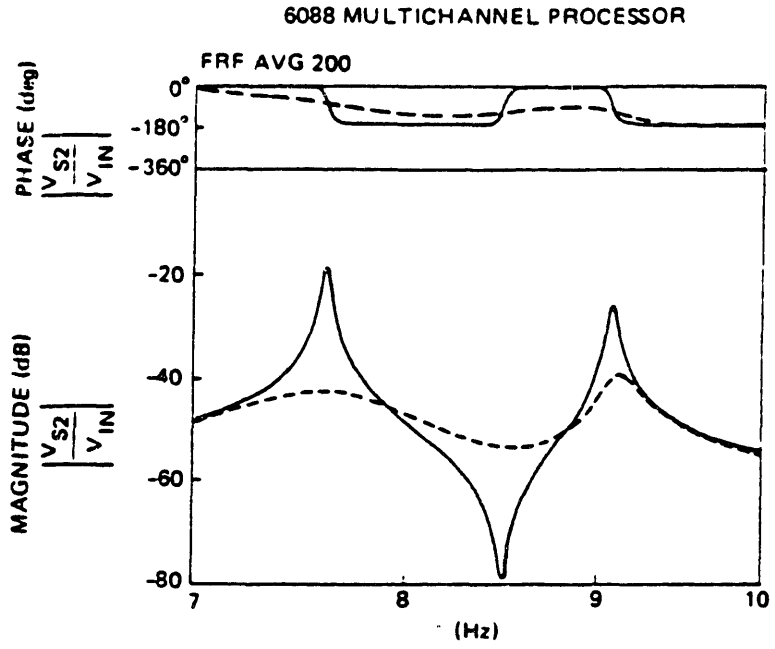

Figure 5-12. Transfer function between the film sensor on beam 2 and the signal input to the magnetic driving coil for the second and third modes. Solid line is the uncontrolled response, dashed line is the actively damped response.

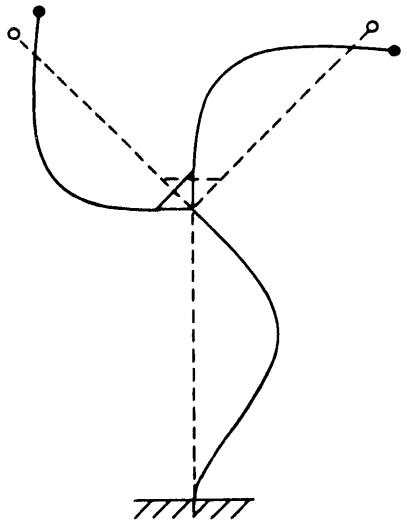

Figure 5-13. Modeshape for the fourth bending mode of the Y-structure.

factor of 7.3. Damping for the first and fourth modes were improved by factors of 2 and 5, respectively. The results verify that the *smart* structures concept is effective in providing vibration control to lightly damped multi-component structures.

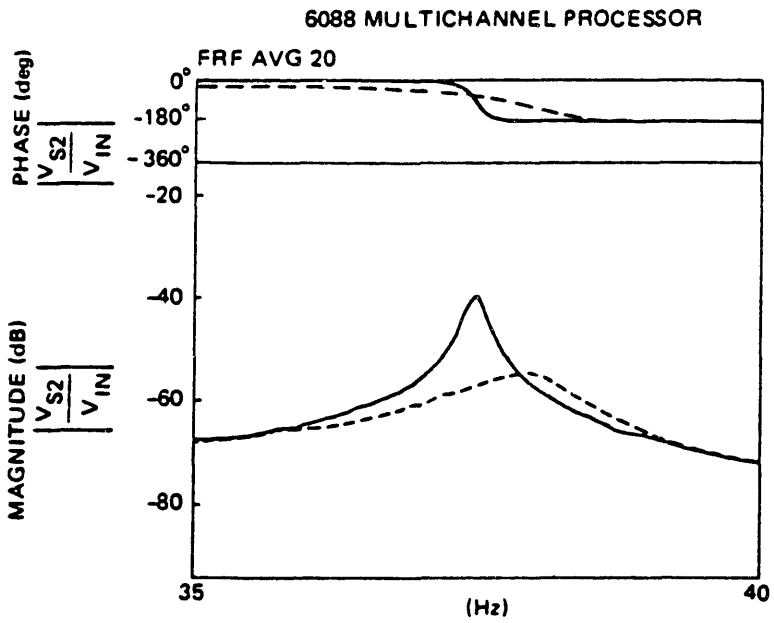

Figure 5-14. Transfer function between the film sensor on beam 2 and the signal input to the magnetic driving coil for the fourth mode. Solid line is the uncontrolled response, dashed line is the actively damped response.

parameter	*Beam*	PVF_2
Modulus, E, $N \cdot m^{-2}$	$210x10^9$	$2.0x10^9$
Length, L, m	0.140	0.140
Thickness, h, mm	$h_b = .381$	$h_f = .028$
Width, b_0, mm	12.7	12.7
Density, ρ, kgm^{-3}	7800	1800
Film Capacitance, C_f, nF		5.03
Film Resistance, MΩ		> 7000
g_{31}, $\frac{m^2}{Coul}$		$\cong 216x10^{-3}$
d_{31}, $\frac{m}{Volt}$		$\cong 23x10^{-12}$
Coupling Factor, k_{31}		$\cong 12\%$
Q_0, Coulombs		$1.61x10^{-7}$

Table 5-2. Structural parameters for smart components used in the control experiment.

parameter	*First Mode*	*Second Mode*	*Third Mode*	*Fourth Mode*
ω_n	1.380 Hz	7.600 Hz	9.092 Hz	36.91 Hz
ζ (uncontroiled)	0.01220	0.00146	0.00230	0.00181
ζ (controlled)	0.03435	0.04234	0.01667	0.00869
V_{max}, act. 1	±200V	0 V	±200V	±200V
V_{max}, act. 2	±38V	±200V	±142V	±172V
V_{max}, act. 3	±38V	±200V	±142V	±172V

Table 5-3. *Smart* Structure Control Analysis Results.

Chapter 6

Computer Simulation of *Smart* Structures Experiment

6.1 Finite Element Model

The smart structure control experiment described in section 5.2 was simulated digitally. The simulation was accomplished using the MSC-NASTRAN finite element program in conjunction with CTRL-C, which is a computer-aided workbench for control system design and analysis developed by Systems Control Technology, Inc. In this chapter the digital model is described with the intent of outlining a viable method for generating computer simulations of *smart* structures.

In developing the NASTRAN finite element model for the "Y-Structure", it was assumed that each of the three component beams had material properties given in Table 5-2. However the material effects of the PVF_2 and epoxy layers were not included in the finite element analysis since their stiffness and mass properties are negligible relative to the steel inner layer. The three components were defined such that beam 1 is the beam length which extends from the clamped base to the plexiglass wedge (190 cm), while beams 2 and 3 extend from the hypotenuse of the wedge to the tip masses (refer to Fig.'s 3-7 and 5-4). Each beam component was subdivided into eleven elements. The common boundary joining the three beam components, shown in Fig. 5-4, was modeled as follows: the beam segments adjacent to the plexiglass wedge were modeled as rigid and massless regions 1.4 cm in length; the regions of beams 2 and 3 directly adjacent to beam 1 (and spot welded to beam 1) were modeled as two separate beam elements (1.9 cm long) which are rigidly fastened to beam 1 at their end points only. The mass properties of these two elements are found in Table 5-2. The tip masses were measured and found to be 4

grams. The case control and bulk data deck entries for the NASTRAN simulation are included in Appendix A.

The fundamental frequencies and modeshapes of the first ten modes were determined using NASTRAN. The modeshapes of the first four modes are illustrated respectively in Fig.'s 5-7, 5-9, 5-11, and 5-13 (see Sect. 5.2). The modal frequencies are presented and compared to the experimentally obtained values in Table 6-1. The first mode frequency estimate from the finite element program is somewhat higher than the experimental result, possibly due to the damping effect of the electrode wires which were necessarily connected to the PVF_2 layers. The correlation of the NASTRAN simulation to the experimental results validates the simplifying assumptions made in the finite element model. A complete listing of NASTRAN results is found in Appendix A.

6.2 Simulation of the Control Law Using CTRL-C

The *smart* structure control strategy was simulated digitally with the aid of the CTRL-C control analysis package. Only the first four modes were considered in the simulation. To emulate the film actuators and sensors, a discrete, co-located sensor and actuator pair was incorporated into the model at each of the five locations indicated in Fig. 6-1. Each sensor measures angular displacement and each actuator induces torque. Since uniformly distributed PVF_2 sensors measure the difference between angular displacement at the film boundaries (Eq. (2-28)), the three film sensors were simulated by determining the difference between the appropriate point sensors included in the model. Uniformly distributed actuators produce moments that act in equal and opposite directions at the film layer boundaries (Eq. (2-39)). The sensor and actuator pairs were coupled with the NASTRAN results for the first four modes to arrive at the following state-space representation for the system:

$$\frac{d}{dt}\begin{bmatrix}\vec{x}\\ \dot{\vec{x}}\end{bmatrix} = \begin{bmatrix}0 & I\\ -\omega_n & -2\zeta\omega_n\end{bmatrix}\begin{bmatrix}\vec{x}\\ \dot{\vec{x}}\end{bmatrix} + [B]\,\vec{u} \qquad (6\text{-}1)$$

$$\vec{y} = [C]\begin{bmatrix}\vec{x}\\ \dot{\vec{x}}\end{bmatrix} \qquad (6\text{-}2)$$

or

$$\frac{d\vec{x}}{dt} = A\vec{x} + B\vec{u} \quad (6\text{-}3)$$

$$\vec{y} = C\vec{x} \quad (6\text{-}4)$$

where $\vec{x}$ and $\dot{\vec{x}}$ are the modal displacement and velocity vectors, respectively, of the first four modes; ω_n is a diagonal matrix whose elements correspond to the modal natural frequencies; $-2\zeta\omega_n$ is a diagonal matrix whose elements are the modal damping coefficients; [B] is the actuator gain matrix; [C] is the sensor gain matrix; $\vec{u}$ is a vector whose five elements are the actuator inputs; $\vec{y}$ is an eight element vector whose first five elements are the discrete sensor outputs, and whose final three elements are the film sensor outputs (determined from the appropriate linear combinations of the discrete sensor outputs). The film sensor gains were determined from the experimental parameters given in Table 5-2: a value of $32\frac{V}{rad}$ was used for each sensor. The actuator gains were determined from "m" in Eq. (2-10), returning a value of $1.11 \cdot 10^{-7}\frac{N \cdot m}{V}$. The damping coefficients were extracted from the (uncontrolled) results found in Table 5-3.

In the experimental procedure described in Section 5.2, each film sensor was compensated according to the transfer function given in Eq. (5-2), amplified by a factor of 100, and fed back into the actuator located on the same structural component. The three component control laws may be represented in state space form:

$$\frac{d\vec{w}}{dt} = F\vec{w} + G\vec{y} \quad (6\text{-}5)$$

$$\vec{u} = H\vec{w} + \vec{u_o} \quad (6\text{-}6)$$

where

$$F = \begin{bmatrix} -6000 & -9 \cdot 10^6 & 0 & 0 & 0 & 0 \\ 1 & 0 & 0 & 0 & 0 & 0 \\ 0 & 0 & -6000 & -9 \cdot 10^6 & 0 & 0 \\ 0 & 0 & 1 & 0 & 0 & 0 \\ 0 & 0 & 0 & 0 & -6000 & -9 \cdot 10^6 \\ 0 & 0 & 0 & 0 & 1 & 0 \end{bmatrix} \quad (6\text{-}7)$$

$$G = \begin{bmatrix} 0 & 0 & 0 & 0 & 0 & 1 & 0 & 0 \\ \vdots & \vdots & \vdots & \vdots & \vdots & 0 & 0 & 0 \\ \vdots & \vdots & \vdots & \vdots & \vdots & 0 & 1 & 0 \\ \vdots & \vdots & \vdots & \vdots & \vdots & 0 & 0 & 0 \\ \vdots & \vdots & \vdots & \vdots & \vdots & 0 & 0 & 1 \\ \vdots & \vdots & \vdots & \vdots & \vdots & 0 & 0 & 0 \end{bmatrix} \tag{6-8}$$

$$H = \begin{bmatrix} -10^4 & 0 & 0 & 0 & 0 & 0 \\ 10^4 & \vdots & \vdots & \vdots & \vdots & \vdots \\ 0 & \vdots & -10^4 & \vdots & \vdots & \vdots \\ \vdots & \vdots & 10^4 & \vdots & \vdots & \vdots \\ \vdots & \vdots & 0 & \vdots & -10^4 & \vdots \\ \vdots & \vdots & \vdots & \vdots & 10^4 & \vdots \end{bmatrix} \tag{6-9}$$

and $\vec{u_o}$ is the disturbance noise vector. The state-space control law representation may be combined with the system equations (Eq.'s (6-3) and (6-4)), resulting in the following representation for the closed loop system:

$$\frac{d}{dt}\begin{bmatrix} \vec{x} \\ \vec{w} \end{bmatrix} = \begin{bmatrix} A & BH \\ GC & F \end{bmatrix}\begin{bmatrix} \vec{x} \\ \vec{w} \end{bmatrix} + \begin{bmatrix} B \\ 0 \end{bmatrix}\vec{u_o} \tag{6-10}$$

$$\vec{y} = \begin{bmatrix} C & 0 \end{bmatrix}\begin{bmatrix} \vec{x} \\ \vec{w} \end{bmatrix} \tag{6-11}$$

The frequency response data presented in the experimental results section are transfer functions between the film sensors and a disturbance force acting on the structure at point 3 in Fig. 6-1. Transfer functions between the PVF_2 sensors (y_6, y_7, y_8) and the input disturbance at point 3 (u_{o3}) were determined using CTRL-C for both the uncontrolled and controlled cases. The results are shown in Fig.'s 6-2 through 6-5. Because of the symmetry of the structure, results for the film sensor on beam 3 (see Fig. 3-7) are identical to the results for film sensor 2. The solid lines represent the uncontrolled responses, while the dashed lines are the actively controlled responses. The results from the simulation agree closely with the measured system response. Simulated results suggest that the control algorithm will be less effective at first mode than at higher modes, which is in accordance with the

actual system behavior. However, the simulation also suggests that the fourth mode attenuation should be greater than what the experimental results indicate.

The method described in this chapter for developing a computer simulation for *smart* structures is applicable to a broad class of systems. These systems include structures in which all *smart* components utilize transducer electrode distributions that may be represented by discrete changes in amplitude and slope. The distributed function of these electrode distributions must be representable as the summation of discrete transducers for the approach to apply. If the distributed actuators and sensors are neither uniform nor linearly varying (e.g. let $\Lambda(Y) = (Y^2 - 2Y + 1)[h(Y) - h(Y-1)]$), then the spatial distribution functions must be discretized. Once the distributed action of the transducers has been modeled as the combined action of point sensors and actuators, then the finite element model may be transformed into state-space and combined with the control law as accomplished in this section.

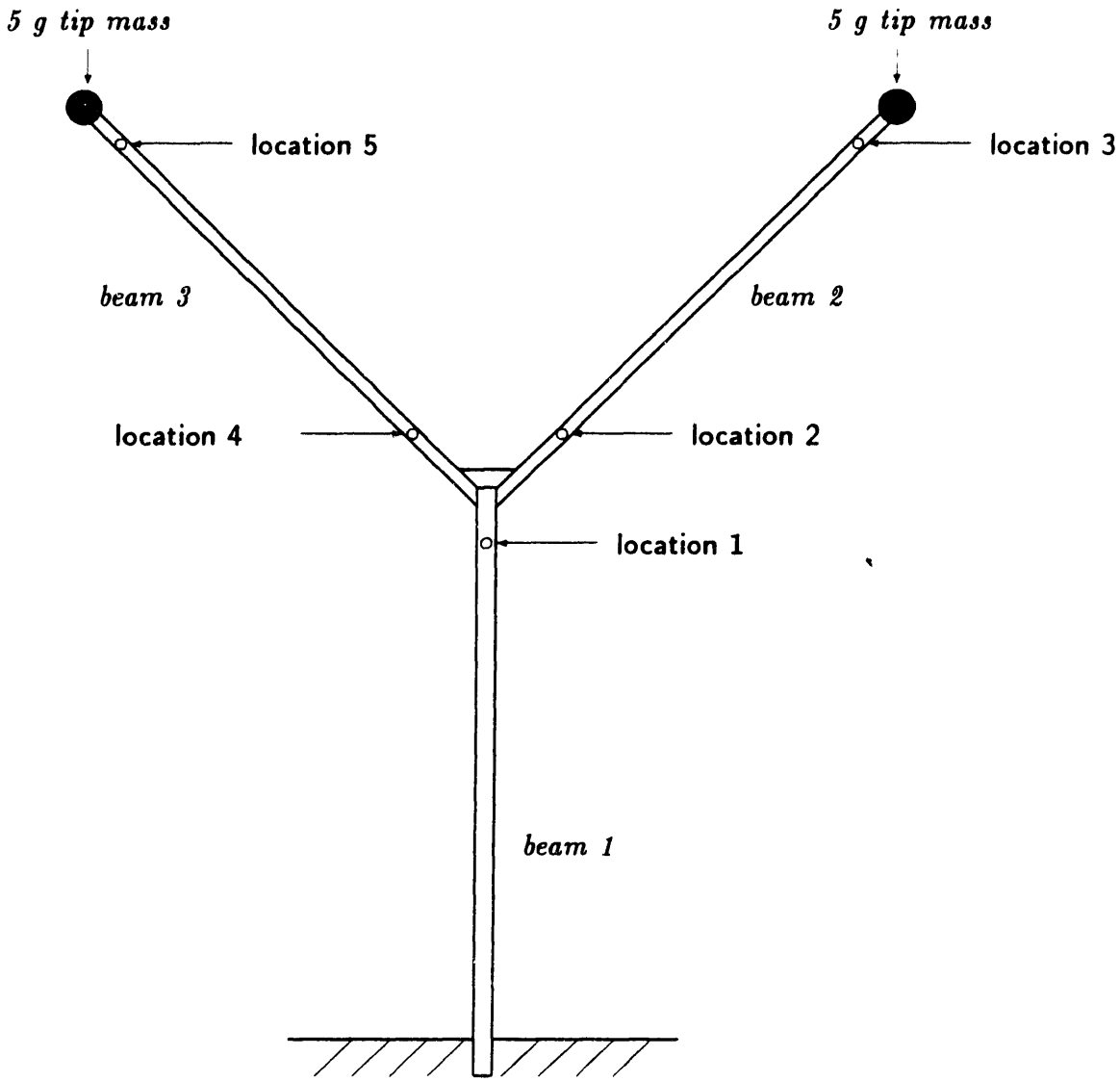

Figure 6-1. Location of discrete sensor and actuator pairs in the digital model.

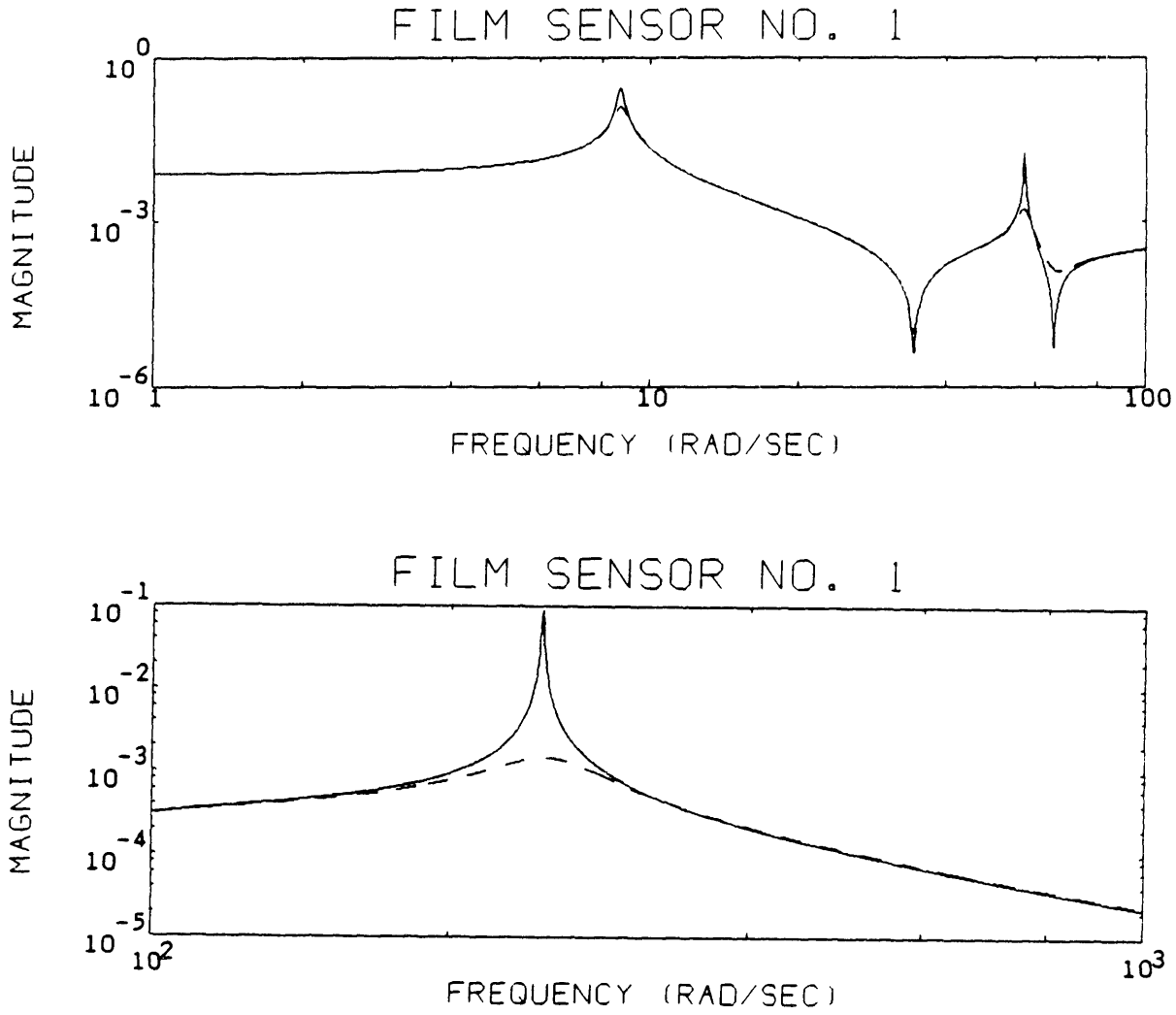

Figure 6-2. Bode plots relating the magnitude of the transfer function between the film sensor on the base beam and the input excitation.

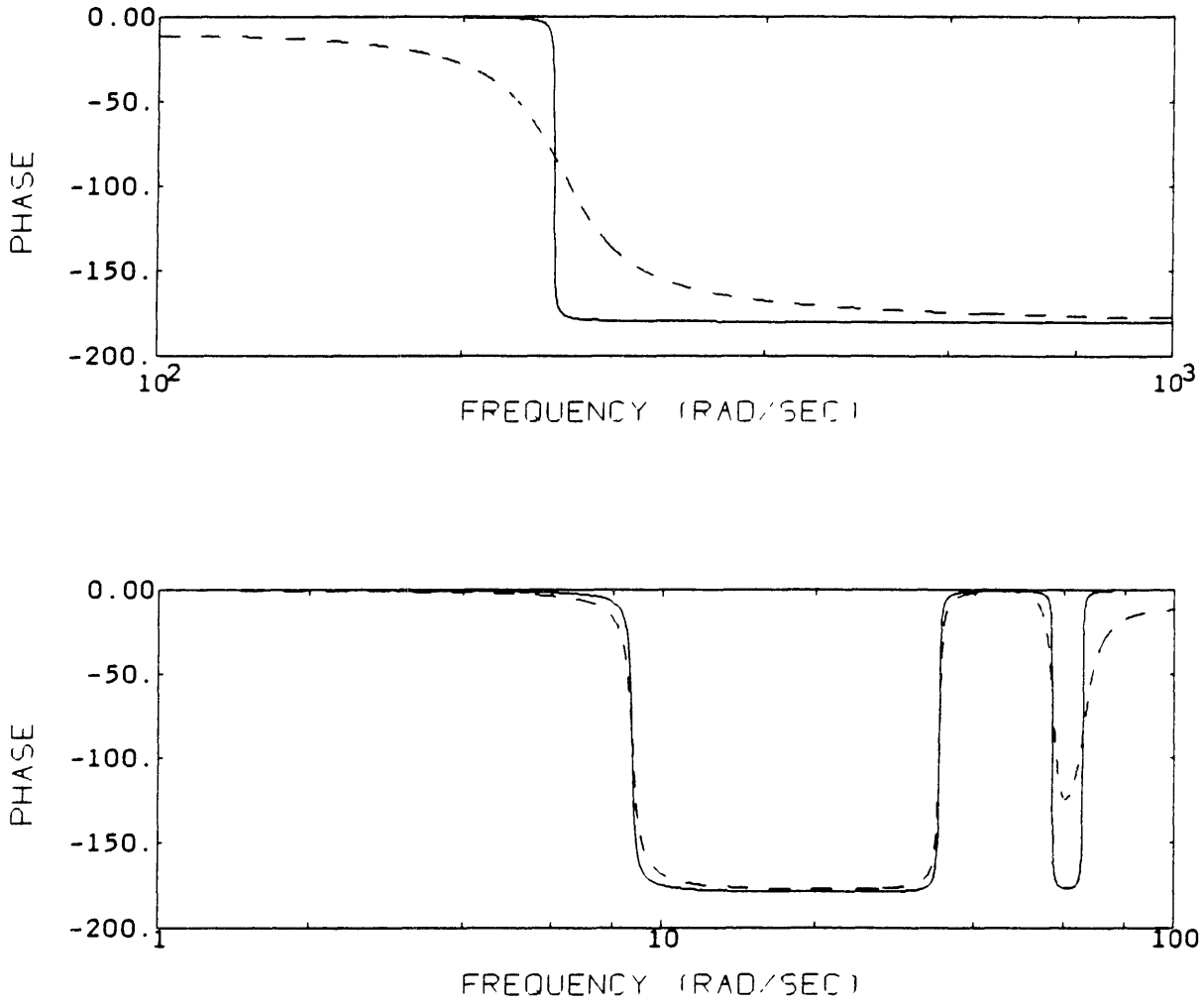

Figure 6-3. Bode plots relating the phase angle of the transfer function between the film sensor on the base beam and input excitation.

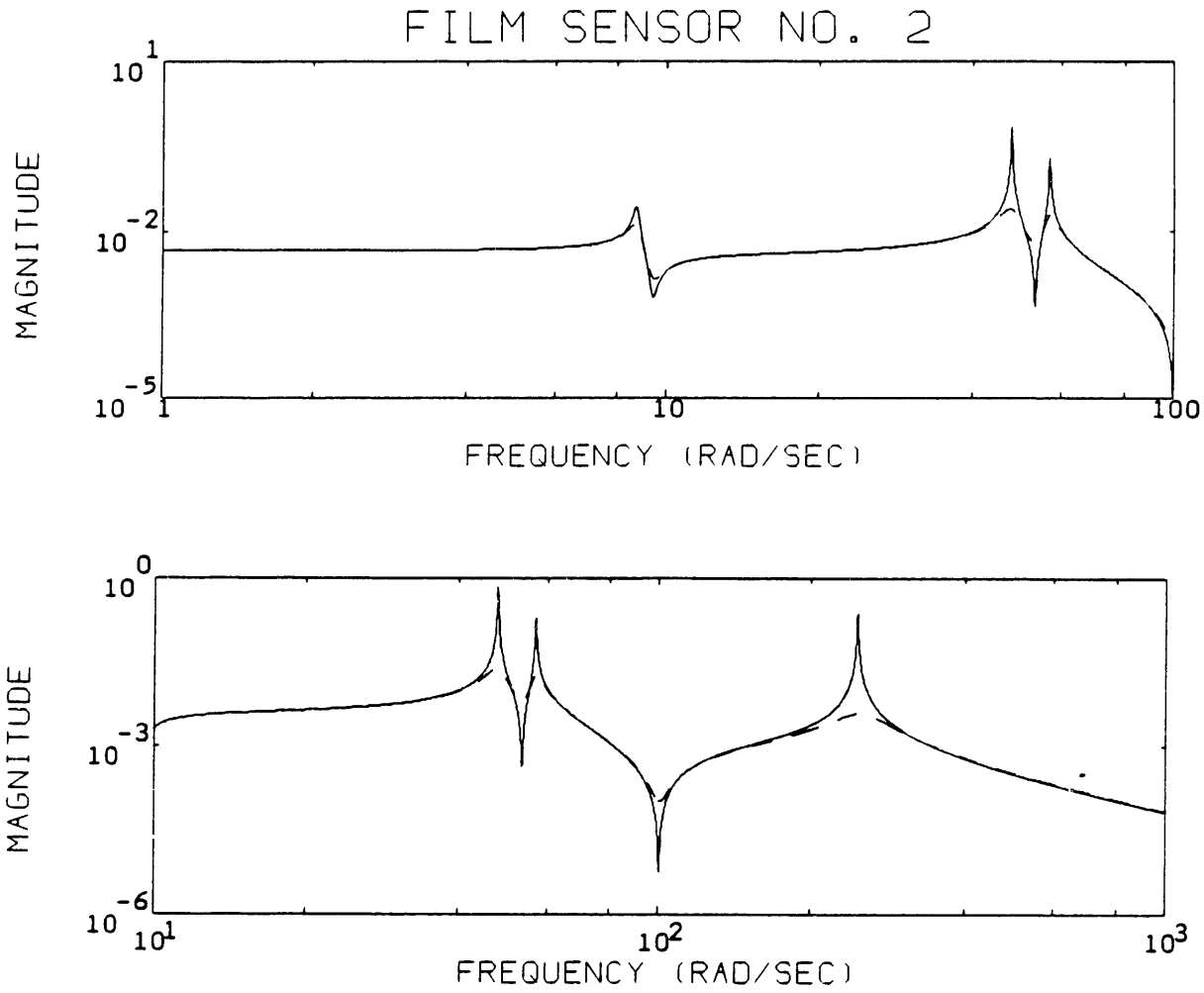

Figure 6-4. Bode plots relating the magnitude of the transfer function between the film sensor on beam 2 and input excitation.

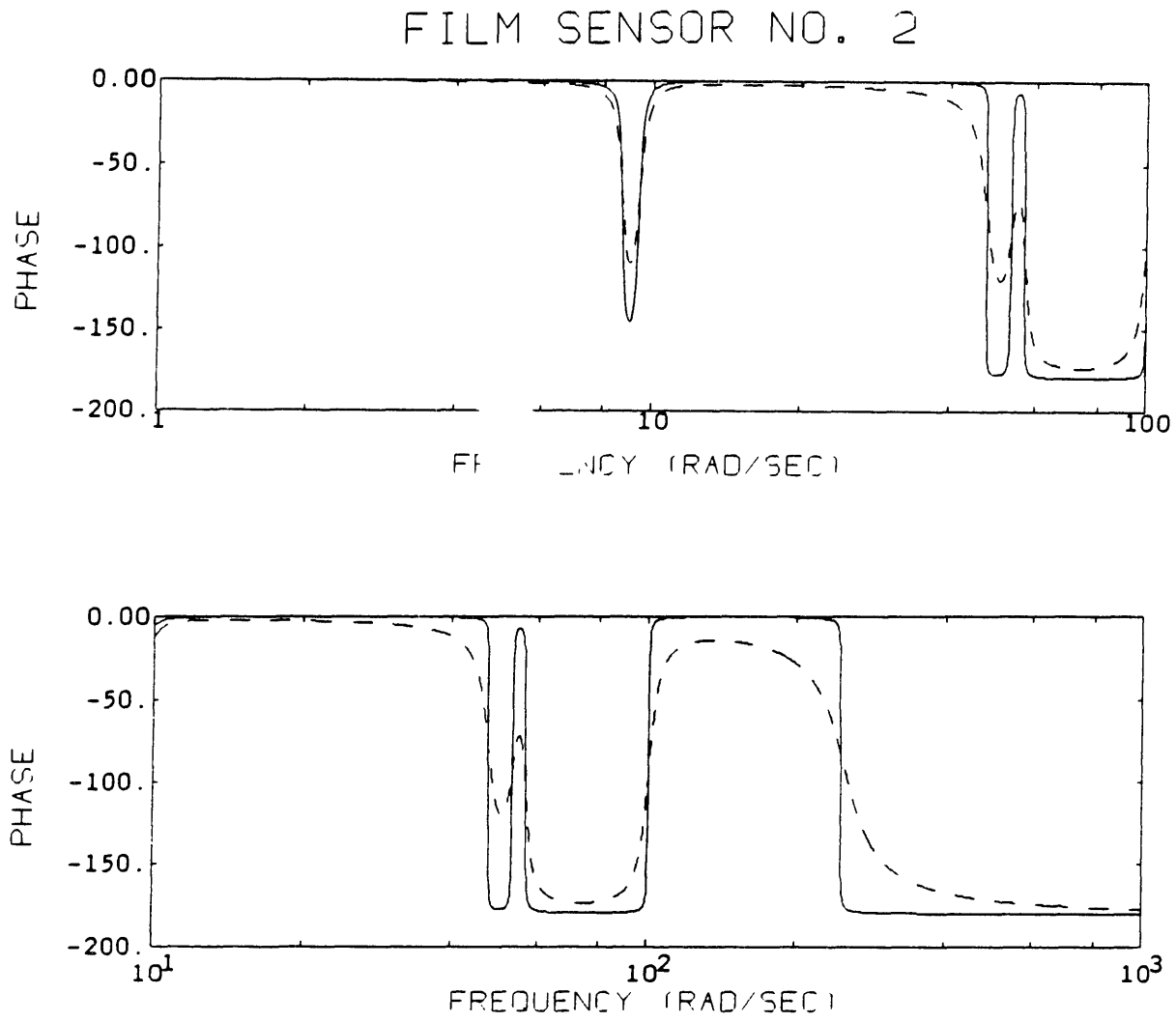

Figure 6-5. Bode plots relating the phase angle of the transfer function between the film sensor on beam 2 and input excitation.

mode	Freq. Estimate		error
	NASTRAN	*Experiment*	
1	1.387 Hz	1.380 Hz	0.51%
2	7.594 Hz	7.600 Hz	0.08%
3	9.037 Hz	9.092 Hz	0.58%
4	39.32 Hz	36.91 Hz	9.79%
5	71.13 Hz	-	-
6	71.15 Hz	-	-
7	137.8 Hz	-	-
8	192.9 Hz	-	-
9	220.7 Hz	-	-
10	295.9 Hz	-	-

Table 6-1. Modal Frequency Estimates

Chapter 7

Conclusions and Recommendations

To facilitate the development of a distributed parameter vibration control strategy for flexible structures, a theoretical model for spatially distributed sensors on a flexible beam was derived without the necessity of modelling the beam in terms of its component vibrational modes. The model predicts that uniform amplitude discontinuities in the spatial distribution result in the sensing of angular displacements, and that uniform slope discontinuities result in the sensing of linear displacements. Both uniform and linearly-varying sensor distributions were studied in order to gain insight into a design methodology for applying film sensors to arbitrary beam configurations. These distributions provide an understanding of film sensors which appeals to one's intuition rather than to mathematical obfuscation. The model shows that the spatial deposition of PVF_2 film on the beam surface may be shaped so as to function similar to point sensors or to produce a signal in which certain vibrational modes of the structure are weighted more than others.

A vibration control strategy for large multi-component structures has been presented in which the structural components are actively damped beam members. Each component element is *smart* in the sense that each obeys a component control law that is autonomous of all other structural members. Distributed sensor and actuator layers are embedded into each structural component. The control law for each smart component is based on the second method of Lyapunov, and does not necessitate truncating the distributed-parameter model into a finite number of modes. A control methodology was derived for a generalized system consisting of an arbitrary number of flexible Bernoulli-Euler beams rigidly fixed to a base beam at a common junction. The theoretical analysis shows that regardless of the energetic

coupling between the component members, energy is guaranteed to be actively removed from the the global system if the *smart* component control law is enforced for each structural element. It is assumed that all eigenvalues of the undamped system are nonpositive. Certain constraints must be met regarding the polarity and spatial orientation of the PVF_2 active elements in order to insure closed-loop stability. The PVF_2 distributions may be spatially varied in order to weight the control authority in favor of certain vibrational modes, or to actively damp vibrations in all modes simultaneously. A *universal* distribution is presented which has the potential of providing active damping to all modes of many multi-component structures if incorporated into every *smart* component of that structure.

The sensor model was verified through experimentation for spatially uniform and linearly-varying PVF_2 film distributions on a cantilever beam. Testing was restricted to frequencies spanning the first three modes of the test structure due to limitations in the point actuator involved in the analysis. In further experimentation, PVF_2 sensors and actuators were incorporated into the same structural component. Radiative noise problems developed when large voltages were applied to the actuator film, which were effectively eliminated with decoupling circuitry. Finally, PVF_2 sensors and actuators were applied to a cantilever beam as the active components of a vibration isolation system, and controllability for the *smart* structure was demonstrated for the first two structural modes.

The *smart* structures control concept was validated both experimentally and through digital simulations. A three component *smart* structure was constructed in the laboratory. A uniform, co-located PVF_2 sensor and actuator pair was incorporated into each component. The component control law derived in the theoretical analysis was enforced for each structural element. Transient and frequency response data were obtained for the first four vibrational modes. The experimental results for these modes show that the control strategy is highly effective in controlling several modes simultaneously. A computational method for the digital modeling of *smart* structures is presented. The method uses the MSC-NAS ı RAN finite element program in conjunction with CTRL-C, a control system design and analysis tool. A simulation was performed for the experimental structure and the results were compared to the experimental data. The simulations closely agree with the observed

system response characteristics.

In specific applications it may be advantageous to use distributed sensors rather than point sensors. Because distributed sensors function as spatial integrators, it is contended that these sensors are less sensitive to placement errors than their discrete counterparts. Non-uniform sensor distributions may be implemented to sense a single mode in specific cases or to weight certain modes more than others. In the context of continuous systems, active dampers have been traditionally based on the implementation of a finite number of discrete sensors and actuators. Since the component elements in theory possess an infinite number of degrees of freedom, these control schemes truncate the system model to a finite number of modes. Difficulties which often arise in determining the number of modes required to accurately model the structure and in reconciling the location of the discrete sensors and actuators are avoided through the implementation of distributed elements.

Results from both the smart structure experiment (i.e. the "Y-structure" experiment) and the digital simulation indicate that the greatest degree of control authority is obtained for structural modes which are characterized by high strain energies. Often the lowest order modes are less controllable than higher order modes using the *smart* structure control strategy: an investigation into the use of this control strategy in conjunction with higher authority actuators may be warranted. Furthermore the control law under study in this paper is a linear control law, and potentially may be optimized in a manner such as that presented in Ref. [6] to improve controller effectiveness.

Appendix A

NASTRAN Simulation Data

```
        N A S T R A N   E X E C U T I V E   C O N T R O L   D E C K   E C H O


    ID RPLEXP,FEM
    SOL 3
    TIME 5
    CHKPNT YES
    CEND
ECHO OF FIRST CARD IN CHECKPOINT DICTIONARY TO BE PUNCHED OUT FOR THIS PROBLEM
   RESTART   RPLEXP  ,FEM     , 2/22/88,   46059,



SMART STRUCTURES
  FINITE ELEMENT MODEL

 MODIFIED MEMBER LENGTHS
                                C A S E   C O N T R O L   D E C K   E C H O
          CARD
          COUNT
           1      TITLE = SMART STRUCTURES
           2      SUBTITLE =  FINITE ELEMENT MODEL
           3      LABEL= MODIFIED MEMBER LENGTHS
           4      SPC = 100
           5      DISP = ALL
           6      METHOD = 100
           7      BEGIN BULK

                       INPUT BULK DATA CARD COUNT =      44
```

SMART STRUCTURES FEBRUARY 22, 1988 MSC/NASTRAN
FINITE ELEMENT MODEL

MODIFIED MEMBER LENGTHS

S O R T E D B U L K D A T A E C H O

CARD COUNT	. 1 ..	2 ..	3 ..	4 ..	5 ..	6 ..	7 ..	8 ..	9 ..	10 .
1-	BAROR				0.	0.	1.			
2-	CBAR	1	100	1	2					
3-	CBAR	2	100	2	3					
4-	CBAR	3	100	3	4					
5-	CBAR	4	100	4	5					
6-	CBAR	5	100	5	6					
7-	CBAR	6	100	6	7					
8-	CBAR	7	100	7	8					
9-	CBAR	8	100	8	9					
10-	CBAR	9	100	9	10					
11-	CBAR	10	100	10	11					
12-	CBAR	12	100	12	13					
13-	CBAR	13	100	13	14					
14-	CBAR	14	100	14	15					
15-	CBAR	15	100	15	16					
16-	CBAR	16	100	16	17					
17-	CBAR	17	100	17	18					
18-	CBAR	18	100	18	19					
19-	CBAR	19	100	19	20					
20-	CBAR	20	100	20	21					
21-	CBAR	21	100	21	22					
22-	CBAR	32	100	32	33					
23-	CBAR	33	100	33	34					
24-	CBAR	34	100	34	35					
25-	CBAR	35	100	35	36					
26-	CBAR	36	100	36	37					
27-	CBAR	37	100	37	38					
28-	CBAR	38	100	38	39					
29-	CBAR	39	100	39	40					
30-	CBAR	40	100	40	41					
31-	CBAR	41	100	41	42					
32-	CBAR	51	100	10	11					
33-	CBAR	52	100	10	11					
34-	CONM2	101	11		.000					
35-	CONM2	201	22		.004					
36-	CONM2	301	42		.004					
37-	CORD2R	1	0	0.0	0.19	0.0	0.0	0.19	1.0	+000001
38-	++000001	1.0	1.19	0.						+000002
39-	CORD2R	2	0	0.0	0.19	0.0	0.0	0.19	1.0	+000003
40-	++000003	-1.0	1.19	0.						+000004
41-	EIGR	100	MGIV				10			+EIG
42-	+EIG	MASS								
43-	GRID	1		0.0	0.0	0.0		345		
44-	GRID	2		0.0	.019	0.0		345		
45-	GRID	3		0.0	.038	0.0		345		
46-	GRID	4		0.0	.057	0.0		345		
47-	GRID	5		0.0	.076	0.0		345		
48-	GRID	6		0.0	.095	0.0		345		
49-	GRID	7		0.0	.114	0.0		345		
50-	GRID	8		0.0	.133	0.0		345		

SMART STRUCTURES FEBRUARY 22, 1988 MSC/NASTRAN
FINITE ELEMENT MODEL

MODIFIED MEMBER LENGTHS

S O R T E D B U L K D A T A E C H O

CARD COUNT	. 1 ..	2 ..	3 ..	4 ..	5 ..	6 ..	7 ..	8 ..	9 ..	10 .
51-	GRID	9		0.0	.152	0.0		345		
52-	GRID	10		0.0	.171	0.0		345		
53-	GRID	11		0.0	.19	0.0		345		
54-	GRID	12	1	0.014	0.0	0.0		345		
55-	GRID	13	1	.0285	0.0	0.0		345		
56-	GRID	14	1	.043	0.0	0.0		345		
57-	GRID	15	1	.0575	0.0	0.0		345		
58-	GRID	16	1	.072	0.0	0.0		345		
59-	GRID	17	1	.0865	0.0	0.0		345		
60-	GRID	18	1	.101	0.0	0.0		345		
61-	GRID	19	1	.1155	0.0	0.0		345		
62-	GRID	20	1	.13	0.0	0.0		345		
63-	GRID	21	1	.1445	0.0	0.0		345		
64-	GRID	22	1	.159	0.0	0.0		345		
65-	GRID	32	2	0.014	0.0	0.0		345		
66-	GRID	33	2	.0285	0.0	0.0		345		
67-	GRID	34	2	.043	0.0	0.0		345		
68-	GRID	35	2	.0575	0.0	0.0		345		
69-	GRID	36	2	.072	0.0	0.0		345		
70-	GRID	37	2	.0865	0.0	0.0		345		
71-	GRID	38	2	.101	0.0	0.0		345		
72-	GRID	39	2	.1155	0.0	0.0		345		
73-	GRID	40	2	.13	0.0	0.0		345		
74-	GRID	41	2	.1445	0.0	0.0		345		
75-	GRID	42	2	.159	0.0	0.0		345		
76-	MAT1	100	210.0E9		.33	7800.0				
77-	PARAM	GRDPNT	0							
78-	PBAR	*100		100		4.8387E-6		6.50362E-11		+000005
79-	*+0000055.85325E-14									+000006
80-	RBAR	11	11	12	123456			126		
81-	RBAR	31	11	32	123456			126		
82-	SPC1	100	126	1						
	ENDDATA									

TOTAL COUNT= 83

SMART STRUCTURES
FINITE ELEMENT MODEL

FEBRUARY 22, 1989 MSC/NASTRAN 12/ 7/84 PAGE 9

MODIFIED MEMBER LENGTHS

REAL EIGENVALUES

MODE NO.	EXTRACTION ORDER	EIGENVALUE	RADIANS	CYCLES	GENERALIZED MASS	GENERALIZED STIFFNESS
1	3	7.600008E+01	8.717802E+00	1.387481E+00	1.000000E+00	7.600008E+01
2	5	2.276832E+03	4.771616E+01	7.594262E+00	1.000000E+00	2.276832E+03
3	2	3.224250E+03	5.678249E+01	9.037213E+00	9.999999E-01	3.224250E+03
4	1	6.105747E+04	2.470981E+02	3.932687E+01	1.000000E+00	6.105747E+04
5	4	1.997656E+05	4.469514E+02	7.113452E+01	9.999999E-01	1.997655E+05
6	7	1.999027E+05	4.471047E+02	7.115892E+01	1.000000E+00	1.999027E+05
7	6	7.491211E+05	8.655178E+02	1.377514E+02	1.000000E+00	7.491211E+05
8	8	1.469500E+06	1.212229E+03	1.929323E+02	9.999999E-01	1.469499E+06
9	10	1.922258E+06	1.386455E+03	2.206612E+02	9.999999E-01	1.922257E+06
10	9	3.457016E+06	1.859305E+03	2.959175E+02	9.999999E-01	3.457015E+06
11	11	5.635135E+06	2.373844E+03	3.778008E+02	0.0	0.0
12	13	8.148278E+06	2.854519E+03	4.543108E+02	0.0	0.0
13	12	1.012527E+07	3.182023E+03	5.064346E+02	0.0	0.0
14	14	1.564692E+07	3.955619E+03	6.295564E+02	0.0	0.0
15	15	2.271782E+07	4.766320E+03	7.585833E+02	0.0	0.0
16	17	2.346395E+07	4.843961E+03	7.709402E+02	0.0	0.0
17	16	3.515312E+07	5.929008E+03	9.436309E+02	0.0	0.0
18	18	4.387005E+07	6.623445E+03	1.054154E+03	0.0	0.0
19	22	5.360584E+07	7.321602E+03	1.165269E+03	0.0	0.0
20	19	6.336672E+07	7.960320E+03	1.266924E+03	0.0	0.0
21	20	8.010682E+07	8.950242E+03	1.424475E+03	0.0	0.0
22	21	9.329670E+07	9.659023E+03	1.537281E+03	0.0	0.0
23	25	1.039480E+08	1.019549E+04	1.622663E+03	0.0	0.0
24	23	1.126432E+08	1.061335E+04	1.689167E+03	0.0	0.0
25	24	1.431337E+08	1.196385E+04	1.904105E+03	0.0	0.0
26	28	1.755108E+08	1.324805E+04	2.108492E+03	0.0	0.0
27	26	2.257558E+08	1.502517E+04	2.391330E+03	0.0	0.0
28	30	2.578685E+08	1.605829E+04	2.555755E+03	0.0	0.0
29	27	3.118390E+08	1.765896E+04	2.810511E+03	0.0	0.0
30	31	3.247119E+08	1.801977E+04	2.867935E+03	0.0	0.0
31	32	3.402314E+08	1.844536E+04	2.935671E+03	0.0	0.0
32	29	4.892713E+08	2.211948E+04	3.520424E+03	0.0	0.0
33	34	3.021573E+09	5.496884E+04	8.748559E+03	0.0	0.0
34	33	4.414308E+09	6.644025E+04	1.057429E+04	0.0	0.0
35	35	1.076584E+10	1.037586E+05	1.651369E+04	0.0	0.0
36	37	1.982500E+10	1.408013E+05	2.240922E+04	0.0	0.0
37	36	2.339081E+10	1.529406E+05	2.434125E+04	0.0	0.0
38	39	3.717874E+10	1.928179E+05	3.068792E+04	0.0	0.0
39	40	5.542448E+10	2.354241E+05	3.746890E+04	0.0	0.0
40	38	6.139612E+10	2.477824E+05	3.943579E+04	0.0	0.0
41	42	7.653032E+10	2.766411E+05	4.402880E+04	0.0	0.0
42	43	1.084929E+11	3.293826E+05	5.242286E+04	0.0	0.0
43	41	1.174350E+11	3.426879E+05	5.454048E+04	0.0	0.0
44	45	1.250573E+11	3.536344E+05	5.628267E+04	0.0	0.0
45	46	1.678419E+11	4.096851E+05	6.520341E+04	0.0	0.0
46	47	1.826681E+11	4.273969E+05	6.802231E+04	0.0	0.0
47	44	1.871036E+11	4.325548E+05	6.884319E+04	0.0	0.0
48	51	2.181684E+11	4.670851E+05	7.433887E+04	0.0	0.0
49	54	2.429880E+11	4.929381E+05	7.845350E+04	0.0	0.0
50	48	2.639959E+11	5.138053E+05	8.177462E+04	0.0	0.0

SMART STRUCTURES FEBRUARY 22, 1988 MSC/NASTRAN 12/ 7/84
FINITE ELEMENT MODEL

MODIFIED MEMBER LENGTHS
EIGENVALUE = 7.600008E+01
CYCLES = 1.387481E+00 REAL EIGENVECTOR NO. 1

POINT ID.	TYPE	T1	T2	T3	R1	R2	R3
1	G	0.0	0.0	0.0	0.0	0.0	0.0
2	G	-4.469667E-02	1.688533E-15	0.0	0.0	0.0	4.654839E+00
3	G	-1.749812E-01	3.377114E-15	0.0	0.0	0.0	9.009267E+00
4	G	-3.851473E-01	5.065789E-15	0.0	0.0	0.0	1.306346E+01
5	G	-6.694937E-01	6.754603E-15	0.0	0.0	0.0	1.681786E+01
6	G	-1.022332E+00	8.443611E-15	0.0	0.0	0.0	2.027332E+01
7	G	-1.437995E+00	1.013286E-14	0.0	0.0	0.0	2.343118E+01
8	G	-1.910845E+00	1.182239E-14	0.0	0.0	0.0	2.629344E+01
9	G	-2.435290E+00	1.351228E-14	0.0	0.0	0.0	2.886276E+01
10	G	-3.005796E+00	1.520252E-14	0.0	0.0	0.0	3.114261E+01
11	G	-3.603979E+00	1.576619E-14	0.0	0.0	0.0	3.180833E+01
12	G	-3.918863E+00	3.148864E-01	0.0	0.0	0.0	3.180833E+01
13	G	-4.248104E+00	6.441264E-01	0.0	0.0	0.0	3.240141E+01
14	G	-4.583028E+00	9.790493E-01	0.0	0.0	0.0	3.291728E+01
15	G	-4.922854E+00	1.318876E+00	0.0	0.0	0.0	3.335860E+01
16	G	-5.266835E+00	1.662858E+00	0.0	0.0	0.0	3.372829E+01
17	G	-5.614256E+00	2.010279E+00	0.0	0.0	0.0	3.402969E+01
18	G	-5.964431E+00	2.360453E+00	0.0	0.0	0.0	3.426648E+01
19	G	-6.316720E+00	2.712743E+00	0.0	0.0	0.0	3.444263E+01
20	G	-6.670524E+00	3.066546E+00	0.0	0.0	0.0	3.456255E+01
21	G	-7.025287E+00	3.421309E+00	0.0	0.0	0.0	3.463091E+01
22	G	-7.380509E+00	3.776532E+00	0.0	0.0	0.0	3.465282E+01
32	G	-3.918863E+00	-3.148864E-01	0.0	0.0	0.0	3.180833E+01
33	G	-4.248104E+00	-6.441264E-01	0.0	0.0	0.0	3.240141E+01
34	G	-4.583028E+00	-9.790493E-01	0.0	0.0	0.0	3.291728E+01
35	G	-4.922854E+00	-1.318876E+00	0.0	0.0	0.0	3.335860E+01
36	G	-5.266835E+00	-1.662858E+00	0.0	0.0	0.0	3.372829E+01
37	G	-5.614256E+00	-2.010279E+00	0.0	0.0	0.0	3.402969E+01
38	G	-5.964431E+00	-2.360453E+00	0.0	0.0	0.0	3.426648E+01
39	G	-6.316720E+00	-2.712743E+00	0.0	0.0	0.0	3.444263E+01
40	G	-6.670524E+00	-3.066546E+00	0.0	0.0	0.0	3.456255E+01
41	G	-7.025287E+00	-3.421309E+00	0.0	0.0	0.0	3.463091E+01
42	G	-7.380509E+00	-3.776532E+00	0.0	0.0	0.0	3.465282E+01

SMART STRUCTURES FEBRUARY 22, 1988 MSC/NASTRAN 12/ 7/84
FINITE ELEMENT MODEL

MODIFIED MEMBER LENGTHS
EIGENVALUE = 2.276832E+03
CYCLES = 7.594262E+00 REAL EIGENVECTOR NO. 2

POINT ID.	TYPE	T1	T2	T3	R1	R2	R3
1	G	0.0	0.0	0.0	0.0	0.0	0.0
2	G	9.538654E-12	3.548510E-06	0.0	0.0	0.0	-9.451067E-10
3	G	3.367492E-11	7.097021E-06	0.0	0.0	0.0	-1.536668E-09
4	G	6.569956E-11	1.064553E-05	0.0	0.0	0.0	-1.775732E-09
5	G	9.893579E-11	1.419404E-05	0.0	0.0	0.0	-1.664754E-09
6	G	1.267679E-10	1.774254E-05	0.0	0.0	0.0	-1.207629E-09
7	G	1.426668E-10	2.129105E-05	0.0	0.0	0.0	-4.096263E-10
8	G	1.402159E-10	2.483955E-05	0.0	0.0	0.0	7.227769E-10
9	G	1.131273E-10	2.838807E-05	0.0	0.0	0.0	2.182655E-09
10	G	5.523990E-11	3.193656E-05	0.0	0.0	0.0	3.963862E-09
11	G	-2.655000E-11	3.311940E-05	0.0	0.0	0.0	4.663004E-09
12	G	-7.271116E-11	3.311945E-05	0.0	0.0	0.0	4.663004E-09
13	G	-1.030678E-01	1.031008E-01	0.0	0.0	0.0	1.972221E+01
14	G	-3.965873E-01	3.966196E-01	0.0	0.0	0.0	3.715067E+01
15	G	-8.570682E-01	8.571022E-01	0.0	0.0	0.0	5.229283E+01
16	G	-1.461156E+00	1.461191E+00	0.0	0.0	0.0	6.516766E+01
17	G	-2.185773E+00	2.185807E+00	0.0	0.0	0.0	7.581015E+01
18	G	-3.008283E+00	3.008317E+00	0.0	0.0	0.0	8.427515E+01
19	G	-3.906752E+00	3.906786E+00	0.0	0.0	0.0	9.064102E+01
20	G	-4.860163E+00	4.860197E+00	0.0	0.0	0.0	9.501195E+01
21	G	-5.848708E+00	5.848742E+00	0.0	0.0	0.0	9.752002E+01
22	G	-6.854102E+00	6.854136E+00	0.0	0.0	0.0	9.832668E+01
32	G	-7.271116E-11	3.311936E-05	0.0	0.0	0.0	4.663004E-09
33	G	1.030678E-01	1.031008E-01	0.0	0.0	0.0	-1.972221E+01
34	G	3.965873E-01	3.966196E-01	0.0	0.0	0.0	-3.715067E+01
35	G	8.570682E-01	8.571022E-01	0.0	0.0	0.0	-5.229283E+01
36	G	1.461156E+00	1.461191E+00	0.0	0.0	0.0	-6.516766E+01
37	G	2.185773E+00	2.185807E+00	0.0	0.0	0.0	-7.581015E+01
38	G	3.008283E+00	3.008317E+00	0.0	0.0	0.0	-8.427515E+01
39	G	3.906752E+00	3.906786E+00	0.0	0.0	0.0	-9.064102E+01
40	G	4.860163E+00	4.860197E+00	0.0	0.0	0.0	-9.501195E+01
41	G	5.848708E+00	5.848742E+00	0.0	0.0	0.0	-9.752002E+01
42	G	6.854102E+00	6.854136E+00	0.0	0.0	0.0	-9.832668E+01

SMART STRUCTURES FEBRUARY 22, 1988 MSC/NASTRAN 12/ 7/84
FINITE ELEMENT MODEL

MODIFIED MEMBER LENGTHS
EIGENVALUE = 3.224250E+03
CYCLES = 9.037213E+00 R E A L E I G E N V E C T O R N O . 3

POINT ID.	TYPE	T1	T2	T3	R1	R2	R3
1	G	0.0	0.0	0.0	0.0	0.0	0.0
2	G	-2.806323E-01	1.255611E-15	0.0	0.0	0.0	2.825040E+01
3	G	-1.024562E+00	2.511215E-15	0.0	0.0	0.0	4.877132E+01
4	G	-2.085269E+00	3.766817E-15	0.0	0.0	0.0	6.160706E+01
5	G	-3.317624E+00	5.022428E-15	0.0	0.0	0.0	6.686317E+01
6	G	-4.579226E+00	6.278042E-15	0.0	0.0	0.0	6.472316E+01
7	G	-5.731959E+00	7.533653E-15	0.0	0.0	0.0	5.545511E+01
8	G	-6.643593E+00	8.789298E-15	0.0	0.0	0.0	3.940909E+01
9	G	-7.189239E+00	1.004496E-14	0.0	0.0	0.0	1.700529E+01
10	G	-7.252503E+00	1.130064E-14	0.0	0.0	0.0	-1.128661E+01
11	G	-6.934610E+00	1.171916E-14	0.0	0.0	0.0	-2.243446E+01
12	G	-6.712523E+00	-2.220899E-01	0.0	0.0	0.0	-2.243446E+01
13	G	-6.418859E+00	-5.157552E-01	0.0	0.0	0.0	-3.468155E+01
14	G	-6.004984E+00	-9.296326E-01	0.0	0.0	0.0	-4.586253E+01
15	G	-5.482445E+00	-1.452175E+00	0.0	0.0	0.0	-5.586028E+01
16	G	-4.863890E+00	-2.070734E+00	0.0	0.0	0.0	-6.457762E+01
17	G	-4.162837E+00	-2.771789E+00	0.0	0.0	0.0	-7.194180E+01
18	G	-3.393425E+00	-3.541203E+00	0.0	0.0	0.0	-7.790810E+01
19	G	-2.570072E+00	-4.364557E+00	0.0	0.0	0.0	-8.246330E+01
20	G	-1.707174E+00	-5.227457E+00	0.0	0.0	0.0	-8.562811E+01
21	G	-8.187346E-01	-6.115898E+00	0.0	0.0	0.0	-8.745923E+01
22	G	8.203381E-02	-7.016668E+00	0.0	0.0	0.0	-8.805077E+01
32	G	-6.712523E+00	2.220899E-01	0.0	0.0	0.0	-2.243446E+01
33	G	-6.418859E+00	5.157552E-01	0.0	0.0	0.0	-3.468155E+01
34	G	-6.004984E+00	9.296326E-01	0.0	0.0	0.0	-4.586253E+01
35	G	-5.482445E+00	1.452175E+00	0.0	0.0	0.0	-5.586028E+01
36	G	-4.863890E+00	2.070734E+00	0.0	0.0	0.0	-6.457762E+01
37	G	-4.162837E+00	2.771789E+00	0.0	0.0	0.0	-7.194180E+01
38	G	-3.393425E+00	3.541203E+00	0.0	0.0	0.0	-7.790810E+01
39	G	-2.570072E+00	4.364557E+00	0.0	0.0	0.0	-8.246330E+01
40	G	-1.707174E+00	5.227457E+00	0.0	0.0	0.0	-8.562811E+01
41	G	-8.187346E-01	6.115898E+00	0.0	0.0	0.0	-8.745923E+01
42	G	8.203381E-02	7.016668E+00	0.0	0.0	0.0	-8.805077E+01

SMART STRUCTURES FEBRUARY 22, 1988 MSC/NASTRAN 12/ 7/84
FINITE ELEMENT MODEL

MODIFIED MEMBER LENGTHS
EIGENVALUE = 6.105747E+04
CYCLES = 3.932687E+01 REAL EIGENVECTOR NO. 4

POINT ID.	TYPE	T1	T2	T3	R1	R2	R3
1	G	0.0	0.0	0.0	0.0	0.0	0.0
2	G	9.796127E-01	2.255172E-15	0.0	0.0	0.0	-9.530429E+01
3	G	3.328663E+00	4.510335E-15	0.0	0.0	0.0	-1.443613E+02
4	G	6.189985E+00	6.765527E-15	0.0	0.0	0.0	-1.499410E+02
5	G	8.789824E+00	9.020769E-15	0.0	0.0	0.0	-1.181635E+02
6	G	1.050460E+01	1.127607E-14	0.0	0.0	0.0	-5.865996E+01
7	G	1.092187E+01	1.353140E-14	0.0	0.0	0.0	1.616428E+01
8	G	9.880572E+00	1.578682E-14	0.0	0.0	0.0	9.253313E+01
9	G	7.480537E+00	1.804227E-14	0.0	0.0	0.0	1.570717E+02
10	G	4.057470E+00	2.029778E-14	0.0	0.0	0.0	1.986176E+02
11	G	2.365457E-01	2.104961E-14	0.0	0.0	0.0	2.014596E+02
12	G	-1.757791E+00	1.994348E+00	0.0	0.0	0.0	2.014596E+02
13	G	-3.686821E+00	3.923377E+00	0.0	0.0	0.0	1.720186E+02
14	G	-5.232958E+00	5.469512E+00	0.0	0.0	0.0	1.272837E+02
15	G	-6.257291E+00	6.493850E+00	0.0	0.0	0.0	7.095561E+01
16	G	-6.664550E+00	6.901112E+00	0.0	0.0	0.0	7.773496E+00
17	G	-6.411439E+00	6.648003E+00	0.0	0.0	0.0	-5.694511E+01
18	G	-5.509968E+00	5.746532E+00	0.0	0.0	0.0	-1.178194E+02
19	G	-4.025350E+00	4.261915E+00	0.0	0.0	0.0	-1.699366E+02
20	G	-2.068650E+00	2.305217E+00	0.0	0.0	0.0	-2.093470E+02
21	G	2.153648E-01	2.120334E-02	0.0	0.0	0.0	-2.334920E+02
22	G	2.664299E+00	-2.427731E+00	0.0	0.0	0.0	-2.415273E+02
32	G	-1.757791E+00	-1.994348E+00	0.0	0.0	0.0	2.014596E+02
33	G	-3.686821E+00	-3.923377E+00	0.0	0.0	0.0	1.720186E+02
34	G	-5.232958E+00	-5.469512E+00	0.0	0.0	0.0	1.272837E+02
35	G	-6.257291E+00	-6.493850E+00	0.0	0.0	0.0	7.095561E+01
36	G	-6.664550E+00	-6.901112E+00	0.0	0.0	0.0	7.773496E+00
37	G	-6.411439E+00	-6.648003E+00	0.0	0.0	0.0	-5.694511E+01
38	G	-5.509968E+00	-5.746532E+00	0.0	0.0	0.0	-1.178194E+02
39	G	-4.025350E+00	-4.261915E+00	0.0	0.0	0.0	-1.699366E+02
40	G	-2.068650E+00	-2.305217E+00	0.0	0.0	0.0	-2.093470E+02
41	G	2.153648E-01	-2.120334E-02	0.0	0.0	0.0	-2.334920E+02
42	G	2.664299E+00	2.427731E+00	0.0	0.0	0.0	-2.415273E+02

SMART STRUCTURES
FINITE ELEMENT MODEL

FEBRUARY 22, 1988 MSC/NASTRAN 12/ 7/84

MODIFIED MEMBER LENGTHS
EIGENVALUE = 1.997656E+05
CYCLES = 7.113452E+01

REAL EIGENVECTOR NO. 5

POINT ID.	TYPE	T1	T2	T3	R1	R2	R3
1	G	0.0	0.0	0.0	0.0	0.0	0.0
2	G	-2.280203E+00	5.384843E-13	0.0	0.0	0.0	2.145598E+02
3	G	-7.216111E+00	1.076967E-12	0.0	0.0	0.0	2.811465E+02
4	G	-1.215313E+01	1.615446E-12	0.0	0.0	0.0	2.197365E+02
5	G	-1.501350E+01	2.153922E-12	0.0	0.0	0.0	7.107446E+01
6	G	-1.466329E+01	2.692391E-12	0.0	0.0	0.0	-1.076928E+02
7	G	-1.112588E+01	3.230855E-12	0.0	0.0	0.0	-2.541379E+02
8	G	-5.554338E+00	3.769309E-12	0.0	0.0	0.0	-3.140112E+02
9	G	3.602991E-02	4.307753E-12	0.0	0.0	0.0	-2.522249E+02
10	G	3.186172E+00	4.846185E-12	0.0	0.0	0.0	-5.717047E+01
11	G	3.331555E+00	5.025654E-12	0.0	0.0	0.0	4.777716E+01
12	G	2.858588E+00	4.729698E-01	0.0	0.0	0.0	4.777716E+01
13	G	1.925250E+00	1.406394E+00	0.0	0.0	0.0	1.271774E+02
14	G	3.978151E-01	2.933908E+00	0.0	0.0	0.0	1.635488E+02
15	G	-1.285915E+00	4.617722E+00	0.0	0.0	0.0	1.582252E+02
16	G	-2.723250E+00	6.055131E+00	0.0	0.0	0.0	1.167864E+02
17	G	-3.590420E+00	6.922366E+00	0.0	0.0	0.0	4.893887E+01
18	G	-3.680069E+00	7.012076E+00	0.0	0.0	0.0	-3.256285E+01
19	G	-2.923865E+00	6.255929E+00	0.0	0.0	0.0	-1.137005E+02
20	G	-1.394605E+00	4.726720E+00	0.0	0.0	0.0	-1.813355E+02
21	G	7.139394E-01	2.618221E+00	0.0	0.0	0.0	-2.253516E+02
22	G	3.127665E+00	2.045368E-01	0.0	0.0	0.0	-2.404435E+02
32	G	2.858588E+00	-4.729698E-01	0.0	0.0	0.0	4.777716E+01
33	G	1.925250E+00	-1.406394E+00	0.0	0.0	0.0	1.271774E+02
34	G	3.978151E-01	-2.933908E+00	0.0	0.0	0.0	1.635488E+02
35	G	-1.285914E+00	-4.617721E+00	0.0	0.0	0.0	1.582252E+02
36	G	-2.723250E+00	-6.055131E+00	0.0	0.0	0.0	1.167864E+02
37	G	-3.590420E+00	-6.922366E+00	0.0	0.0	0.0	4.893887E+01
38	G	-3.680069E+00	-7.012076E+00	0.0	0.0	0.0	-3.256285E+01
39	G	-2.923865E+00	-6.255929E+00	0.0	0.0	0.0	-1.137005E+02
40	G	-1.394605E+00	-4.726720E+00	0.0	0.0	0.0	-1.813355E+02
41	G	7.139394E-01	-2.618221E+00	0.0	0.0	0.0	-2.253516E+02
42	G	3.127665E+00	-2.045368E-01	0.0	0.0	0.0	-2.404435E+02

References

[1] Burke, S. and Hubbard,J.E., *Active Vibration Control of a Simply-Supported Beam Using a Spatially Distributed Actuator*, IEEE Control Systems Magazine, Vol. 7 No. 6, Aug. 1987, pp. 25-30.

[2] Forward, R.L., and Swigert, C.J. *Electronic Damping of Orthogonal Bending Modes in a Cylindrical Mast*, AIAA papers 81-4017/4018, Journal of Spacecraft and Rockets, 1981.

[3] Haftka, R.T., Martinovic, Z.N., Hallauer, W.L., and Schamel, G. *Sensitivity of Optimized Control Systems to Minor Structural Modifications*, Procedings, AIAA/ASME/ASCE/AHS 26th Structures, Structural Dynamics and Materials Conference, 1985.

[4] Komkov, V., Optimal Control Theory for Damping of Vibrations of Elastic Systems. Springer-Verlag, Berlin, 1972.

[5] Meirovitch, L., and Baruh, H., *Nonlinear Control of an Experimental Beam*, AIAA preprint No. 83-0855, 1984.

[6] Bailey, T. and Hubbard, J.E. *Distributed Piezoelectric Polymer Active Vibration Control of a Cantilever Beam*, Journal of Guidance, Control, and Dynamics, Vol. 8, No. 5, 1985, pp. 605-611.

[7] Hubbard, J.E. *Method and Apparatus using a Piezoelectric Film for Active Control of Vibrations*, U.S. Patent Number 4565940, 1986.

[8] Burke, S., and Hubbard, J.E., *Distributed Actuator Control Design for Flexible Beams*, Proceedings, 4th IFAC Conference on Control of Distributed Parameter Systems, 1986, to appear in Automatica, Sept. 1988.

[9] Nakamura, Y., Hanafusa, H., and Ueno, N., *A Piezoelectric Film Sensor with Uniformly Expanded Surface To Detect Tactile Information for Robotic Endeffectors*, presented at ICAR Conference, Tokyo, 1985.

[10] Linvill, J.G. PVF_2-Models, Measurements, Device Ideas, ICL, Stanford University, Technical Report No. 4834-3, 1978.

[11] Hayakawa and Wada, *Piezoelectricity and Related Properties of Polymer Films*, Advances in Polymer Science,Vol.11, No. 1., 1973.

[12] Tamura, Ogasawara, Ono, and Hagiwara, *Piezoelectricity in Uniaxially Stretched Polyvinylidene Fluoride*, Journal of Applied Physics, Vol. 45, 1974, pp.3768-3771.

[13] Tamura, Yamaguchi, Oyata, and Yoshimi, *Electroacoustic Transducers with piezoelectric High Polymer Films*, Journal of Audio Eng. Soc., Vol. 23, 1975, pp.21-26.

[14] Chatigny, J.V. and Robb, L., *Piezo Film Sensors*, Sensors, Vol. 3, No. 5, May 1986.

[15] de Lafontaine, J., *Sensor/Actuator Selection and Placement for Control of Elastic Continua*, presented at the 4th IFAC Conference on Control of Distributed Parameter Systems, 1986.

[16] Kynar Piezo Film Technical Manual, Pennwalt Corporation, 1985.

[17] Lighthill, M., An Introduction to Fourier Analysis and Generalized Functions, Cambridge Univ. Press, Cambridge, England, 1958.

[18] Crandall, S.H., Engineering Analysis, McGraw-Hill, New York., 1956, pp. 286-289.

[19] Nicolet Scientific Corp., *Instruction Manual for the Model 660B Dual Channel FFT Analyzer*, Rev. 2, 1981, p.550.

[20] Properties of Solef Piezoelectric Sheets, Solvay Technologies, Inc., May 1985.

[21] Bailey,T., *Distributed Parameter Active Vibration Control of a Cantilever Beam*, MS/BS Thesis, Dept. of Mech. Engineering, MIT, Sept. 1984.

[22] Plump, J., Hubbard, J.E., Bailey, T., *Nonlinear Control of a Distributed System: Simulation and Experimental Results*, Transactions of the ASME, Journal of Dynamic Systems, Measurement, and Control; Vol. 109 No. 2, June 1987 pp. 133-139.

[23] Kalmann, R.E. and Bartram, J.E., *Control Systems Analysis and Design Via the Second Method of Lyapunov*, Journal of Basic Engineering, Transactions of the ASME, pp.371-400, 1960.